GLP-1R associates with VAPB and SPHKAP at ERMCSs to regulate β-cell mitochondrial remodelling and function.

Gregory Austin[1,*], Affiong I. Oqua[1,*], Liliane El Eid[1], Mingli Zhu[1], Yusman Manchanda[1], Priyanka Peres[2], Helena Coyle[2], Yelyzaveta Poliakova[3], Karim Bouzakri[4], Alex Montoya[5], Dominic J. Withers[5,6], Michele Solimena[7,8,9], Ben Jones[10], Steven J. Millership[1], Steffen Burgold[11], David C.A. Gaboriau[12], Endre Majorovits[11], Inga Prokopenko[13,14], Jonathon Nixon-Abell[2], Andreas Müller[7,8,9] and Alejandra Tomas[1,#]

[1] Section of Cell Biology and Functional Genomics, Division of Diabetes, Endocrinology, and Metabolism, Department of Metabolism, Digestion and Reproduction, Imperial College London, London, United Kingdom.
[2] Cambridge Institute for Medical Research, Department of Clinical Neurosciences, University of Cambridge, Cambridge, United Kingdom.
[3] School of Public Health, Imperial College London, London, United Kingdom.
[4] Centre Européen d'Étude du Diabète, Strasbourg, France.
[5] MRC Laboratory of Medical Sciences, London, United Kingdom.
[6] Institute of Clinical Sciences, Faculty of Medicine, Imperial College London, London, United Kingdom.
[7] Molecular Diabetology, University Hospital and Faculty of Medicine Carl Gustav Carus, TU Dresden, Dresden, Germany.
[8] Paul Langerhans Institute Dresden, Helmholtz Center Munich, University Hospital Carl Gustav Carus and Faculty of Medicine, TU Dresden, Dresden, Germany.
[9] German Center for Diabetes Research, Neuherberg, Germany.
[10] Section of Endocrinology and Investigative Medicine, Division of Diabetes, Endocrinology, and Metabolism, Department of Metabolism, Digestion and Reproduction, Imperial College London, London, United Kingdom.
[11] Carl Zeiss Microscopy GmbH, ZEISS Gruppe, Oberkochen, Germany.
[12] Facility for Imaging by Light Microscopy, National Heart and Lung Institute, Imperial College London, London, United Kingdom.
[13] Department of Clinical and Experimental Medicine, University of Surrey, Guildford, United Kingdom.
[14] People-Centred Artificial Intelligence Institute, University of Surrey, Guildford, United Kingdom.

*Joint first authors

[#]Corresponding author: a.tomas-catala@imperial.ac.uk

Abstract

Glucagon-like peptide-1 receptor (GLP-1R) agonists (GLP-1RAs) ameliorate mitochondrial health by increasing mitochondrial turnover in metabolically relevant tissues. Mitochondrial adaptation under metabolic stress is crucial to maintain pancreatic β-cell function and prevent type 2 diabetes (T2D) progression. While the GLP-1R is well known to stimulate cAMP production leading to Protein Kinase A (PKA) and Exchange Protein Activated by cyclic AMP 2 (Epac2) activation, there is a lack of understanding of the molecular mechanisms that link GLP-1RA-induced signalling with mitochondrial remodelling and functional adaptation. Here, we present a comprehensive study in β-cells and primary mouse and human islets that demonstrates that, following GLP-1RA stimulation, GLP-1R-positive endosomes associate with the endoplasmic reticulum (ER) membrane contact site (MCS) tether VAPB at ER-mitochondria MCSs (ERMCSs), where active GLP-1R engages with SPHKAP, an A-kinase anchoring protein (AKAP) linked to T2D and adiposity risk in genome-wide association studies (GWAS). The inter-organelle complex formed by endosomal GLP-1R, ER VAPB and SPHKAP triggers a pool of ERMCS-localised cAMP/PKA signalling which leads to the phosphorylation of the mitochondrial contact site and cristae organising system (MICOS) complex component MIC19 and is accompanied by mitochondrial remodelling and modulation of mitochondrial function, with important consequences for β-cell function and survival to oxidative stress.

Introduction

Maintenance of mitochondrial function and mitochondrial adaptation to changes in nutritional state is vital for the preservation of pancreatic β-cell regulated secretion of insulin[1], the main hormone in charge of lowering blood glucose concentrations, with disruptions in this process underlying the development and/or progression of type 2 diabetes (T2D)[2, 3] – an uncontrolled pandemic affecting ~500 million people worldwide, and causing ~1.5 million deaths per year[4]. The incretin glucagon-like peptide-1 (GLP-1), released from the gut during food intake, amplifies glucose-stimulated insulin release by binding to and activating its cognate G protein-coupled receptor (GPCR), the GLP-1 receptor (GLP-1R), triggering cAMP generation and downstream Protein Kinase A (PKA) and Exchange Protein Activated by cyclic AMP 2 (Epac2) signalling[5], a process that has been exploited to develop pharmacological GLP-1R agonists (GLP-1RAs) as T2D therapies. There is extensive data highlighting the beneficial role of GLP-1RAs in the maintenance and/or restoration of mitochondrial function in β-cells and beyond, with reports emphasising their capacity to induce mitochondrial remodelling/turnover and functional adaptation[6, 7, 8, 9], two closely intertwined processes essential for the preservation of optimal metabolic activity[10]. While a range of GLP-1R-induced pathways has been reported, there is no clear description of the molecular mechanisms engaged by the receptor to modulate mitochondrial remodelling and improve mitochondrial function. Here, we present new evidence in β-cells and primary mouse and human islets demonstrating that, following agonist binding and internalisation, endosomal GLP-1R binds to endoplasmic reticulum (ER)-localised ER-mitochondria membrane contact site (ERMCS) organising factor VAPB to locally engage SPHKAP, an A-kinase anchoring protein (AKAP) whose gene coding variants have been linked to T2D and high BMI risk in genome-wide association studies (GWAS). We further show that SPHKAP itself localises to ERMCSs via its direct interaction with VAPB through a pFFAT motif present in SPHKAP. Establishment of a membrane contact site (MCS) between GLP-1R-positive endosomes and ERMCS-localised VAPB leads to the generation of a pool of highly-localised cAMP and PKA activity that triggers the PKA-dependent phosphorylation of the mitochondrial contact site and cristae organising system (MICOS) complex component MIC19, as well as GLP-1RA-induced mitochondrial remodelling, resulting in improved β-cell mitochondrial function and contributing to the potentiation of insulin secretion and survival to ER stress afforded by the GLP-1R. This is, to our knowledge, the first description of a three-way contact between an endosomal GPCR, the ER-resident MCS tether VAPB and mitochondria with engagement of an ERMCS-localised AKAP enabling the assembly of a highly-localised GPCR signalling hub to control the function of the MICOS complex, and therefore cristae architecture and mitochondrial turnover. Our data not only unveils a previously unknown pathway of ERMCS-localised Gαs-coupled GPCR signalling into mitochondria, potentially applicable to other GPCRs beyond the GLP-1R, but also opens the door to further roles of the GLP-1R in the regulation of mitochondrial lipid metabolism, a process tightly linked to changes in mitochondrial morphology and known to be governed by MIC19 activity[11]. In summary, this study has uncovered the molecular mechanism employed by the GLP-1R to achieve mitochondrial regeneration leading to optimised β-cell function, with important repercussions in our current understanding of the beneficial role of GLP-1RAs in disorders such as T2D, obesity, and neurodegeneration.

Results

Human GLP-1R β-cell interactome reveals binding of agonist-stimulated GLP-1R to signalling effectors, with strong prevalence of ERMCSs-localised proteins.

To gain a comprehensive understanding of the specific downstream partners and signalling mediators engaged by active GLP-1Rs in pancreatic β-cells, we performed an interactome

analysis of proteins that bind to the receptor under vehicle *versus* 5-minute stimulation with the GLP-1RA exendin-4 in a subline of rat INS-1 832/3 β-cells stably expressing SNAP/FLAG-tagged human GLP-1R (SNAP/FLAG-hGLP-1R). Mass spectrometry (MS) analysis of GLP-1R co-immunoprecipitants revealed a list of proteins enriched in agonist-stimulated *versus* unstimulated conditions (Fig. 1a,b, Supplementary Fig. 1a). Gene ontology analysis of the identified factors indicated that these were involved in pathways related to endomembranes and the ER (Supplementary Fig. 1b). Amongst these factors, we found a high number of proteins localised to ERMCSs (Fig. 1c), which are points of close interaction, but not fusion, between the ER and mitochondria that fulfil specific functions including cross-organelle ion and lipid sensing and transfer, and signal transmission to coordinate mitochondrial remodelling[12]. While known GLP-1R interactors such as $G\alpha_S$, AP2, Rab5, and β-arrestin 2 were reassuringly identified in our interactomic list, the most prominently enriched factor interacting with active GLP-1R was VAMP Associated Protein B (VAPB), followed by its homolog VAPA, integral ER proteins whose main role is the establishment and maintenance of organelle-ER interactions, or membrane contact sites (MCSs)[13, 14], including those involving endosomes and/or mitochondria. We next validated the active GLP-1R–VAPB binding inferred from our MS results by co-immunoprecipitating both EGFP-VAPB (Fig. 1d) and endogenous VAPB (Fig. 1e, Supplementary Fig. 1c) with SNAP/FLAG-hGLP-1R in vehicle *versus* exendin-4-stimulated INS-1 832/3 SNAP/FLAG-hGLP-1R cells. Confocal microscopy analysis of exendin-4-stimulated GLP-1R co-localisation with EGFP-VAPB in these cells revealed that GLP-1R-positive endosomes are intimately associated with VAPB-positive ER network regions, with the ER often surrounding a central core of GLP-1R-positive signal (Fig. 1f), suggesting that GLP-1R-containing endosomes directly contact VAPB-positive ER membranes, potentially at MCSs. This hypothesis was validated by transmission electron microscopy (TEM) localisation of SNAP/FLAG-hGLP-1R (labelled at the cell surface with SNAP-biotin plus streptavidin-gold particles in living cells prior to exendin-4 stimulation) to endosome-ER MCSs (Fig. 1g). Further microscopy experiments performed to visualise GLP-1R engagement with EGFP-VAPB in response to exendin-4 stimulation include confocal imaging of serial optical sections covering the entire cell thickness after SNAP/FLAG-hGLP-1R cell surface labelling with a membrane impermeable SNAP-tag probe followed by exendin-4 stimulation, represented as a maximum intensity projection (MIP) in Fig. 1h, and time-lapse confocal microscopy analysis of exendin-4-induced SNAP/FLAG-hGLP-1R trafficking from the plasma membrane to endosomes situated in close proximity to EGFP-VAPB-positive ER regions (Supplementary Fig. 1d, Supplementary Movie 1).

The interaction of active GLP-1R with VAPB was deemed functionally relevant, as it was no longer present when VAPB P56S, a self-aggregating loss-of-function VAPB mutant associated with amyotrophic lateral sclerosis (ALS)[15, 16], was expressed instead of its wildtype (WT) counterpart (Supplementary Fig. 1e,f), and as both VAPB knockdown by RNAi (Fig. 1i, Supplementary Fig. 1g,h), and overexpression of VAPB P56S, but not of WT VAPB (Supplementary Fig. 1i), significantly reduced the capacity of GLP-1R to potentiate insulin secretion from INS-1 832/3 cells.

Agonist-stimulated GLP-1R–VAPB binding requires GLP-1R internalisation and is differentially modulated by GLP-1RAs with varying GLP-1R internalisation propensities.

To elucidate whether active GLP-1R requires its prior internalisation for VAPB binding, we co-transfected INS-1 832/3 SNAP/FLAG-hGLP-1R cells with dominant negative (K44A) mutants of dynamin 1 and 2 to block GLP-1R endocytosis triggered by exendin-4 (Supplementary Fig. 2a). Under these conditions, increased binding of the receptor to VAPB in stimulated *versus* vehicle conditions was abrogated (Fig. 2a), demonstrating that active GLP-1R interacts with VAPB following its agonist-induced internalisation. Supporting this

notion, MS interactomic analyses of GLP-1R co-immunoprecipitates in INS-1 832/3 SNAP/FLAG-hGLP-1R cells after 5-minute stimulation with endogenous agonist GLP-1, as well as with exendin-4-based biased GLP-1RAs exendin-F1 and exendin-D3, previously shown to trigger differing degrees of GLP-1R internalisation[17, 18], resulted in marked differences in the propensity of the receptor to associate with VAPB (Supplementary Fig. 3), with agonists that trigger robust receptor internalisation (GLP-1, exendin-4, exendin-D3) showing a stronger degree of GLP-1R-VAPB interaction compared to slow GLP-1R-internalising exendin-F1. Marked kinetic differences in GLP-1R-VAPB interaction following exendin-4 *versus* exendin-F1 stimulation were also demonstrated in INS-1 832/3 cells by a novel NanoBRET assay, with Nanoluciferase-tagged GLP-1R co-expressed with Venus-tagged VAPB (Fig. 2b, Supplementary Fig. 2b). We extended our analysis to a panel of seven GLP-1RAs, including, as well as exendin-4, exendin-F1, and exendin-D3, fatty acid-modified semaglutide[19] and tirzepatide[20], as well as small molecules orforglipron[21] and danuglipron[22]. We first tested these GLP-1RAs for their capacity to induce GLP-1R internalisation in purified mouse islets transduced with SNAP/FLAG-hGLP-1R-expresssing adenoviruses (Fig. 2c). As previously shown, acute (5-minute) exposure to exendin-4 and exendin-D3 triggered noticeable GLP-1R internalisation, while this was much reduced with the biased agonist exendin-F1. Additionally, and as previously published[23], semaglutide triggered a much more robust GLP-1R internalisation than tirzepatide, an agonist that shows a similar degree of GLP-1R $G_{\alpha S}$ bias to exendin-F1. We also detected a clear difference in GLP-1R internalisation triggered by orforglipron *versus* danuglipron, with the latter showing a similar level of receptor internalisation to that of exendin-4, while the former resulted in very reduced receptor internalisation 5 minutes post-agonist exposure. VAPB co-immunoprecipitation using the panel of GLP-1RAs described above unveiled a correlation between the level of GLP-1R–VAPB binding and the degree of receptor internalisation elicited by each of the tested GLP-1RAs (Fig. 2d, Supplementary Fig. 2c).

Exendin-4-stimulated GLP-1R triggers VAPB-localised cAMP generation and PKA activity at the outer mitochondrial membrane.

As stated above, besides VAPB, our interactome analysis highlighted several factors enriched for their association with active GLP-1R localised at the ER, mitochondria and/or ERMCSs (Fig. 1c), a location where VAPB plays a prominent organising role[16], suggesting that ERMCSs could be a potential hub for endosomal GLP-1R signalling. To determine if GLP-1R induces cAMP generation specifically at VAPB locations, we modified a fluorescence resonance energy transfer (FRET)-based system of biosensors targeted to endogenous proteins (FluoSTEPs)[24], so that a FRET cAMP sensor would fully reconstitute only in the presence of GFP_{11} fragment fused to VAPB, resulting in functional biosensor assembly specifically at VAPB loci (Supplementary Fig. 2d). This modified FluoSTEP system was used to measure VAPB-localised cAMP generation in response to either exendin-4 or exendin-F1 stimulation (Fig. 2e). Results in WT INS-1 832/3 cells (expressing endogenous levels of GLP-1R) show VAPB-localised cAMP responses with both agonists, which are less pronounced for the slow internalising exendin-F1 compared to exendin-4, demonstrating that GLP-1R actively signals at VAPB loci. Next, we evaluated whether GLP-1R signalling would also trigger a pool of PKA activity at the surface of mitochondria, a process known to be important for the control of mitochondrial function[25]. To this end, we employed either a global (whole cell) or a mitochondrially-restricted PKA biosensor expressed at the outer mitochondrial membrane (OMM)[26] (Supplementary Fig. 2e). Exendin-4 stimulation of WT INS-1 832/3 cells triggered, as expected, a robust global PKA response, which was also evident with the OMM-localised PKA biosensor, demonstrating that GLP-1R stimulation triggers mitochondrial PKA activity (Supplementary Fig. 2f). Furthermore, utilising the same biosensors as above, we detected reduced OMM-localised but no change in global PKA activity with slow internalising exendin-F1 *versus* exendin-4 (Fig. 2f), leading to an increased mitochondrial over global PKA signalling propensity with exendin-4 at this acute (5-minute) stimulation time-point (Fig. 2g). This, together with the VAPB-localised cAMP FluoSTEP

results from above, indicates that GLP-1R internalisation is important for GLP-1R-induced cAMP generation at VAPB loci and PKA signalling at OMMs, at least acutely.

Exendin-4-stimulated GLP-1R associates with ERMCSs.

To examine the potential docking of GLP-1R-positive endosomes to ERMCSs, we first performed a crude mitochondrial purification, a method that results in isolation of mitochondria together with associated ER membranes, from vehicle *versus* exendin-4-stimulated INS-1 832/3 SNAP/FLAG-hGLP-1R cells. Results showed increased SNAP/FLAG-hGLP-1R association with crude mitochondrial fractions in exendin-4-stimulated *versus* vehicle conditions (Fig. 3a). We next employed a split-GFP-based contact site sensor (SPLICS)[27] to specifically visualise ERMCSs in conjunction with SNAP/FLAG-hGLP-1R in exendin-4-stimulated INS-1 832/3 SNAP/FLAG-hGLP-1R cells (Fig. 3b,c, Supplementary Movie 2). This approach allowed us to visualise an intimate association between GLP-1R-positive endosomes and ERMCSs over time, validating our hypothesis.

Further high-resolution 3D imaging modalities were then employed to confirm endosomal GLP-1R localisation to ERMCSs. We first performed an *in situ* Correlative Light and Electron Microscopy (CLEM) approach at room temperature to correlate ultrastructural features with positive fluorescent signals for SNAP/FLAG-hGLP-1R, EGFP-VAPB, and mitochondria. To this end, INS-1 832/3 SNAP/FLAG-hGLP-1R cells were labelled at the cell surface with a membrane impermeable fluorescence SNAP-tag probe prior to stimulation with exendin-4. Internalised SNAP/FLAG-hGLP-1R was detected colocalised with EGFP-VAPB, often close to mitochondria (Fig. 3d). Correlation of the confocal slice to the corresponding TEM tomogram (Fig. 3e) revealed two mitochondrial volumes in close contact with the ER and a vesicle positive for SNAP/FLAG-hGLP-1R, indicative of a GLP-1R-positive endosome (Fig. 3f). Similar results were obtained using a cryo-CLEM approach, with endosomal SNAP/FLAG-hGLP-1R colocalised with EGFP-VAPB in close proximity to mitochondria (Supplementary Fig. 4a), and correlation of confocal and FIB-SEM data (Supplementary Fig. 4b) revealing a GLP-1R-positive endosome docked to the ER in the vicinity of a mitochondria (Supplementary Fig. 4c).

These results were replicated by an immuno-EM approach in primary mouse islets transduced with a SNAP/FLAG-hGLP-1R-expressing adenovirus, by labelling cell surface SNAP/FLAG-hGLP-1R in intact living islets with membrane-impermeable SNAP-biotin plus streptavidin conjugated to 5-nm gold particles prior to exendin-4 stimulation and TEM processing. TEM imaging of ultrathin (70-nm) sections from resin-embedded islets from above revealed 5-nm gold-positive endosomes (indicative of the presence of SNAP/FLAG-hGLP-1R) forming contacts with both the ER and mitochondria (Fig. 3g).

Active GLP-1R engages with the AKAP SPHKAP at ERMCSs via shared VAPB binding.

Amongst the interactors enriched for active GLP-1R binding in our MS interactome analysis, we identified the A-kinase anchoring protein (AKAP) SPHKAP, a paralog of AKAP11 that binds to two RI subunits of the PKA holoenzyme[28], with both SPHKAP and AKAP11 previously shown to localise to mitochondria (SPHKAP)[29], or to regulate mitochondrial metabolism (AKAP11)[30]. Both SPHKAP and AKAP11 harbour a FFAT (two phenylalanines in an acidic tract) motif[31, 32], a specific short protein sequence that binds to the Major Sperm Protein (MSP) domain of VAPs[33] (Supplementary Fig. 5a), which, in the case of SPHKAP, can be regulated by phosphorylation (pFFAT)[32]. Agreeably, SPHKAP has previously been shown to interact with VAP proteins in neurons[34]. Beyond neurons, SPHKAP is also expressed in metabolically relevant tissues, including pancreatic islets and intestinal K- and L-cells, and has been previously shown to play an important role in both incretin secretion and incretin-dependent glucoregulation[35, 36]. Additionally, SPHKAP mRNA expression is decreased in a published RNA Seq database of islets from *db*/*db* *versus* WT mice

(Supplementary Fig. 5b), and genome-wide significant associations between *SPHKAP* gene variants, T2D risk, and high BMI have been found in meta-analyses from four separate genome-wide association studies (GWAS) in humans[37, 38, 39, 40] (Supplementary Fig. 5c,d). The effect of *SPHKAP* variants in T2D *versus* high BMI is tightly correlated (Supplementary Fig. 5e), suggesting a shared mechanism of action for SPHKAP in both disorders where GLP-1RAs are known to be effective. Additionally, our own genetic analysis demonstrated a significant association between *SPHKAP* gene coding variants and random blood glucose levels in whole exome sequencing (WES) data from UK Biobank (UKBB) individuals without diabetes (Supplementary Fig. 5f), strongly supporting a role for SPHKAP in the regulation of β-cell function.

We therefore next investigated the potential involvement of SPHKAP in GLP-1R signal transduction from ERMCSs. We first confirmed the active GLP-1R–SPHKAP interaction inferred from our MS interactome analysis by measuring increased co-immunoprecipitation of SPHKAP-EGFP (Fig. 4a,b, Control RNAi conditions; Supplementary Fig. 6a), as well as endogenous SPHKAP (Supplementary Fig. 6b), with SNAP/FLAG-hGLP-1R in exendin-4-stimulated *versus* vehicle-treated INS-1 832/3 SNAP/FLAG-hGLP-1R cells. We next determined that this interaction requires VAPB, as it is abrogated by VAPB knockdown (Fig. 4a,b, Supplementary Fig. 6a). Confocal analysis of SPHKAP-EGFP localisation in WT INS-1 832/3 cells revealed that this AKAP localises to an intracellular network closely apposed to, but not inside, mitochondria (Fig. 4c, Control RNAi panels; Supplementary Fig. 6c). Labelling of the ER network with the fluorescent dye ER-Tracker revealed a punctate localisation of SPHKAP-EGFP along ER membranes (Fig. 4d). Localisation of SPHKAP-EGFP to these ER loci required VABP, as it was lost in VAPB RNAi-treated cells (Fig. 4c, VAPB RNAi panels). We next generated a mutant version of SPHKAP-EGFP harbouring a point mutation in its pFFAT motif (SPHKAP-EGFP A215E, DFLT**A**SE to DFLT**E**SE). This strategy was based on previous structural data showing that position 5 of the FFAT core motif is positioned within a hydrophobic pocket in the MSP domain of VAP[41], with previous studies indicating that introducing a negative charge in this position causes a steric hindrance which effectively disrupts FFAT motif-VAP interaction[42]. Agreeably, our SPHKAP-EGFP pFFAT motif mutant lost both its increased binding to exendin-4-stimulated SNAP/FLAG-hGLP-1R (Supplementary Fig. 6d) and its localisation to the ER network in close proximity of mitochondria (Supplementary Fig. 6e), demonstrating that SPHKAP localisation to ERMCSs and its engagement with active GLP-1R depends on SPHKAP binding to VAPB via its pFFAT motif.

ERMCS-localised GLP-1R-dependent PKA signalling requires SPHKAP.

We next tested the effect of SPHKAP downregulation on GLP-1R-dependent downstream signalling. SPHKAP knockdown efficiency in INS-1 832/3 cells was validated against both endogenous SPHKAP (Supplementary Fig. 6f,g) and SPHKAP-EGFP (Supplementary Fig. 6h). Loss of SPHKAP did not affect the interaction between the receptor and VAPB (Supplementary Fig. 7a,b), indicating that GLP-1R is recruited to VAPB-positive ERMCSs independently of SPHKAP. Loss of SPHKAP also did not affect the capacity for the receptor to generate cAMP following exendin-4 stimulation of WT INS-1 832/3 cells (Fig. 4e). In contrast, while global PKA responses to exendin-4 were not affected (Fig. 4f), exendin-4-induced OMM-localised PKA activity was blunted by SPHKAP downregulation (Fig. 4g). Finally, we employed a similar modified FluoSTEP system to the one shown in Fig. 2, this time adapted to assess VAPB-localised PKA activity in response to exendin-4 stimulation in Control *versus* SPHKAP RNAi-treated WT INS-1 832/3 cells (see Supplementary Fig. 7c for a schematic of this method). Results showed that exendin-4 stimulation does indeed trigger VAPB-localised PKA activity in WT INS-1 832/3 cells, and that this activity requires SPHKAP (Fig. 4h), presumably via SPHKAP binding to and recruitment of PKA to ERMCSs.

Control of mitochondrial and β-cell function by SPHKAP-dependent GLP-1R signalling.

We next assessed the effect of ERMCS-localised GLP-1R signalling in the control of INS-1 832/3 mitochondrial function. Exendin-4 stimulation triggered a small increase in mitochondrial membrane potential under 6 mM glucose conditions, with this response enhanced under increased (20 mM) glucose concentrations. Both membrane potential rises were however significantly reduced in SPHKAP RNAi-treated *versus* Control WT INS-1 832/3 cells (Fig. 5a). Accordingly, ATP increases in response to exendin-4 exposure were significantly reduced following SPHKAP knockdown (Fig. 5b, Supplementary Fig. 7d), suggesting a defect in GLP-1R-dependent mitochondrial respiration. We further determined the impact of ERMCS-localised GLP-1R signalling on β-cell function by analysing acute insulin secretion responses and β-cell survival to ER stress induction downstream of GLP-1R stimulation in SPHKAP RNAi-treated *versus* Control WT INS-1 832/3 cells. Exendin-4-stimulated insulin secretion was significantly reduced in SPHKAP RNAi *versus* control conditions (Fig. 5c, Supplementary Fig. 7e), with no effect of SPHKAP over-expression (Supplementary Fig. 7f). Additionally, the anti-apoptotic effect of exendin-4 in cells exposed to thapsigargin (to trigger ER stress) was blunted following SPHKAP knockdown (Fig. 5d). Finally, we measured exendin-4-induced mitochondrial and ER calcium responses in Control *versus* SPHKAP RNAi-treated WT INS-1 832/3 cells. Increases in both ER and mitochondrial calcium in response to exendin-4 stimulation were apparent in these cells. While ER responses were not affected by SPHKAP knockdown (Supplementary Fig. 7g), we detected a delay in the mitochondrial calcium response peak time in SPHKAP RNAi *versus* Control RNAi-treated WT INS-1 832/3 cells (Supplementary Fig. 7h).

As SPHKAP has previously been shown to bind to the mitochondrial cristae junction regulator and MICOS complex component MIC19[29], a prominent PKA substrate involved in both cristae assembly during mitochondrial remodelling[43] and regulation of ERMCSs[11], we next tested whether exendin-4 stimulation would trigger MIC19 phosphorylation in WT INS-1 832/3 cells using a MIC19 immunoprecipitation strategy coupled with Western blotting with an antibody raised against PKA phosphosites (RRxpS/T)[44]. Exendin-4 exposure resulted in a ~5-fold increase in PKA-specific MIC19 phosphorylation, an effect that was potentiated by the adenylate cyclase activator forskolin (Fig. 5e). Furthermore, knockdown of either SPHKAP or VAPB in INS-1 832/3 cells led to the loss of exendin-4-induced MIC19 phosphorylation, consistent with our hypothesis that GLP-1R-SPHKAP interaction at VAPB-positive ERMCSs is responsible for the PKA-dependent phosphorylation of this MICOS complex component (Supplementary Fig. 7i).

Control of mitochondrial morphology by SPHKAP-dependent ERMCS-localised GLP-1R signalling.

As the main role of MIC19 is to orchestrate mitochondrial cristae assembly[45] and enable the transfer of lipid precursors during mitochondrial remodelling[11], we next assessed whether GLP-1R stimulation would play a role in mitochondrial remodelling processes in INS-1 832/3 cells, and whether this would be affected by SPHKAP knockdown. We first investigated if acute exendin-4 stimulation triggers changes in mitochondrial turnover. Despite no detectable changes in mitochondrial DNA copy number after 30 minutes of exendin-4 exposure in Control *versus* SPHKAP RNAi-treated, or in GLP-1R KO INS-1 832/3 cells (Supplementary Fig. 7j), acute (10-minute) stimulation of WT INS-1 832/3 cells with exendin-4 triggered increased mitophagy, assessed using an mKeima-based assay[46], an effect not present following SPHKAP downregulation (Fig. 5f). Further evidence of exendin-4-induced mitophagy was obtained by CLEM analysis of INS-1 832/3 SNAP/FLAG-hGLP-1R cells, where we could find instances of SNAP/FLAG-hGLP-1R-positive endolysosomes surrounded by mitochondria (Supplementary Fig. 8a,b). We also detected increased

recruitment of the mitochondrial fission protein mCherry-Drp1 to mito-BFP-expressing mitochondria in exendin-4-stimulated *versus* vehicle-exposed WT INS-1 832/3 cells (Fig. 5g, Supplementary Fig. 8c, Supplementary Movies 3 and 4). Drp1 phosphorylation at Serine 616, which, unlike Serine 637[47], is important for regulating mitochondrial fission and is not directly PKA-dependent[48], was not modified by acute exendin-4 exposure in Control RNAi-treated cells, but was progressively lost 15 minutes post-exendin-4 stimulation in SPHKAP RNAi-treated WT INS-1 832/3 cells (Fig. 5h).

We next directly assessed changes in mitochondrial morphology by confocal microscopy imaging of MitoTracker-labelled mitochondria in vehicle *versus* exendin-4-stimulated WT INS-1 832/3 cells. Here, we employed a similar approach to [49] to manually score cells by mitochondrial phenotype into three categories: long tubular (referred to as “hyperfused”), intermediate/short tubular (referred to as “tubular”) and fragmented. Results showed that 10 minutes of exendin-4 exposure completely remodels the mitochondrial network from a predominantly hyperfused to a fragmented phenotype (Fig. 6a). As expected, and serving as validation of our classification approach, this remodelling did not take place in INS-1 832/3 cells lacking the GLP-1R (GLP-1R KO) (Fig. 6b). We further confirmed our results by re-analysing the data from above using the automated Mitochondria Analyzer plugin in Fiji to determine changes in mitochondrial form factor, which provides information on mitochondrial shape, as well as mitochondrial mean area (Supplementary Fig. 8d). Agreeably, we found a significant reduction on mitochondrial form factor and mean area, indicative of remodelling, upon exendin-4 stimulation of INS-1 832/3, but not of INS-1 832/3 GLP-1R KO cells.

Next, we performed mitochondrial morphology analysis of WT INS-1 832/3 cells treated with Control *versus* SPHKAP RNAi prior to vehicle or exendin-4 exposure (Fig. 6c). While exendin-4 triggered a similar degree of mitochondrial network remodelling as above in Control RNAi-treated cells, SPHKAP knockdown resulted in disrupted mitochondrial morphology at vehicle conditions, which somewhat resembled that of exendin-4-stimulated Control RNAi-treated cells in terms of tubularity but had further visual abnormalities. Moreover, exendin-4 stimulation had no effect on the mitochondrial morphology of SPHKAP RNAi-treated cells. These results were validated with the Mitochondria Analyzer plugin in Fiji, which showed reduced mitochondrial form factor and mean area following exendin-4 exposure of Control RNAi-treated cells, with SPHKAP RNAi-treated cells under vehicle conditions showing similar values to those of exendin-4-stimulated control cells (Supplementary Fig. 8e). However, with this analysis method, we also detected an apparent increase in form factor and mitochondrial mean area in exendin-4-stimulated *versus* vehicle-treated SPHKAP RNAi-treated cells, an effect opposite to that triggered by exendin-4 in control conditions.

To better visualise the changes in mitochondrial morphology under these different conditions, we also performed z-series analysis of confocal sections across whole cells, represented as MIPs in Fig. 6d, as well as Stimulated Emission Depletion (STED) microscopy analysis of mitochondrial morphologies using the fixable STED-compatible mitochondrial dye PKmito ORANGE FX (Fig. 6e), with Control *versus* SPHKAP RNAi-treated cells showing similar changes in mitochondrial morphology as those described above.

Finally, we also performed high-resolution TEM imaging for precise quantification of mitochondrial area and number of cristae per mitochondria in ultrathin (70-nm) sections on resin-embedded Control *versus* SPHKAP RNAi-treated WT INS-1 832/3 cells, as well as INS-1 832/3 GLP-1R KO cells, both under vehicle conditions and following exendin-4 stimulation. In agreement with our previous results, we measured an exendin-4-induced reduction in both parameters in Control RNAi-treated cells, but no change in response to exendin-4 in either SPHKAP RNAi-treated or in GLP-1R KO cells (Fig. 7a,b). Interestingly, the mitochondrial morphology changes triggered by exendin-4 in Control RNAi-treated cells were accompanied by a significant reduction in ERMCS length, which appeared already

reduced under vehicle conditions, without further effect of exendin-4, following SPHKAP downregulation (Fig. 7c). We also detected a reduction in the number of ERMCSs per mitochondrial area in exendin-4-stimulated *versus* vehicle-exposed WT INS-1 832/3 cells using a splitFAST approach as in [50] (Fig. 7d,e).

Active GLP-1R localisation and SPHKAP-dependent GLP-1R signalling at ERMCSs in primary mouse and human islets.

To validate the interaction of GLP-1R with VAPB and SPHKAP at ERMCSs in a physiologically relevant setting with endogenous levels of receptor expression, proximity ligation assays (PLAs) were performed in purified mouse primary islets using one of the few existing validated mouse GLP-1R antibodies from the Developmental Studies Hybridoma Bank[51, 52, 53], with GLP-1R–VAPB and GLP-1R–SPHKAP interactions readily observed in exendin-4-stimulated islets (Fig. 8a, Supplementary Fig. 9a). To verify that these interactions are present within pancreatic β-cells, we counterstained both vehicle and exendin-4-stimulated islets processed for GLP-1R–SPHKAP PLA for insulin (Supplementary Fig. 9b). Next, to analyse the functional impact of SPHKAP downregulation on islet function, we employed a lentiviral shRNA approach to knock-down SPHKAP on intact islets, as most functional outputs from primary islets cannot be optimally recapitulated with dispersed islet cells due to the loss of important intra-islet cell-cell interactions. Lentiviral transduction of cells within intact islets is restricted to the outermost cell layers so that only a small fraction of cells (which we estimate at ~25% of the total) is effectively transduced. However, those represent a higher functional cell pool due to necrosis of the islet core in non-vascularised isolated islets[54], so that it is still possible to assess potential functional differences from a relatively small percentage of transduced cells. Accordingly, we could only detect a tendency for reduced *SPHKAP* mRNA levels in whole islets transduced with SPHKAP *versus* Control shRNA lentiviruses (Supplementary Fig. 9c), which nevertheless suggests a good level of downregulation from the pool of transduced cells. We next analysed some key signalling outcomes from these transduced islets. As for WT INS-1 832/3 cells, while we could measure increased ATP outputs from exendin-4-stimulated *versus* vehicle-treated Control shRNA-transduced islets, this effect was no longer present in islets transduced with SPHKAP shRNA (Fig. 8b). Exendin-4 exposure also led to a significant reduction in the level of reactive oxygen species (ROS) in Control shRNA islets exposed to the ER stress drug thapsigargin, but this effect was no longer present in SPHKAP shRNA-transduced islets, which presented with generally higher ROS levels than the corresponding control islets (Fig. 8c). Finally, while the effect of partial SPHKAP knockdown in the acute potentiation of insulin secretion triggered by exendin-4 in these islets was mild, we found a small but significant increase in insulin secretion at 11 mM glucose alone in SPHKAP *versus* Control shRNA-transduced islets (Fig. 8d, left), which led to a near-significant reduction in exendin-4-induced insulin secretion fold (Fig. 8d, right), an effect which agrees with previously published results in a SPHKAP KO mouse model, with increased insulin secretion under glucose alone conditions but dampened incretin responses in islets from these mice[35].

We next assessed changes in mitochondrial morphology in intact mouse islets by confocal imaging of mitochondria from the outermost layer of islet cells, to maximise our chances of recording phenotypes from lentivirally transduced cells. We used a similar approach as in INS-1 832/3 cells to segment and classify islet cells as predominantly presenting a hyperfused, tubular or fragmented mitochondrial phenotype (see Supplementary Fig. 9d for an example of our method of islet segmentation and cell classification). Cells in WT mice islets presented a similar distribution of mitochondrial morphologies as in WT INS-1 832/3, with mitochondria primarily hyperfused or tubular under vehicle conditions but remodelling towards a more fragmented phenotype following exendin-4 exposure (Fig. 9a). Islets extracted from GLP-1R KO mice presented a higher level of hyperfused mitochondria that did not undergo remodelling with exendin-4 (Fig. 9b). As in INS-1 832/3 cells, transduction of WT islets with SPHKAP shRNA-expressing lentiviruses triggered a change in mitochondrial

morphology under vehicle conditions, with a higher degree of fragmentation *versus* control islets and no effect of exendin-4 exposure following SPHKAP downregulation (Fig. 9c).

Finally, we also performed mitochondrial morphology assessments in dispersed islet cells from WT mice transfected with Control *versus* SPHKAP siRNA, which responded similarly to transduced intact islets in terms of increased mitochondrial fragmentation following exendin-4 exposure in control conditions, but showing disturbed mitochondrial morphology under vehicle conditions, and no effect of exendin-4 exposure, in SPHKAP siRNA-treated cells (Fig. 9d). These phenotypic changes were still present when assessed as changes in mitochondrial form factor and mean area using the Mitochondria Analyser Fiji plugin with data from dispersed islet cells (Supplementary Fig. 9e).

Lasty, we repeated some of our assessments with human donor islets. PLA assays again demonstrated interactions between endogenous GLP-1R, VAPB and SPHKAP in exendin-4-stimulated human islets (Fig. 10a,b). As in mouse islets, assessment of mitochondrial morphology by confocal microscopy analysis and cell classification in intact human islets revealed predominantly hyperfused mitochondria under vehicle conditions which was rapidly remodelled by acute exendin-4 exposure to a more fragmented morphology (Fig. 10c,d).

Discussion

Mitochondrial malfunction is a prominent feature of diabetes, encompassing defects in mitochondrial structure and dynamics, ROS overproduction and apoptosis, breakdown of nutrient sensing, and metabolic uncoupling[55, 56], with strong backing evidence from human genetic studies[57, 58, 59]. Mitochondrial quality control mechanisms have been recently found to control cellular identity and maturity in metabolically relevant tissues[60], including in pancreatic β-cells, highlighting the importance that mitochondria have in the control of β-cell function. Strategies to correct the detrimental effect of T2D in affected tissues are therefore likely to involve amelioration of mitochondrial function; GLP-1RAs are no exception, with numerous reports highlighting their capacity to potentiate mitochondrial quality control mechanisms and improve mitochondrial health[6, 7, 8, 9], with mitochondrial regulation potentially key to explain their beneficial effects in metabolic tissues.

Despite the accumulating evidence around pathways engaged by the GLP-1R and other GPCRs in target tissues, there is still substantial uncertainty about the precise molecular mechanisms engaged, particularly with regards to the spatiotemporal organisation of their signalling and presence in spatially restricted subcellular (and even suborganelle) signalling hubs or nanodomains[61]. In this context, the study of MCSs has become an area of considerable importance to understand the spatial architecture of signalling, with recent reports recognising their prominent role in pancreatic β-cells in processes ranging from insulin granule biogenesis to calcium homeostasis[62, 63, 64]. In this study, we took an unbiased approach to unveil new molecular partners that might work in concert with the GLP-1R to control β-cell function, finding not only that the receptor engages with ER-endosome MCSs to organise its signalling, but that the main constituents of these inter-organelle contacts, namely the VAPs, are by a considerable margin the most prominent intracellular binding partners of active GLP-1R. This suggests that engagement of VAPs, and subsequent generation of ER-localised GLP-1R signalling, is not just one of many pathways engaged by the receptor, but the main site of action of GLP-1R following its internalisation. This also suggests that GLP-1RAs with distinct receptor internalisation *versus* lysosomal targeting propensities might differentially regulate the kinetics of this engagement, including, potentially, by slow GLP-1R internalising compounds enabling prolonged VAPB-GLP-1R interactions despite an initially reduced acute engagement, as seen in the present study, as these compounds also prevent the rapid lysosomal degradation of receptors triggered by fast internalising compounds with a high level of acute GLP-1R-VAPB engagement.

We have not only identified the engagement of active GLP-1R with ER-endosome MCSs, but also its localisation to VAPB-containing ERMCSs, from where endosomal GLP-1R assembles a newly described signalling nanodomain, enabling cAMP-dependent PKA activation at the OMM. This ERMCS-localised GLP-1R signalling hub requires the engagement of the AKAP SPHKAP, with VAPB playing a central role as the tethering factor responsible for the separate recruitments of both GLP-1R and SPHKAP to ERMCSs, the latter via the direct interaction of VAPB with the pFFAT motif of SPHKAP. Here, it is important to highlight that SPHKAP is one of the few AKAPs known to bind PKA RI instead of RII subunits[29]. This is relevant for the present study as PKA RI has been found to undergo liquid-liquid phase separation (LLPS) to form localised cAMP/PKA biomolecular condensates[65] which spatially restrict PKA activity leading to signal compartmentalisation[24], potentially explaining why the physical presence of GLP-1R at ERMCSs is required to assemble this signalling hub.

The relevance of SPHKAP for the control of β-cell function is supported by human genetic data of genome-wide significance, unveiling an association between *SPHKAP* gene variants, random blood glucose levels and T2D, as well as high BMI. As we observe a correlation between SPHKAP variant effects in T2D and high BMI (as a proxy for obesity), we propose that this AKAP might play a pleiotropic role in both disorders by the engagement of common signalling pathways in different tissues. These could potentially involve the GLP-1R, known to signal in anorectic neurons to regulate food intake as well as in pancreatic β-cells to potentiate insulin secretion and β-cell survival[66]. Alternatively, SPHKAP might engage other metabolically relevant GPCRs acting via VAPB to modulate mitochondrial function in tissues where SPHKAP is expressed, including the brain and heart[28, 34]. For example, this mechanism might potentially regulate liver mitochondrial function, a possibility supported by the previously published interaction between the closely related glucagon receptor and VAPB in hepatocytes[67]. The significance of the ERMCS-localised signalling hub identified in this study is therefore likely to extend well beyond the GLP-1R to other metabolically relevant $G\alpha_s$-coupled GPCRs. Moreover, beyond the loss of exendin-4-induced responses, we also find a significant effect of SPHKAP downregulation in mitochondrial morphology and other parameters under vehicle conditions, suggesting additional effects of this AKAP in β-cells.

Another outcome from the present study is the identification of the MICOS complex protein MIC19 as a downstream target of SPHKAP-dependent PKA phosphorylation downstream of ERMCS-localised GLP-1R activity. MIC19 is not only a key member of mitochondrial cristae junctions, responsible for the organisation of mitochondrial inner and outer membrane contacts, as well as for the architecture of respiratory complexes and the mitochondrial proton pump, but also plays a prominent role in ERMCSs, where it enables the transfer of lipid precursors for the biosynthesis of the key mitochondrial lipid cardiolipin[68], therefore connecting mitochondrial cristae organisation with the generation of membrane curvature and control of mitochondrial function afforded by cardiolipin[11]. We therefore hypothesise that GLP-1R-dependent phosphorylation of MIC19 at ERMCSs via the VAPB/SPHKAP/PKA pathway might not only highlight a direct role for the GLP-1R in the control of mitochondrial cristae architecture and dynamics, but also in the regulation of lipid precursor transfer across ERMCSs to sustain mitochondrial turnover. This is particularly relevant as alterations in cardiolipin profiles have been reported in several diseases where GLP-1RAs play beneficial roles, including Alzheimer's, Parkinson's, obesity, and T2D[69]. Interestingly, our MS interactomic analysis also identifies TAMM41, an essential enzyme for the biosynthesis of cardiolipin[70], as an active GLP-1R interactor.

Amongst the mitochondrial processes modulated by SPHKAP-dependent ERMCS-localised GLP-1R cAMP/PKA signalling, we have found acute increases in mitochondrial fission and

mitophagy, two key mitochondrial quality control mechanisms which enable the clearance of damaged, unhealthy, or old mitochondria, and hold a prominent role in the maintenance of β-cell function[56] and identity[60]. Loss of these functions can lead to impaired insulin release and glucose intolerance[71], with the present study indicating that controlling these processes is an important mechanism engaged by the GLP-1R to exert its beneficial action on β-cell function and promotion of survival under oxidative stress conditions.

Amongst the major metabolic triggers of β-cell dysfunction is glucose and lipid-induced cytotoxicity. In the context of obesity, elevated glucose and fatty acids increase insulin demand and contribute to β-cell oxidative stress. Additionally, excess free fatty acids accumulated in β-cells induce further ROS generation, contributing to increase ER stress and β-cell dysfunction. β-cell mitochondria therefore need to appropriately adapt to glucolipotoxic conditions to avoid progression towards overt T2D[72]. Changes in mitochondrial morphology have been previously associated with modified nutrient utilisation, with a strong correlation between mitochondrial fragmentation and increased fatty acid oxidation (FAO)[73], a process which is normally inhibited in β-cells under high glucose conditions to favour metabolic coupling towards insulin secretion[74], but that might be differentially modulated by the action of the GLP-1R under excess lipid conditions to enable lipid clearance and detoxification[72]. In support of this hypothesis, our MS interactome analysis indicates the association of active GLP-1R with a range of factors involved in lipid metabolism and FAO, including lipases and regulators of lipase transfer to lipid droplets (Mest[75], Copb1[76]), lipid metabolising enzymes (TMEM120A[77], Acsl4[78], Fads1[79], Chp1[80], Cds2[81], Apgat4[82]), and mitochondrial FAO and ketone body enzymes (HADHA/B[83], Bdh1[84]), as well as the ER-lipid droplet small GTPase Rab18[85], several subunits of the mitochondrial ATP synthase, the respiratory chain subunit SDHA, and the FAO-fuelled plasma membrane Na^+/K^+ pump[86]. Interestingly, a recent study has also identified ERMCSs as required for lipid radical transfer from mitochondria to the ER to reduce mitochondrial oxidative stress[87], which could represent another mechanism stimulated by ERMCS-localised GLP-1R to enhance β-cell survival under glucolipotoxic conditions.

Beyond its interaction with lipid enzymes, our MS interactome analysis also indicates that the GLP-1R binds to ERMCS-localised Sarcoendoplasmic Reticulum Calcium ATPase (SERCA) pump[88] in the ER and voltage-dependent anion-selective channel protein 2 (VDAC2) in the OMM, both involved in calcium/ion transfer across ERMCSs[89], suggesting a prominent role for the receptor in the control of intra-organelle ion homeostasis, with important implications for the regulation of mitochondrial function, ER stress responses and insulin secretion[90].

Overall, all these MS-identified interactions suggest that the effect of GLP-1R signalling at ERMCS is likely to extend well beyond MIC19 phosphorylation into a more comprehensive programme of regulation of ER, mitochondria and lipid metabolic pathways.

In summary, this investigation has unveiled the existence of a newly characterised inter-organelle signalling hub in pancreatic β-cells which involves active endosomal GLP-1R localisation to ERMCSs via VAPB binding, and engagement of the AKAP SPHKAP to enable ERMCS-restricted cAMP/PKA activity, leading to the phosphorylation of the MICOS complex and ERMCS component MIC19, as well as enhanced mitochondrial fragmentation and mitophagy and improved mitochondrial function, with important implications for the modulation of β-cell function and survival, and the potential to serve as a mechanism for GLP-1R-induced β-cell mitochondrial adaptation during metabolic stress and excess nutrient exposure. Further studies to investigate this later possibility, including examination of the effect of GLP-1R in β-cell lipid metabolism and mitochondrial nutrient utilisation under normal and glucolipotoxic stress conditions, are therefore warranted.

Methods

Cell culture

INS-1 832/3 rat insulinoma cells were maintained in RPMI-1640 at 11 mM D-glucose, supplemented with 10% fetal bovine serum (FBS), 10 mM HEPES, 2 mM L-glutamine, 1 mM pyruvate, 50 µM β-mercaptoethanol and 1% penicillin/streptomycin. INS-1 832/3 cells stably expressing SNAP/FLAG-tagged human GLP-1R (hGLP-1R) were generated by transfection of pSNAP-GLP-1R (Cisbio) into INS-1 832/3 cells lacking endogenous GLP-1R expression (INS-1 832/3 GLP-1R KO, a gift from Dr Jacqueline Naylor, AstraZeneca[91]) followed by G418 (1 mg/mL) selection. Mycoplasma testing was performed yearly. Cell culture reagents were obtained from Sigma or Thermo Fisher Scientific.

Peptides and fluorescent probes

GLP-1 was purchased from Bachem, semaglutide was from Imperial College London Healthcare NHS Trust pharmacy, and tirzepatide was a gift from Sun Pharmaceuticals. Custom analogues were from WuXi AppTec, China, and danuglipron and orforglipron were purchased from MedChemExpress. SNAP-Surface fluorescent probes were from New England Biolabs and MitoTracker™ Red CMXRos and ER-Tracker Red were from Thermo Fisher Scientific.

β-cell GLP-1R interactome

INS-1 832/3 SNAP/FLAG-hGLP-1R cells were stimulated in 6-cm dishes with vehicle or 100 nM GLP-1RA (GLP-1, exendin-4, exendin-F1 or exendin-D3) for 5 minutes. Following stimulation, cells were washed in PBS and osmotically lysed in lysis buffer (50 mM Tris-HCl, pH 7.4, 150 mM NaCl, 1% Triton X-100, 1 mM EDTA) with 1% protease inhibitor (Roche) and 1% phosphatase inhibitor cocktail (Sigma-Aldrich) at 4°C. Cell lysates were centrifuged at 12,000 g and 4°C for 10 minutes, prior to addition of 40 µL anti-FLAG M2 beads (A2220, Sigma-Aldrich) for overnight rotating incubation at 4°C to increase binding efficiency. Samples were centrifuged at 5,000 g for 30 seconds, and bead pellets washed 3x in 500 µL wash buffer (50 mM Tris-HCl, 150 mM NaCl, pH 7.4) before storage at -80°C until further analysis.

Beads were resuspended in 150 µL 1 M urea in 20 mM HEPES pH 8.0 with 1 mM DTT, followed by addition of 1.5 µg Trypsin gold (Promega) with overnight digestion at 37°C. Supernatants were subsequently acidified with 0.5% trifluoroacetic acid (TFA), followed by desalting using reversed-phase spin tips (Glygen Corp) and drying using vacuum centrifugation. Dried peptides were resuspended in 0.1% TFA and Liquid Chromatography Tandem Mass Spectrometry (LC-MS/MS) performed as previously described[92] using an Ultimate 3000 nano-HPLC coupled to a Q-Exactive mass spectrometer (Thermo Scientific) via an EASY-Spray source. Peptides were loaded onto a trap column (Acclaim PepMap 100 C18, 100 µm × 2 cm) at 8 µL/minute in 2% acetonitrile and 0.1% TFA. Peptides were then eluted on-line to an analytical column (Acclaim Pepmap RSLC C18, 75 µm × 75 cm). A 90-minute stepped gradient separation was used with 4-25% acetonitrile 80%, formic acid 0.1% for 60 minutes, followed by 25-45% for 30 minutes. Eluted peptides were analysed by Q-Exactive operating in positive polarity and data-dependent acquisition mode. Ions for fragmentation were determined from an initial MS1 survey scan at 70,000 resolution (at m/z 200), followed by higher-energy collisional dissociation of the top 12 most abundant ions at a resolution of 17,500. MS1 and MS2 scan AGC targets were set to 3e6 and 5e4 for a maximum injection time of 50 and 75 miliseconds, respectively. A survey scan range of 350 – 1800 m/z was used, with a normalised collision energy set to 27%, minimum AGC of 1e3, charge state exclusion enabled for unassigned and +1 ions and a dynamic exclusion of 45 seconds.

Data was processed using the MaxQuant software platform (v1.6.10.43)[93], with database searches carried out by the in-built Andromeda search engine against the Swissprot Rattus Norvegicus database (Downloaded – 21st May 2022, entries: 8,132) concatenated with the human GLP-1R protein sequence. A reverse decoy database approach was used at a 1% FDR for peptide spectrum matches and protein identifications. Search parameters included: maximum missed cleavages set to 2, variable modifications of methionine oxidation, protein N-terminal acetylation, asparagine deamidation and cyclisation of glutamine to pyroglutamate.

Label-free quantification was enabled with an LFQ minimum ratio count of 1. Proteins were filtered for those containing at least one unique peptide and identified in all 4 biological replicates. For normalisation, proteins were ranked by fold change increase in abundance compared with control (vehicle-treated) immunoprecipitates. The resulting data was pre-processed by elimination of proteins that are non-specifically bound and residual background proteins, such as common contaminants and reverse database proteins. To further facilitate the selection of GLP-1R interactors, the following criteria were established; i) identified at least twice from four runs; ii) not nuclear proteins; and (iii) previously identified in pancreatic β-cells.

Untargeted label-free quantitation (LFQ) intensity values, normalised to hGLP-1R levels in each immunoprecipitated sample, were analysed by LFQ Analyst[94] to identify differences in levels of individual protein-GLP-1R interactions between vehicle and GLP-1RA-treated conditions. Paired t-tests adjusted for multiple comparisons using Benjamin-Hochberg false discovery rate correction and Perseus type imputations were used for statistical analysis. To generate novel information about the functional pathways represented by these potential GLP-1R interactors, we performed pathway enrichment analysis with GLP-1R binding partners exhibiting changes between vehicle and exendin-4-stimulated conditions using gProfiler.

cDNA and siRNA transfection

INS-1 832/3 cells were transfected with relevant amounts of plasmid cDNA outlined in Table 1, or siRNA outlined in Table 2, using Lipofectamine 2000 (Life Technologies) in media without antibiotics according to the manufacturer's instructions. Experiments were carried out 24-48 hours after plasmid cDNA, or 72 hours after siRNA transfection.

Name	Origin	Assay
EGFP-VAPB	Gift from Dr Emily Eden, UCL	Co-Immunoprecipitation, confocal microscopy
Venus-VAPB	Generated *in house*	NanoBRET
EGFP-VAPB P56S	Generated *in house*	Co-immunoprecipitation, insulin secretion
GLP-1R-NanoLuc	Generated *in house*	NanoBRET
pcDNA3.1+		Control empty plasmid
Dynamin1 K44A-EGFP	Addgene #34681	Co-Immunoprecipitation, confocal microscopy
Dynamin2 K44A-mRFP	Addgene #128153	Co-Immunoprecipitation, confocal microscopy
SPHKAP-EGFP	Gift from Prof John D. Scott, Howard Hughes Medical Institute[29]	Co-Immunoprecipitation, confocal microscopy
SPHKAP pFFAT mut (DFLTESE)-EGFP	Generated *in house*	Co-Immunoprecipitation, confocal microscopy

pcDNA3-mitoExRai-AKAR2	Addgene #161757	Mitochondrial PKA
pcDNA3.1(+)-ExRai-AKAR2	Addgene #161753	Global PKA
cyto-Ruby3-iATPSnFR1.0	Addgene #102551	ATP
MIC19-3xHA	Gift from Prof Toshihiko Oka, Rikkyo University[95]	Immunoprecipitation, PKA-dependent phosphorylation
SPLICS Mt-ER Long P2A	Addgene #164107	Confocal microscopy of ERMCSs
Proinsulin-NLuc	Addgene #62057	Insulin secretion
mKeima-Red-Mito-7	Addgene #56018	Mitophagy
pCAG G-CEPIA1er	Addgene #105012	ER calcium
pCAG mito-RCaMP1h	Addgene #105013	Mitochondrial calcium
pEGFPC1-hVAP-B	Addgene #104448	Cloning of pcDNA3-GFP11(x7)-VAPB
pcDNA3-GFP11(x7)-Actin	Addgene #181967	Cloning of pcDNA3-GFP11(x7)-VAPB
pcDNA3-GFP11(x7)-VAPB	Generated *in house*	FluoSTEPs assays
mito-BFP	Addgene #49151	Mitochondrial fission
mCh-Drp1	Addgene #49152	Mitochondrial fission
pcDNA3.1(+)-FluoSTEP-ICUE	Addgene #181845	FluoSTEP cAMP
pcDNA3.1(+)-FluoSTEP-AKAR	Addgene #181844	FluoSTEP PKA
4xMTS-Halo	Gift from the Avezov group, UK DRI	Mitochondrial imaging for splitFAST data
ER-RspA-NFAST and OMM-short-RspA-CFAST	Gifts from the Filadi lab, CNR Institute of Neuroscience[50]	ERMCS imaging for splitFAST data

Table 1: Plasmid cDNA origin and use.

Name	Origin
Control siRNA	Ambion™ Silencer™ Select Negative Control #1 siRNA Cat#:4390843
VAPB siRNA	Ambion™ Silencer™ Select Pre-Designed siRNA Cat#:4390771, s133396
SPHKAP siRNA	Ambion™ Silencer™ Select Pre-Designed siRNA Cat#:4390771, s164929

Table 2: siRNA origin.

Isolation and culture of pancreatic islets

WT or GLP-1R KO mice (*in house*) were humanely euthanised before inflating the pancreas through the common bile duct with RPMI-1640 medium containing 1 mg/mL collagenase (Nordmark Biochemicals). The pancreas was then dissected, incubated at 37°C for 10 minutes, and digestion halted with cold RPMI-1640 supplemented with 10% FBS (F7524,

Sigma-Aldrich) and 1% (v/v) penicillin/streptomycin solution (15070-063, Invitrogen). Mouse islets were subsequently washed, purified using a Histopaque gradient (Histopaque-1119 and Histopaque-1083, Sigma-Aldrich) and rested overnight at 37°C in a 95% O_2 / 5% CO_2 incubator before performing experiments in mouse islet culture medium (RPMI-1640 with 11 mM D-glucose, supplemented with 10% FBS and 1% penicillin/streptomycin).

Human islets were received from the isolation unit at the Centre Européen d'Etude du Diabète (CEED), Strasbourg, or from isolation centres ascribed to the Integrated Islet Distribution Program (IIDP), National Institute of Diabetes and Kidney Diseases (NIDDK), National Institutes of Health (NIH), USA, with all ethical approvals in place. Human islets were cultured on arrival in RPMI-1640 medium supplemented with L-glutamine, 10% FBS, 1% penicillin/streptomycin solution, 0.25 µg/mL amphotericin B, and 5.5 mM glucose at 37°C in a 95% O_2 / 5% CO_2 incubator. Donor characteristics are indicated in Table 3.

DATE OF ARRIVAL	SEX	AGE	BMI	SOURCE	C.O.D.
14.12.23	M	34	24.4	CEED	Anoxia
29.01.24	M	71	29.75	CEED	Stroke
15.03.24	M	61	30	CEED	Stroke
23.10.24	F	59	38.8	CEED	Stroke
01.11.24	F	64	23.8	IIDP	Head trauma
15.11.24	F	23	32.5	IIDP	Head trauma
16.12.24	F	55	29.5	IIDP	Stroke

Table 3: Details of human islet donors.

Islet shRNA transduction

Mouse islets were transduced with Control or SPHKAP shRNA-expressing lentiviral particles (MISSION® shRNA, Target Clone ID TRCN0000088765 mouse *SPHKAP*, Sigma Aldrich) at an MOI of 1 and cultured for 72 hours before experiments.

Co-immunoprecipitation

INS-1 832/3 SNAP/FLAG-hGLP-1R cells were seeded in 6-well plates at 1.2×10^6 cells per well and incubated overnight. Cells were stimulated in normal media with 100 nM exendin-4 or vehicle for 5 minutes at 37°C, washed once with ice cold PBS and lysed with 1 mL lysis buffer supplemented with 1% phosphatase inhibitor cocktail (Sigma-Aldrich) and 1% complete EDTA-free protease inhibitor cocktail (Sigma-Aldrich). Cell lysates were centrifuged at 12,000 g for 10 minutes, and supernatants added to 40 µL anti-FLAG M2 beads (Sigma Aldrich) or anti-HA Magnetic beads (Thermo Fisher Scientific) and incubated at 4°C overnight. Beads were washed 3x in 500 µL wash buffer and proteins eluted with urea buffer (200 mM Tris-HCl, pH 6.8; 5% w/v SDS, 8 M urea, 100 mM dithiothreitol, 0.02% w/v bromophenol blue) at 37°C for 10 minutes before SDS-PAGE and Western blot analysis.

SDS-PAGE and Western blotting

Samples were loaded onto 10% SDS-polyacrylamide gels then transferred to 0.45-µm PVDF membranes and blocked with 5% skimmed milk [or 5% bovine serum albumin (BSA) for anti-phospho antibodies] in TBS buffer supplemented with 0.1% Tween 20 (TBS-T). Membranes were incubated with primary antibody overnight diluted in TBS-T/milk (or TBS-T/BSA for anti-phospho antibodies) at 4°C, washed in TBS-T and incubated for 1 hour at RT with HRP-conjugated secondary antibody in TBS-T/milk. Following a further 3x washes in TBS-T,

membranes were developed with Clarity Western ECL substrate (BioRad) and imaged on a Biorad ChemiDoc or in a Xograph Compact X5 processor with Fuji medical X-ray films. Specific band densities were quantified in Fiji. The following antibodies were used (source, catalogue number, dilution): rabbit anti-VAPB (Antibodies.com, A14703, 1:5,000); rabbit anti-SNAP tag (New England Biolabs, P93105, 1:5,000); mouse anti-SPHKAP (kind gift from Dr Nicholas Vierra, University of Utah[34], L131/17, 1:1,000); mouse anti-Tubulin (Sigma Aldrich, T-5168, 1:2,000); rabbit anti-HA tag (Abcam, Ab9110, 1:1,000); rabbit anti-GFP (Proteintech, 50430-2-AP, 1:2,000); rabbit anti-phospho-PKA Substrate (RRXS*/T*) (Cell Signaling, 9624, 1:1,000); rabbit anti-Drp1 (D6C7) (Cell Signaling, 8570S, 1:1,000); rabbit anti-phospho-Drp1 Ser616 (D9A1) (Cell Signaling, 4494S, 1:1,000); mouse anti-human Tom20 (F-10) (Santa Cruz Biotechnology, sc-17764, 1:1,000); goat anti-mouse IgG-HRP (Abcam, ab205719, 1:5,000); goat anti-rabbit IgG HRP (Abcam, ab205718, 1:2,000).

SNAP/FLAG-hGLP-1R localisation by confocal microscopy

Cells seeded onto 35-mm glass-bottom dishes (MatTek) were transfected with the indicated constructs. SNAP-FLAG-hGLP-1R was labelled for 15 minutes at 37°C with SNAP-Surface Alexa Fluor 546 or 647 in full media prior to stimulation with 100 nM exendin-4 and imaging in a Leica Stellaris 8 inverted confocal microscope with a 63x/1.40 oil immersion objective with Lightning confocal super resolution modality from the Facility for Imaging by Light Microscopy (FILM) at Imperial College London. Mouse islets were transduced 24 hours prior to imaging with an adenoviral SNAP/FLAG-hGLP-1R vector (custom made by VectorBuilder) at a MOI of 1 and subsequently labelled for 10 minutes at 37°C with SNAP-Surface Alexa Fluor 647 before 5-minute stimulation with the indicated agonists and imaging of whole islets in the same microscope as above. Images were analysed in Fiji.

Transmission electron microscopy (TEM)

Cells and islets were prepared for TEM and imaged as previously described[17]. For SNAP/FLAG-hGLP-1R gold labelling, INS-1 832/3 SNAP/FLAG-hGLP-1R cells grown on Thermanox coverslips (Agar Scientific), or mouse islets transduced with SNAP/FLAG-hGLP-1R adenoviruses, were labelled with 2 μM cleavable SNAP-Surface biotin probe (kind gift of Dr Ivan Corrêa Jr, New England Biolabs) in full media, followed by incubation with 5 μg/mL NaN_3-free Alexa Fluor 488 Streptavidin, 5 nm or 10 nm colloidal gold conjugate (Thermo Fisher Scientific) to label SNAP/FLAG-hGLP-1R prior to stimulation with 100 nM exendin-4, fixation and processing for conventional TEM. Cells or islets were fixed at room temperature for 20 minutes in 2% PFA + 2% glutaraldehyde in 0.1 M sodium cacodylate, washed 2x with 0.1 M sodium cacodylate and 1x with ddH_2O, and then post-stained on ice with 2% osmium tetroxide for 1 hour followed by 1% tannic acid at room temperature for 45 minutes, and washed 2x in 0.05 M sodium cacodylate before stepwise dehydration in 70%, 90%, and 100% EtOH and Epon resin embedding. Cells mounted on Epon stubs and resin-embedded islets in moulds were baked at 65°C overnight. Samples were trimmed and cut *en face* with a diamond knife (DiATOME) in a Leica Ultracut UCT 6 ultramicrotome before examination on an FEI Tecnai G2-Spirit TEM. Images were acquired in a charge-coupled device camera (Eagle) and analysed in Fiji. Mitochondrial area, number of cristae per mitochondria and ERMCS length was determined as in [96] by manually drawing mitochondria and ERMCSs visible from the TEM micrographs.

GLP-1R–VAPB interaction assay by NanoBRET

INS-1 832/3 cells were co-transfected with 1 µg Venus-VAPB (generated *in house* from EGFP-VAPB) and 0.5 µg GLP-1R-NanoLuc[97]. NanoBRET assays were carried out as previously described[97]. Briefly, 24 hours after transfection, cells were washed with PBS, detached, and resuspended in NanoGlo Live Cell Reagent (Promega) with furimazine (1:40 dilution in HBSS) and seeded into white 96-well half-area plates. A baseline reading was

taken for 5 minutes at 37°C at 460 nm for NanoLuc emission and at 535 nm for Venus emission in a Flexstation 3 microplate reader. Cells were then stimulated with or without 1 µM of the indicated agonist and luminescent signal read for 30 minutes. Ratio (535/460 nm) BRET readings were normalised to baseline and to average vehicle readings for agonist-specific responses. Areas under the curve (AUCs) were calculated for each agonist response using GraphPad Prism 10.

Global and mitochondrial PKA assays

INS-1 832/3 cells were seeded onto 35-mm glass-bottom dishes (MatTek) and transfected with enhanced excitation-ratiometric PKA biosensor pcDNA3.1(+)-ExRai-AKAR2 (for global PKA) or pcDNA3-mitoExRai-AKAR2 (for mitochondrial PKA)[26]. Cells were washed with PBS 24 hours after transfection and imaged in Krebs-Ringer bicarbonate-Hepes (KRBH) buffer (140 mM NaCl, 3.6 mM KCl, 1.5 mM $CaCl_2$, 0.5 mM $MgSO_4$, 0.5 mM NaH_2PO_4, 2 mM $NaHCO_3$, 10 mM Hepes, 0.1% BSA, saturated with 95% O_2 / 5% CO_2, pH 7.4) supplemented with 11 mM glucose and imaged ratiometrically at excitation wavelengths of 405 and 488 nm and emission of 530 nm using a Zeiss LSM-780 inverted confocal laser-scanning microscope with a 63x oil immersion objective, with images taken every 6 seconds, in a 37°C heated chamber. A baseline reading was taken for 1 minute followed by stimulation with 1 µM exendin-4 and imaging for 5 minutes before addition of 10 µM forskolin (FSK) + 100 µM isobutyl methylxanthine (IBMX) for the last 2 minutes of acquisition to record maximal responses. AUCs were calculated using GraphPad Prism 10.

cAMP assays

INS-1 832/3 cells were seeded onto 35-mm glass-bottom dishes (MatTek) and incubated overnight with the Green Up cADDis biosensor in a BacMam vector (Montana Molecular) according to the manufacturer's instructions. Cells were washed with PBS and imaged in 11 mM glucose KRBH buffer using a Nikon Eclipse Ti microscope with an ORCA-Flash 4.0 camera (Hamamatsu) and Metamorph software (Molecular Devices) with a 20x air objective and 488 nm laser, with images taken every 6 seconds, on a 37°C stage. A baseline reading was taken for 1 minute followed by stimulation with 1 µM exendin-4 for 5 minutes, and 10 µM FSK + 100 µM IBMX addition for the last 2 minutes of the acquisition for maximal responses. Raw fluorescent intensities were extracted in Fiji to plot an average intensity trace and AUCs calculated in GraphPad Prism 10.

Mitochondrial morphology assays

INS-1 832/3 cells were seeded at 50,000 cells per well in 96-well glass-bottom imaging plates (Sigma Aldrich) coated with poly-L-lysine and laminin (1:50). Primary mouse islets were dispersed by trituration with trypsin-EDTA 0.25% for 3 minutes and seeded as above, or imaged whole without dispersion. Both cells and islets were stimulated with 100 nM exendin-4 or vehicle for 10 minutes and subsequently labelled with MitoTracker Red CMXRos (Thermo Fisher Scientific), washed 1x with PBS and imaged in phenol red free RPMI-1640 in a Leica Stellaris 8 inverted confocal microscope with 63x/1.40 (islets) or 100x/1.40 (cells) oil immersion objectives. Five images were collected per condition and analysed using the Mitochondria Analyzer plugin for Fiji to determine mitochondrial mean area and form factor. Cells were also classified by mitochondrial phenotype as in [49, 98] into a) hyperfused (highly interconnected and elongated), b) tubular (mixed) or c) fragmented mitochondrial types. For INS-1 832/3 and dispersed islet cell experiments, 30 to 130 cells were analysed from *n*=4-5 independent repeats per experiment; for intact islet experiments, all visible cells in a total of 15 to 30 islets from *n*=5-6 independent repeats were analysed per experiment.

Imaging of mitochondria by STED microscopy

INS-1 832-3 cells were seeded in glass-bottom dishes (MatTek), labelled with 500 nM PKmito Orange FX (Spirochrome) for 30 minutes, washed 3x in PBS and incubated in complete media for 30 minutes to recover. Cells were then treated with vehicle or 100 nM exendin-4 in complete media for 10 minutes prior to fixation in 4% PFA and imaging in PBS using a Leica Stellaris 8 microscope in TauSTED mode with a 100x/1.40 oil immersion objective. Cells were excited at 591 nm and pulsed depletion performed at 775 nm with 750 picosecond delay at 50% intensity.

Mitochondrial membrane potential assay

INS-1 832/3 cells were seeded 35-mm glass-bottom dishes (MatTek), incubated in 3 mM glucose KRBH for 1 hour, followed by incubation with 50 µM tetramethylrhodamine (TMRE) in 3 mM glucose KRBH for 15 minutes to label active mitochondria[99]. Cells were then washed with KRBH and imaged in 3 mM glucose KRBH with images taken every 12 seconds in a 60x/1.4 oil immersion objective with a 561 nm laser in a Nikon Eclipse Ti microscope with an ORCA-Flash 4.0 camera (Hamamatsu) and Metamorph software (Molecular Devices). A baseline reading was recorded for 1 minute followed by stimulation with 1 µM exendin-4 in 6 mM glucose KRBH for 2 minutes. Glucose levels were then increased to 20 mM and cells imaged for a further 5 minutes, followed by mitochondrial hyperpolarisation using 20 µg/ml oligomycin for 5 minutes and depolarisation using 20 µM carbonyl cyanide 4-trifluoromethoxyphenylhydrazone (FCCP) for 5 minutes. Raw fluorescent intensities were extracted in Fiji to obtain average intensity traces and AUCs calculated using GraphPad Prism 10.

ATP assays

<u>By time-lapse microscopy:</u> INS-1 832/3 cells were seeded in 35-mm glass-bottom dishes (MatTek) and transfected with the ATP biosensor cyto-Ruby3-iATPSnFR1.0[100]. Cells were imaged 24 hours after DNA transfection in 11 mM glucose KRBH buffer in a Zeiss LSM-780 inverted confocal laser-scanning microscope using a 63x/1.4 oil immersion objective with a 488 nm laser, with images taken every 6 seconds. A baseline reading was recorded for 1 minute followed by stimulation with 1 µM exendin-4 for 5 minutes. Raw fluorescent intensities were extracted using Fiji to obtain average intensity traces and AUCs calculated using GraphPad Prism 10.

<u>Biochemical assay:</u> INS-1 832/3 cells seeded in 12-well plates, or mouse islets, were pre-incubated with KRBH buffer supplemented with 3 mM glucose for 30 minutes followed by stimulation with KRBH supplemented with 11 mM glucose +/- 100 nM exendin-4 for 15 minutes. Cells were lysed in KRBH + 0.1% Triton X-100 and sonicated, while islets were lysed in acidic ethanol (75% ethanol, 15 mM HCl). Samples were centrifuged at 13,200 rpm and stored at -20°C until further analysis. ATP concentrations from islets and cells were determined using the ATP Determination Kit (A22066, Thermo Fisher Scientific).

Insulin secretion assays

INS-1 832/3 cells were seeded in 6-well plates at 1.2×10^6 cells per well. For VAPB WT *versus* P56S experiments, cells were co-transfected with 40 ng proinsulin-NLuc and 200 ng of either pEGFP-VAPB, pEGFP-VAPB-P56S (generated *in house* by site directed mutagenesis from pEGFP-VAPB), or pcDNA3.1+ as a control. For SPHKAP-EGFP experiments, cells were co-transfected as above with proinsulin-NLuc and either empty EGFP or SPHKAP-EGFP. For RNAi experiments, cells were transfected with Control *versus* Target (VAPB or SPHKAP) siRNA. Cells were incubated overnight in INS-1 832/3 media at 3 mM glucose 24 hours after cDNA, and 48 hours after siRNA transfections and then pre-incubated for 30 minutes in KRBH buffer supplemented with 3 mM glucose before

stimulation in KRBH buffer supplemented with 11 mM glucose +/- 100 nM exendin-4 for 60 minutes. Cell supernatants were collected to assess secreted insulin and cells lysed in KRBH + 0.1% Triton X-100 with sonication for total insulin extraction. For cDNA-transfected cells, NanoGlo Live Cell Reagent with furimazine (1:40 dilution in HBSS) was added and relative luciferase units (RLU) recorded at 460 nm using a Flexstation 3 microplate reader.

Mouse islets were incubated in KRBH buffer supplemented with 3 mM glucose for 1 hour followed by stimulation in KRBH buffer supplemented with 11 mM glucose +/- 100 nM exendin-4 for 30 minutes. Supernatants were collected and centrifuged at 1,000 rpm for 3 minutes. Islets were lysed in acidic ethanol (75% ethanol, 15 mM HCl), sonicated 3x10 seconds in a water bath and centrifuged at 13,200 rpm for 10 minutes to determine intracellular insulin concentrations.

For RNAi-transfected cells and shRNA-transduced islets, sample insulin concentration was determined using the Insulin Ultra-Sensitive HTRF Assay kit (Cisbio) according to manufacturer's instructions.

TUNEL assays

INS-1 832/3 SNAP/FLAG-hGLP-1R cells seeded onto coverslips were incubated with or without 5 µM thapsigargin in vehicle or 100 nM exendin-4-supplemented media for 8 hours before fixation and terminal deoxynucleotidyl transferase dUTP nick-end labelling (TUNEL) assay performed using the DeadEnd™ Fluorometric TUNEL system (Promega) following the manufacturer's instructions. Coverslips were mounted with ProLong™ Diamond Antifade Mountant with DAPI (Thermo Fisher Scientific) and imaged for fluorescein and DAPI (to assess total cell number) in a Zeiss LSM-780 inverted confocal laser-scanning microscope with a 20x/0/8 air objective. The percentage of TUNEL positive cells was calculated in Fiji from 5 regions per coverslip.

Proximity ligation assays (PLAs)

Mouse and human islets were stimulated with vehicle or 100 nM exendin-4 in full media for 10 minutes at 37°C. Islets were washed with PBS and fixed for a minimum of 1 hour. Islets were washed again with PBS and processed by PLA with the NaveniFlex Tissue MR Red kit (Navinci) following the manufacturer's instructions, with an extra permeabilisation step. Antibody pairs for mouse islets were mouse anti-mouse GLP-1R Ab Mab 7F38 (DSHB) and either rabbit anti-VAPB (A14703, Antibodies.com), or rabbit anti-mouse SPHKAP (36690, kind gift from Dr Nicholas Vierra, University of Utah[34]); antibody pairs for human islets were mouse anti-human GLP-1R Mab 3F52 (DSHB) and either rabbit anti VAPB (A14703, Antibodies.com), or rabbit anti-human SPHKAP (HPA042499, Atlas Antibodies). For insulin co-staining, islets were further incubated with anti-insulin antibody (IR002, Dako Agilent Technologies) overnight followed by secondary anti-guinea pig Alexa Fluor 647 (A21450, Life Technologies) for 1 hour. Islets were imaged using the confocal settings on a Leica Stellaris STED FALCON microscope and a 40x/0.8 air objective.

Room temperature Correlative Light and Electron Microscopy (CLEM)

The CLEM protocol was adapted from [101]. Briefly, INS-1 832/3 SNAP/FLAG-hGLP-1R cells were seeded on gridded coverslips (MatTek) and transfected with EGFP-VAPB before labelling with MitoTracker Red CMXRos and SNAP-Surface Alexa Fluor 647 and stimulation with 100 nM exendin-4 for 5 minutes. Cells were initially fixed for confocal microscopy with 4% PFA + 0.1% glutaraldehyde, and confocal stacks acquired with a C2+ confocal microscope (Nikon) and a 60x oil immersion objective. After fluorescence imaging, cells were additionally fixed for EM with 4% PFA + 2.5 % glutaraldehyde in sodium phosphate buffer. Samples were further processed according to a protocol modified from [102] using osmium

tetroxide (OsO_4) and thiocarbohydrazide (TCH). In brief, samples were incubated in a 2% aqueous OsO_4 solution containing 1.5% potassium ferrocyanide and 2 mM $CaCl_2$ (30 minutes on ice), washed in 1% TCH, rinsed in ddH_2O and incubated again in 2% OsO_4. After washing, samples were stained *en bloc* with 1% uranyl acetate (UA), rinsed in ddH_2O and dehydrated in a graded series of ethanol. Samples were embedded into epoxy resin Embed812 (Science Services). After resin curing at 60°C, the coverslip was removed by dipping into liquid nitrogen. The block was trimmed to a region identified during confocal imaging and serial sections with a thickness of 300 nm cut. Section post-staining was performed with 2% UA in methanol and 1% lead citrate in ddH_2O. After application of 15-nm colloidal gold beads, sections were imaged in a 300 kV Thermo Fisher F30 electron microscope. Tilt series were acquired at steps of 1° ranging from -63° to +63°. Tomograms were reconstructed with the IMOD software package[103]. Correlation of confocal images and tomogram slices was done with the EC-CLEM plugin[104] in Icy[105]. Segmentation of the tomograms was performed manually with Microscopy Image Browser[106]. 3D rendering of the segmentation was performed with ORS Dragonfly (www.theobjects.com/dragonfly/index.html).

Cryo-CLEM

INS-1 832/3 SNAP/FLAG-hGLP-1R cells previously transfected with EGFP-VAPB were plated onto glow discharged (30 seconds, 20 mAmp) poly-L-lysine-coated Quantifoil R2/2 200 mesh gold EM grids (Electron Microscopy Sciences). Cells were labelled with 500 nM PKmito Orange FX (Spirochrome) and SNAP-Surface Alexa Fluor 647 before stimulation with 100 nM exendin-4 in complete media for 10 minutes. Grids were subsequently plunge-frozen in condensed ethane using a Vitrobot and stored in liquid N_2 for further analysis.

The clipped plunge-frozen grids were loaded into the Zeiss correlative cryo-holder which can be transferred into the cryo-LSM and the cryo-FIB-SEM without further removal from the holder. For cryo-confocal data acquisition, the cryo-holder was transferred onto the cryo-Linkam stage (Linkam Scientific) and mounted onto a ZEISS Axio Imager.Z2 fitted with a LSM900 confocal scan head equipped with 3 confocal channels, including the Airyscan 2 detector for super resolution. Low magnification objectives (C Epiplan-Apochromat 5x/0.2 DIC, C Epiplan-Apochromat 10x/0.4 DIC) were used for overviews, and a LD EC Epiplan-Neofluar 100x/0.75 DIC used for high resolution. Images were acquired using the following settings: 488 nm, 561 nm and 640 nm excitation with emission bands of 493-551 nm, 553-612 nm and 613-700 nm. Reflection and brightfield channels were additionally acquired for correlation of light microscopy with SEM images. Confocal images were processed with LSM Plus (linear Wiener deconvolution). For highest resolution, Airyscan detection was used with the following settings: 488 nm, 561 nm and 640 nm excitation with emission bands of 492-549 nm, 564-611 nm and 644-700 nm and images processed using the Airyscan joint deconvolution algorithm. For cryo FIB-SEM data acquisition, the correlative cryo-holder was transferred into the Zeiss Crossbeam 550 equipped with a Quorum cryo stage. The transfer is done through the Quorum Prep Chamber attached to the FIB-SEM chamber. Inside the chamber, the sample surface was sputter-coated with platinum with a current of 5 mA for 45 seconds to make the surface conductive for SEM imaging and FIB milling. After insertion, the FIB-SEM coordinate system was aligned with respect to the LSM dataset using the ZEN software (Zeiss) and ROIs acquired in the LSM relocated and imaged in the FIB-SEM. The sample was then tilted to 54° (perpendicular to the FIB) and a cold platinum deposition applied to minimize the curtaining effect (vertical stripes in the SEM images that result from uneven milling of the sample due to roughness of the sample surface). For this purpose, the gas injection system (GIS) nozzle was inserted at ~2.5 mm from the sample surface and the unheated GIS opened for about 60 seconds resulting in a protection layer with a thickness of ~0.5 µm. Trenches were milled at the ROIs with a FIB current of 3 nA (Gallium ion energy 30 keV) to generate cross-sections. FIB-SEM volume imaging was performed with a milling current of 300 pA (Gallium ion energy 30 keV) using a slice thickness of 30 nm to obtain

SEM image stacks representing a volume of 16 µm x 12 µm x 9 µm (XYZ). The SEM images were acquired with an electron energy of 2.3 keV and an electron current of 30 pA with a pixel size of 8 nm using the InLens SE detector. The resulting FIB-SEM datasets were imported into ZEN project. After alignment of the image stack, images were processed using "destriping" (ZEN) based on the VSNR algorithm[107]. Processed image stacks were cropped to an appropriate size and a 3D alignment of the SEM and LSM stacks performed. A selected area in the aligned region of the FIB-SEM data was manually segmented, slice by slice, in Fiji, using the freehand selection tool. Outlines were saved as masks, and 3D reconstruction performed in Icy[105].

Reactive oxygen species (ROS) assays

ROS was determined using the ROS-Glo™ H_2O_2 Assay (G8820, Promega) according to the manufacturer's instructions. Briefly, islets were incubated overnight in full media containing 1 µM thapsigargin +/- 100 nM exendin-4 at 37°C and subsequently incubated in 25 µM H_2O_2 Substrate diluted in H_2O_2 Substrate Dilution Buffer plus 1 µM thapsigargin +/- 100 nM exendin-4 in a final volume of 100 µL for 3 hours at 37°C in a 5% CO_2 incubator. Media (50 µL) was combined with 50 µL ROS-Glo™ Detection Solution in a 96-well opaque plate and incubated for 20 minutes at room temperature. Relative luminescence units (RLU) were recorded in a Flexstation 3 plate reader.

Mitophagy (keima) assays

INS-1 832/3 cells were transfected with the dual-excitation ratiometric biosensor mKeima-Red-Mito-7 and seeded onto 35-mm glass-bottom dishes (MatTek). Cells were imaged 24 hours after seeding in RPMI-1640 buffer without phenol red +/- 100 nM exendin-4 by time-lapse microscopy every 12 seconds for 11 minutes in a 37°C heated chamber using a Leica Stellaris 8 inverted confocal microscope with a 40x/1.2 oil immersion objective with excitation wavelengths of 440 and 580 nm and emission wavelength of 620 nm. Ratio fluorescence intensities for the two excitation wavelengths (580/440 nm) was calculated to obtain a response trace as in [46].

ER and mitochondrial calcium assays

INS-1 832/3 cells were transfected with pCAG G-CEPIA1er (for ER calcium) or pCAG mito-RCaMP1h (for mitochondrial calcium)[108]. 24 hours after transfection, cells were washed 1x with PBS and imaged by time-lapse microscopy in RPMI-1640 without phenol red in a 40x/1.2 oil immersion objective Nikon Eclipse Ti microscope with an ORCA-Flash 4.0 camera (Hamamatsu) and Metamorph software (Molecular Devices). Mitochondrial calcium was imaged with 561 nm, and ER calcium with 488 nm excitation wavelength, with images taken every 3 seconds. A baseline reading was recorded for 1 minute followed by 1 µM exendin-4 stimulation for 3 minutes. Raw fluorescent intensities were extracted using Fiji to obtain average intensity traces and AUCs calculated using GraphPad Prism 10.

qPCR assays

<u>SPHKAP knock-down efficiency:</u> Mouse islets transduced with either Control or SPHKAP shRNA lentiviral particles were lysed using Trizol and RNA extracted using 200 µL chloroform per 1 mL Trizol and then precipitated in 500 µL isopropanol and 5 mg glycogen per mL of Trizol. RNA was washed with 75% EtOH before resuspension in ddH_2O. 250 ng of purified RNA was reverse transcribed into cDNA using the high-capacity cDNA reverse transcription kit (Applied Biosystems) and relative mRNA expression determined using FAST SYBR green chemistry qPCR and Applied Biosystems 7500 Real time PCR system.

Mitochondrial DNA copy number: INS1 832/3 cells were seeded at 300,000 cells per well on a 24-well plate. Cells were stimulated +/- 100 nM exendin-4 for 30 minutes at 37°C. Total DNA was extracted using 20 mM Tris pH 8.0, 5 mM EDTA, 400 mM NaCl, 1% SDS and 40 µg/mL proteinase K, as previously described[109], and used at 3 ng/mL for qPCR analysis of mitochondrial DNA (mtDNA) relative to genomic DNA (gDNA) as in [110]. Primers were designed using NCBI Primer Blast and validated *in silico* and then using a 1:2 standard curve of DNA ranging from 12 - 0.75 ng/mL, resulting in reaction efficiencies of 97 to 102%.

qPCR primer sequences are shown in Table 4.

Gene	Species	Fwd (5'→3')	Rev (5'→3')
HK1	rat	CCAAGCGTCTCCATAAGGCA	GTTGGTCAGCCAGACGGTAA
mitochondrial $tRNA^{Trp}$	rat	GTGAAATCAACAACCCGCCC	ATAGTCACCCCCAGGACGAA
SPHKAP	mouse	CCAAACTCTGCTACCTGCCTT	GTGATTCCACGTTGCTGGATT
Actb	mouse	CACTGTCGAGTCGCGTCC	TCATCCATGGCGAACTGGTG

Table 4: qPCR primer sequences.

Mitochondrial purification

$2x10^7$ INS-1 832/3 SNAP/FLAG-hGLP-1R cells were seeded per T75 flask in complete media and cultured overnight. Cells were then incubated in complete media + 50 mg/mL cycloheximide (CHX) for 2 hours to stop translation and prevent accumulation of immature SNAP/FLAG-hGLP-1R in the ER. Cells were then serum-starved for 30 minutes before stimulation in complete media containing CHX +/- 100 nM exendin-4 for 10 minutes. The fraction of mitochondria containing ER-associated membranes was then purified using the mitochondria isolation kit for cultured cells (Thermo Fisher Scientific) according to the manufacturer's protocol. Lysates from purified mitochondria were prepared for Western blot analysis as described above.

pcDNA3-GFP11(x7)-VAPB cloning

pcDNA3-GFP11(x7)-VAPB was cloned *in house* from pEGFP-C1-hVAPB and pcDNA3-GFP11(x7)-Actin by PCR amplification of human VAPB with addition of 5'-BglII and 3'-XhoI restriction sites. The second BglII site at position 7107 in pcDNA3-GFP11(x7)-Actin was removed by site directed mutagenesis using the Quick-Change Lightning kit (Agilent) prior to in frame cloning of human VAPB using T4 DNA ligase (Promega).

Fluorescent Sensors Targeted to Endogenous Proteins (FluoSTEPs) assays of VAPB-localised cAMP and PKA signalling

The FluoSTEP system was used to determine VAPB-localised cAMP and PKA signalling as in [24]. INS1 832/3 cells were transfected with pcDNA3-GFP11(x7)-VAPB and pcDNA3.1(+)-FluoSTEP-ICUE (for cAMP) or pcDNA3.1(+)-FluoSTEP-AKAR (for PKA) at a 1:1 ratio. Cells were seeded onto glass-bottom dishes (MatTek) 24 hours before imaging in RPMI-1640 without phenol red + 10% FBS. Cells were imaged by time-lapse microscopy using a Zeiss LSM-780 inverted confocal laser-scanning microscope with a 63x/1.4 oil immersion objective and a 488 nm excitation wavelength and emissions at 508 and 583 nm for 2 minutes to record a baseline, followed by agonist stimulation at 100 nM for 5 minutes and 2 minutes exposure to 10 µM FSK + 100 µM IBMX to generate a maximal response. FRET emission ratios were calculated and normalised to mean baseline values using GraphPad Prism 10.

Quantification of ERMCSs per mitochondrial area using splitFAST

INS-1 832/3 cells were plated onto Matrigel (Gibco) coated glass-bottom imaging chambers (Ibidi) and transfected with 4xMTS-Halo, ER-RspA-NFAST and OMM-short-RspA-CFAST[50]. After 18 hours, cells were labelled with 10 nM JFX646 Halo ligand (kind gift from the Lavis lab, Janelia) in optiMEM (Gibco) for 3 minutes, followed by 3x washes in mKRB buffer (140 mM NaCl, 2.8 mM KCl, 2 mM $MgCl_2$, 1 mM $CaCl_2$, 10 mM HEPES, 10 mM glucose, pH 7.4) at 37°C. The Lime splitFAST ligand (Twinkle Factory) was prepared at 5 µM in mKRB buffer and passed through a 0.22-µm filter before being added to cells. Exendin-4 was used at 1 µM in Lime splitFAST ligand in mKRB and added to cells for 10 minutes prior to imaging with an LSM980/Airyscan2 point-scanning confocal microscope (Zeiss) in LSMPlus mode. Simultaneous excitation was achieved using solid-state diode lasers at 488 nm/10 mW (0.9% max power) and 639 nm/7.5 mW (1.0% max power), with imaging conditions experimentally selected to minimise crosstalk. The resulting fluorescence was collected using a 63x/1.4 oil immersion objective and detected on a 34-channel spectral GaAsP array detector with the gain set at 650 V and split into two ranges of 490–632 nm and 641–694 nm. Samples were imaged at room temperature in a humidified imaging chamber with a Definite Focus module (Zeiss) employed for thermal drift correction and ZEN Blue v3.2 (Zeiss) software used for acquisition and deconvolution (LSMPlus function). The number of contact sites per mitochondrial area was quantified in Fiji. Firstly, the acquired images were gaussian blurred (sigma radius 1.5) to aid in the generation of reliable downstream masks and puncta detection. An automated Otsu threshold was used to generate mitochondrial masks and quantitate mitochondrial area. These same masks were then applied to the splitFAST channel to ensure that only true contact sites (i.e. puncta on mitochondria) were counted in the analysis. A blinded count of total number of ERMCSs in each cell was taken and normalised to the mitochondrial area.

Statistical analyses for cellular experiments

All statistical analyses and graph generation was performed using GraphPad Prism 10.2.1 (GraphPad Software Inc). Statistical tests used are indicated in the corresponding figure legends. The number of replicates per comparison represents biological replicates and technical replicates within biological replicates are averaged before statistical testing. Data are presented as mean ± SEM. The p value threshold for statistical significance was set at 0.05.

Statistical analyses in human datasets

To compare the effects of *SPHKAP* gene region variants on T2D *versus* BMI, we used GWAS meta-analyses summary statistics from DIAMANTE consortium (http://www.diagram-consortium.org) for T2D by Mahajan *et al*[37], and from GIANT (https://portals.broadinstitute.org/collaboration/giant/index.php/GIANT_consortium_data_files) for BMI by Locke *et al*[40]. We report SNPs from the region surrounding *SPHKAP* gene (Chr2:228,844,666-229,046,361, NCBI human genome built37). Data pre-processing involved merging and aligning variant effects to T2D risk-increasing allele. We extracted beta values for BMI and T2D signals and calculated respective odds ratios (OR) for T2D using the formula OR = exp(beta). The plot contains SNPs with at least nominally significant ($p<0.05$) effects on both BMI and T2D. A scatter plot was generated using RStudio with the ggplot2 package.

Data availability

Proteomics data is deposited in the ProteomeXchange (PRIDE) repository with accession number PXD056782.

Acknowledgements

The authors thank Dr Nicholas Vierra, University of Utah, for the SPHKAP antibodies; Prof Toshihiko Oka, Rikkyo University, for the MIC19-3xHA construct; Prof John D. Scott, Howard Hughes Medical Institute, for the SPHKAP-EGFP construct; Dr Emily Eden, UCL, for the EGFP-VAPB construct; the Filadi lab, CNR Institute of Neuroscience, for the ER-RspA-NFAST and OMM-short-RspA-CFAST splitFAST constructs; and the Avezov lab, UK Dementia Research Institute, for the 4xMTS-Halo construct. We thank the Imperial College Facility for Imaging by Light Microscopy (FILM) for technical support on light microscopy experiments, the Electron Microscopy Centre at the Centre of Structural Biology, Imperial College London, for support during TEM data acquisition, and Dr Ricardo Aramayo at the Electron Microscopy Facility of the MRC Laboratory of Medical Sciences (LMS) for support during cryo-CLEM sample preparation. The room temperature CLEM was supported by the Electron Microscopy and Histology Facility, a Core Facility of the CMCB Technology Platform at TU Dresden. We thank the EM facility of the Max Planck Institute of Molecular Cell Biology and Genetics for their services. We additionally thank the Cambridge Institute for Medical Research (CIMR) Microscopy Facility for their support with acquiring the splitFAST imaging data. The CIMR microscopy LSM980/Airyscan2 was funded by the MRC (MR/Y002172/1). The FILM Facility at Imperial College London is part-supported by funding from the Wellcome Trust (grant 104931/Z/14/Z) and BBSRC (grant BB/L015129/1). The AT lab is funded by grants from Diabetes UK (19/0006094), the MRC (MR/X021467/1), and the Wellcome Trust (301619/Z/23/Z). GA is supported by a President's PhD Scholarship from Imperial College London and AIO by a Commonwealth PhD Scholarship. MS and AM are supported by the German Center for Diabetes Research (DZD e.V.) and the German Ministry for Education and Research (BMBF). The JNA group is funded by a Wellcome Trust Career Development Award (227745/Z/23/Z).

References

1. Rivera Nieves AM, Wauford BM, Fu A. Mitochondrial bioenergetics, metabolism, and beyond in pancreatic β-cells and diabetes. *Frontiers in Molecular Biosciences* **11**, (2024).

2. Haythorne E*, et al.* Diabetes causes marked inhibition of mitochondrial metabolism in pancreatic beta-cells. *Nat Commun* **10**, 2474 (2019).

3. Rivera Nieves AM, Wauford BM, Fu A. Mitochondrial bioenergetics, metabolism, and beyond in pancreatic beta-cells and diabetes. *Front Mol Biosci* **11**, 1354199 (2024).

4. Ahmad E, Lim S, Lamptey R, Webb DR, Davies MJ. Type 2 diabetes. *Lancet* **400**, 1803-1820 (2022).

5. Mayendraraj A, Rosenkilde MM, Gasbjerg LS. GLP-1 and GIP receptor signaling in beta cells - A review of receptor interactions and co-stimulation. *Peptides* **151**, 170749 (2022).

6. Boland ML*, et al.* Resolution of NASH and hepatic fibrosis by the GLP-1R/GcgR dual-agonist Cotadutide via modulating mitochondrial function and lipogenesis. *Nat Metab* **2**, 413-431 (2020).

7. Timper K*, et al.* GLP-1 Receptor Signaling in Astrocytes Regulates Fatty Acid Oxidation, Mitochondrial Integrity, and Function. *Cell Metab* **31**, 1189-1205 e1113 (2020).

8. Wu P*, et al.* Liraglutide Regulates Mitochondrial Quality Control System Through PGC-1alpha in a Mouse Model of Parkinson's Disease. *Neurotox Res* **40**, 286-297 (2022).

9. Carlessi R*, et al.* GLP-1 receptor signalling promotes beta-cell glucose metabolism via mTOR-dependent HIF-1alpha activation. *Sci Rep* **7**, 2661 (2017).

10. Ng MYW, Wai T, Simonsen A. Quality control of the mitochondrion. *Dev Cell* **56**, 881-905 (2021).

11. Dong J*, et al.* Mic19 depletion impairs endoplasmic reticulum-mitochondrial contacts and mitochondrial lipid metabolism and triggers liver disease. *Nat Commun* **15**, 168 (2024).

12. Prinz WA, Toulmay A, Balla T. The functional universe of membrane contact sites. *Nat Rev Mol Cell Biol* **21**, 7-24 (2020).

13. Dudas EF, Huynen MA, Lesk AM, Pastore A. Invisible leashes: The tethering VAPs from infectious diseases to neurodegeneration. *J Biol Chem* **296**, 100421 (2021).

14. Kors S, Costello JL, Schrader M. VAP Proteins - From Organelle Tethers to Pathogenic Host Interactors and Their Role in Neuronal Disease. *Front Cell Dev Biol* **10**, 895856 (2022).

15. Suzuki H*, et al.* ALS-linked P56S-VAPB, an aggregated loss-of-function mutant of VAPB, predisposes motor neurons to ER stress-related death by inducing aggregation of co-expressed wild-type VAPB. *J Neurochem* **108**, 973-985 (2009).

16. Obara CJ*, et al.* Motion of VAPB molecules reveals ER-mitochondria contact site subdomains. *Nature* **626**, 169-176 (2024).

17. Jones B*, et al.* Targeting GLP-1 receptor trafficking to improve agonist efficacy. *Nat Commun* **9**, 1602 (2018).

18. Fang Z*, et al.* Ligand-Specific Factors Influencing GLP-1 Receptor Post-Endocytic Trafficking and Degradation in Pancreatic Beta Cells. *Int J Mol Sci* **21**, (2020).

19. Madsbad S, Holst JJ. Glycaemic control and weight loss with semaglutide in type 2 diabetes. *Lancet Diabetes Endocrinol* **5**, 315-317 (2017).

20. Nauck MA, D'Alessio DA. Tirzepatide, a dual GIP/GLP-1 receptor co-agonist for the treatment of type 2 diabetes with unmatched effectiveness regrading glycaemic control and body weight reduction. *Cardiovasc Diabetol* **21**, 169 (2022).

21. Dutta D, Nagendra L, Anne B, Kumar M, Sharma M, Kamrul-Hasan ABM. Orforglipron, a novel non-peptide oral daily glucagon-like peptide-1 receptor agonist as an anti-obesity medicine: A systematic review and meta-analysis. *Obes Sci Pract* **10**, e743 (2024).

22. Fatima H*, et al.* Evaluating Glycemic Control Efficacy and Safety of the Oral Small Molecule Glucagon-Like Peptide 1 Receptor Agonist Danuglipron in Type 2 Diabetes Patients: A Systemic Review and Meta-Analysis. *Diabetes Metab Syndr Obes* **16**, 3567-3578 (2023).

23. Novikoff A, *et al.* Spatiotemporal GLP-1 and GIP receptor signaling and trafficking/recycling dynamics induced by selected receptor mono- and dual-agonists. *Mol Metab* **49**, 101181 (2021).

24. Zhang JZ, *et al.* Phase Separation of a PKA Regulatory Subunit Controls cAMP Compartmentation and Oncogenic Signaling. *Cell* **182**, 1531-1544 e1515 (2020).

25. Akabane S, Oka T. Insights into the regulation of mitochondrial functions by protein kinase A-mediated phosphorylation. *J Biochem* **175**, 1-7 (2023).

26. Zhang JF, *et al.* An ultrasensitive biosensor for high-resolution kinase activity imaging in awake mice. *Nat Chem Biol* **17**, 39-46 (2021).

27. Vallese F, *et al.* An expanded palette of improved SPLICS reporters detects multiple organelle contacts in vitro and in vivo. *Nat Commun* **11**, 6069 (2020).

28. Kovanich D, van der Heyden MA, Aye TT, van Veen TA, Heck AJ, Scholten A. Sphingosine kinase interacting protein is an A-kinase anchoring protein specific for type I cAMP-dependent protein kinase. *Chembiochem* **11**, 963-971 (2010).

29. Means CK, *et al.* An entirely specific type I A-kinase anchoring protein that can sequester two molecules of protein kinase A at mitochondria. *Proc Natl Acad Sci U S A* **108**, E1227-1235 (2011).

30. Deng Z, *et al.* Selective autophagy of AKAP11 activates cAMP/PKA to fuel mitochondrial metabolism and tumor cell growth. *Proc Natl Acad Sci U S A* **118**, (2021).

31. Neefjes J, Cabukusta B. What the VAP: The Expanded VAP Family of Proteins Interacting With FFAT and FFAT-Related Motifs for Interorganellar Contact. *Contact (Thousand Oaks)* **4**, 25152564211012246 (2021).

32. Di Mattia T, *et al.* FFAT motif phosphorylation controls formation and lipid transfer function of inter-organelle contacts. *EMBO J* **39**, e104369 (2020).

33. Loewen CJ, Roy A, Levine TP. A conserved ER targeting motif in three families of lipid binding proteins and in Opi1p binds VAP. *EMBO J* **22**, 2025-2035 (2003).

34. Vierra NC, *et al.* Neuronal ER-plasma membrane junctions couple excitation to Ca(2+)-activated PKA signaling. *Nat Commun* **14**, 5231 (2023).

35. Wang Y, Harashima SI, Liu Y, Usui R, Inagaki N. Sphingosine kinase 1-interacting protein is a novel regulator of glucose-stimulated insulin secretion. *Sci Rep* **7**, 779 (2017).

36. Liu Y, *et al.* Sphingosine kinase 1-interacting protein is a dual regulator of insulin and incretin secretion. *FASEB J* **33**, 6239-6253 (2019).

37. Mahajan A, *et al.* Multi-ancestry genetic study of type 2 diabetes highlights the power of diverse populations for discovery and translation. *Nat Genet* **54**, 560-572 (2022).

38. Suzuki K, *et al.* Genetic drivers of heterogeneity in type 2 diabetes pathophysiology. *Nature* **627**, 347-357 (2024).

39. Pulit SL, *et al.* Meta-analysis of genome-wide association studies for body fat distribution in 694 649 individuals of European ancestry. *Hum Mol Genet* **28**, 166-174 (2019).

40. Locke AE, *et al.* Genetic studies of body mass index yield new insights for obesity biology. *Nature* **518**, 197-206 (2015).

41. Kaiser SE, Brickner JH, Reilein AR, Fenn TD, Walter P, Brunger AT. Structural basis of FFAT motif-mediated ER targeting. *Structure* **13**, 1035-1045 (2005).

42. Kors S, Schrader M, Costello JL. Multiple Ways to Keep FFAT Under Control! *Contact (Thousand Oaks)* **5**, 1-4 (2022).

43. Friedman JR, Mourier A, Yamada J, McCaffery JM, Nunnari J. MICOS coordinates with respiratory complexes and lipids to establish mitochondrial inner membrane architecture. *Elife* **4**, (2015).

44. Pearson RB, Kemp BE. Protein kinase phosphorylation site sequences and consensus specificity motifs: tabulations. *Methods Enzymol* **200**, 62-81 (1991).

45. Bock-Bierbaum T, *et al.* Structural insights into crista junction formation by the Mic60-Mic19 complex. *Sci Adv* **8**, eabo4946 (2022).

46. Sun N, Malide D, Liu J, Rovira, II, Combs CA, Finkel T. A fluorescence-based imaging method to measure in vitro and in vivo mitophagy using mt-Keima. *Nat Protoc* **12**, 1576-1587 (2017).

47. Yu R, *et al.* The phosphorylation status of Ser-637 in dynamin-related protein 1 (Drp1) does not determine Drp1 recruitment to mitochondria. *J Biol Chem* **294**, 17262-17277 (2019).

48. Kashatus JA, *et al.* Erk2 phosphorylation of Drp1 promotes mitochondrial fission and MAPK-driven tumor growth. *Mol Cell* **57**, 537-551 (2015).

49. von der Malsburg A, *et al.* Structural mechanism of mitochondrial membrane remodelling by human OPA1. *Nature* **620**, 1101-1108 (2023).

50. Garcia Casas P, *et al.* Simultaneous detection of membrane contact dynamics and associated Ca(2+) signals by reversible chemogenetic reporters. *Nat Commun* **15**, 9775 (2024).

51. Ast J, *et al.* Revealing the tissue-level complexity of endogenous glucagon-like peptide-1 receptor expression and signaling. *Nat Commun* **14**, 301 (2023).

52. Ast J, *et al.* Expanded LUXendin Color Palette for GLP1R Detection and Visualization In Vitro and In Vivo. *JACS Au* **2**, 1007-1017 (2022).

53. Ast J, Broichhagen J, Hodson DJ. Reagents and models for detecting endogenous GLP1R and GIPR. *EBioMedicine* **74**, 103739 (2021).

54. Komatsu H, *et al.* Oxygen environment and islet size are the primary limiting factors of isolated pancreatic islet survival. *PLoS One* **12**, e0183780 (2017).

55. Veluthakal R, *et al.* Mitochondrial Dysfunction, Oxidative Stress, and Inter-Organ Miscommunications in T2D Progression. *Int J Mol Sci* **25**, (2024).

56. Rutter GA, Sidarala V, Kaufman BA, Soleimanpour SA. Mitochondrial metabolism and dynamics in pancreatic beta cell glucose sensing. *Biochem J* **480**, 773-789 (2023).

57. Koeck T*, et al.* A common variant in TFB1M is associated with reduced insulin secretion and increased future risk of type 2 diabetes. *Cell Metab* **13**, 80-91 (2011).

58. Reardon W*, et al.* Diabetes mellitus associated with a pathogenic point mutation in mitochondrial DNA. *Lancet* **340**, 1376-1379 (1992).

59. Mulder H. Transcribing beta-cell mitochondria in health and disease. *Mol Metab* **6**, 1040-1051 (2017).

60. Walker EM*, et al.* Retrograde mitochondrial signaling governs the identity and maturity of metabolic tissues. *Science*, eadf2034 (2025).

61. Anton SE*, et al.* Receptor-associated independent cAMP nanodomains mediate spatiotemporal specificity of GPCR signaling. *Cell* **185**, 1130-1142 e1111 (2022).

62. Xie B, Nguyen PM, Idevall-Hagren O. Feedback regulation of insulin secretion by extended synaptotagmin-1. *FASEB J* **33**, 4716-4728 (2019).

63. Xie B, Panagiotou S, Cen J, Gilon P, Bergsten P, Idevall-Hagren O. The endoplasmic reticulum-plasma membrane tethering protein TMEM24 is a regulator of cellular Ca2+ homeostasis. *J Cell Sci* **135**, (2022).

64. Panagiotou S*, et al.* OSBP-mediated PI(4)P-cholesterol exchange at endoplasmic reticulum-secretory granule contact sites controls insulin secretion. *Cell Rep* **43**, 113992 (2024).

65. Hardy JC*, et al.* Molecular determinants and signaling effects of PKA RIalpha phase separation. *Mol Cell* **84**, 1570-1584 e1577 (2024).

66. Chen Z*, et al.* GLP-1R-positive neurons in the lateral septum mediate the anorectic and weight-lowering effects of liraglutide in mice. *J Clin Invest* **134**, (2024).

67. Han J*, et al.* The Identification of Novel Protein-Protein Interactions in Liver that Affect Glucagon Receptor Activity. *PLoS One* **10**, e0129226 (2015).

68. Paradies G, Paradies V, Ruggiero FM, Petrosillo G. Role of Cardiolipin in Mitochondrial Function and Dynamics in Health and Disease: Molecular and Pharmacological Aspects. *Cells* **8**, (2019).

69. Zhang J, Shi Y. In Search of the Holy Grail: Toward a Unified Hypothesis on Mitochondrial Dysfunction in Age-Related Diseases. *Cells* **11**, (2022).

70. Thompson K*, et al.* Biallelic variants in TAMM41 are associated with low muscle cardiolipin levels, leading to neonatal mitochondrial disease. *HGG Adv* **3**, 100097 (2022).

71. Kaufman BA, Li C, Soleimanpour SA. Mitochondrial regulation of beta-cell function: maintaining the momentum for insulin release. *Mol Aspects Med* **42**, 91-104 (2015).

72. Prentki M, Peyot ML, Masiello P, Madiraju SRM. Nutrient-Induced Metabolic Stress, Adaptation, Detoxification, and Toxicity in the Pancreatic beta-Cell. *Diabetes* **69**, 279-290 (2020).

73. Ngo J*, et al.* Mitochondrial morphology controls fatty acid utilization by changing CPT1 sensitivity to malonyl-CoA. *EMBO J* **42**, e111901 (2023).

74. Prentki M, Corkey BE, Madiraju SRM. Lipid-associated metabolic signalling networks in pancreatic beta cell function. *Diabetologia* **63**, 10-20 (2020).

75. Nikonova L, Koza RA, Mendoza T, Chao PM, Curley JP, Kozak LP. Mesoderm-specific transcript is associated with fat mass expansion in response to a positive energy balance. *FASEB J* **22**, 3925-3937 (2008).

76. Wang T*, et al.* OSBPL2 Is Required for the Binding of COPB1 to ATGL and the Regulation of Lipid Droplet Lipolysis. *iScience* **23**, 101252 (2020).

77. Xue J*, et al.* TMEM120A is a coenzyme A-binding membrane protein with structural similarities to ELOVL fatty acid elongase. *Elife* **10**, (2021).

78. Lin J*, et al.* A positive feedback loop between ZEB2 and ACSL4 regulates lipid metabolism to promote breast cancer metastasis. *Elife* **12**, (2023).

79. Gromovsky AD*, et al.* Delta-5 Fatty Acid Desaturase FADS1 Impacts Metabolic Disease by Balancing Proinflammatory and Proresolving Lipid Mediators. *Arterioscler Thromb Vasc Biol* **38**, 218-231 (2018).

80. Obaseki E, Adebayo D, Bandyopadhyay S, Hariri H. Lipid droplets and fatty acid-induced lipotoxicity: in a nutshell. *FEBS Lett* **598**, 1207-1214 (2024).

81. Xu Y*, et al.* CDP-DAG synthase 1 and 2 regulate lipid droplet growth through distinct mechanisms. *J Biol Chem* **294**, 16740-16755 (2019).

82. Yamashita A*, et al.* Glycerophosphate/Acylglycerophosphate acyltransferases. *Biology (Basel)* **3**, 801-830 (2014).

83. Miklas JW*, et al.* TFPa/HADHA is required for fatty acid beta-oxidation and cardiolipin re-modeling in human cardiomyocytes. *Nat Commun* **10**, 4671 (2019).

84. Williams AS*, et al.* Ketone flux through BDH1 supports metabolic remodeling of skeletal and cardiac muscles in response to intermittent time-restricted feeding. *Cell Metab* **36**, 422-437 e428 (2024).

85. Hugenroth M, Bohnert M. Come a little bit closer! Lipid droplet-ER contact sites are getting crowded. *Biochim Biophys Acta Mol Cell Res* **1867**, 118603 (2020).

86. Briant LJB*, et al.* CPT1a-Dependent Long-Chain Fatty Acid Oxidation Contributes to Maintaining Glucagon Secretion from Pancreatic Islets. *Cell Rep* **23**, 3300-3311 (2018).

87. Shiiba I*, et al.* ER-mitochondria contacts mediate lipid radical transfer via RMDN3/PTPIP51 phosphorylation to reduce mitochondrial oxidative stress. *Nat Commun* **16**, 1508 (2025).

88. Sassano ML, Felipe-Abrio B, Agostinis P. ER-mitochondria contact sites; a multifaceted factory for Ca(2+) signaling and lipid transport. *Front Cell Dev Biol* **10**, 988014 (2022).

89. Raffaello A, Mammucari C, Gherardi G, Rizzuto R. Calcium at the Center of Cell Signaling: Interplay between Endoplasmic Reticulum, Mitochondria, and Lysosomes. *Trends Biochem Sci* **41**, 1035-1049 (2016).

90. Klec C, Ziomek G, Pichler M, Malli R, Graier WF. Calcium Signaling in ss-cell Physiology and Pathology: A Revisit. *Int J Mol Sci* **20**, (2019).

91. Naylor J*, et al.* Use of CRISPR/Cas9-engineered INS-1 pancreatic beta cells to define the pharmacology of dual GIPR/GLP-1R agonists. *Biochem J* **473**, 2881-2891 (2016).

92. Yu V*, et al.* Differential CpG methylation at Nnat in the early establishment of beta cell heterogeneity. *Diabetologia*, (2024).

93. Tyanova S, Temu T, Cox J. The MaxQuant computational platform for mass spectrometry-based shotgun proteomics. *Nat Protoc* **11**, 2301-2319 (2016).

94. Shah AD, Goode RJA, Huang C, Powell DR, Schittenhelm RB. LFQ-Analyst: An Easy-To-Use Interactive Web Platform To Analyze and Visualize Label-Free Proteomics Data Preprocessed with MaxQuant. *J Proteome Res* **19**, 204-211 (2020).

95. Akabane S*, et al.* PKA Regulates PINK1 Stability and Parkin Recruitment to Damaged Mitochondria through Phosphorylation of MIC60. *Mol Cell* **62**, 371-384 (2016).

96. Lam J*, et al.* A Universal Approach to Analyzing Transmission Electron Microscopy with ImageJ. *Cells* **10**, (2021).

97. Manchanda Y*, et al.* Enhanced Endosomal Signaling and Desensitization of GLP-1R vs GIPR in Pancreatic Beta Cells. *Endocrinology* **164**, (2023).

98. Landoni JC, Kleele T, Winter J, Stepp W, Manley S. Mitochondrial Structure, Dynamics, and Physiology: Light Microscopy to Disentangle the Network. *Annu Rev Cell Dev Biol* **40**, 219-240 (2024).

99. Perry SW, Norman JP, Barbieri J, Brown EB, Gelbard HA. Mitochondrial membrane potential probes and the proton gradient: a practical usage guide. *Biotechniques* **50**, 98-115 (2011).

100. Lobas MA*, et al.* A genetically encoded single-wavelength sensor for imaging cytosolic and cell surface ATP. *Nat Commun* **10**, 711 (2019).

101. Polishchuk RS*, et al.* Correlative light-electron microscopy reveals the tubular-saccular ultrastructure of carriers operating between Golgi apparatus and plasma membrane. *J Cell Biol* **148**, 45-58 (2000).

102. Seligman AM, Wasserkrug HL, Hanker JS. A new staining method (OTO) for enhancing contrast of lipid--containing membranes and droplets in osmium tetroxide--fixed tissue with osmiophilic thiocarbohydrazide(TCH). *J Cell Biol* **30**, 424-432 (1966).

103. Kremer JR, Mastronarde DN, McIntosh JR. Computer visualization of three-dimensional image data using IMOD. *J Struct Biol* **116**, 71-76 (1996).

104. Paul-Gilloteaux P*, et al.* eC-CLEM: flexible multidimensional registration software for correlative microscopies. *Nat Methods* **14**, 102-103 (2017).

105. de Chaumont F*, et al.* Icy: an open bioimage informatics platform for extended reproducible research. *Nat Methods* **9**, 690-696 (2012).

106. Belevich I, Joensuu M, Kumar D, Vihinen H, Jokitalo E. Microscopy Image Browser: A Platform for Segmentation and Analysis of Multidimensional Datasets. *PLoS Biol* **14**, e1002340 (2016).

107. Fehrenbach J, Weiss P, Lorenzo C. Variational algorithms to remove stationary noise: applications to microscopy imaging. *IEEE Trans Image Process* **21**, 4420-4430 (2012).

108. Hirabayashi Y*, et al.* ER-mitochondria tethering by PDZD8 regulates Ca(2+) dynamics in mammalian neurons. *Science* **358**, 623-630 (2017).

109. Sambrook J, Russell DW. Purification of nucleic acids by extraction with phenol:chloroform. *CSH Protoc* **2006**, (2006).

110. Rooney JP*, et al.* PCR based determination of mitochondrial DNA copy number in multiple species. *Methods Mol Biol* **1241**, 23-38 (2015).

111. Neelankal John A, Ram R, Jiang FX. RNA-Seq Analysis of Islets to Characterise the Dedifferentiation in Type 2 Diabetes Model Mice db/db. *Endocr Pathol* **29**, 207-221 (2018).

Figure Legends

Fig. 1. hGLP-1R β-cell interactome and validation of VAPB-hGLP-1R interaction. a, Heatmap of GLP-1R interactor enrichment from anti-FLAG co-immunoprecipitates of vehicle (Veh) *versus* 5-minute exendin-4 (Ex-4)-stimulated INS-1 832/3 SNAP/FLAG-hGLP-1R cells; blue, decreased; red, increased binding; LC-MS/MS data analysed in LFQ-Analyst and normalised to hGLP-1R levels for each experimental sample; colour scale centred around overall median value of the experiment; *n*=4. **b**, Volcano plot of data from (**a**) depicting $\log_2$ fold change to vehicle (x-axis) *versus* -$\log10_q$value (y-axis). **c**, ER, mitochondria or ERMCS-localised hGLP-1R interactors enriched in exendin-4-stimulated *versus* vehicle conditions. **d**, Co-immunoprecipitation (co-IP) of EGFP-VAPB with SNAP/FLAG-hGLP-1R in Veh *versus* 5-minute Ex-4-stimulated INS-1 832/3 SNAP/FLAG-hGLP-1R cells. Representative blots and quantification of EGFP-VAPB levels per condition normalised to SNAP shown; *n*=3, *p<0.05 by paired t-test. **e**, As for (**d**) for endogenous VAPB; *n*=4, *p<0.05 by paired t-test. **f**, Confocal microscopy analysis of SNAP/FLAG-hGLP-1R (red) co-localisation with EGFP-VAPB (green) in Ex-4-stimulated INS-1 832/3 SNAP/FLAG-hGLP-1R cells; box, magnification inset; size bar, 5 µm. **g**, Electron microscopy micrograph depicting gold-labelled SNAP/FLAG-hGLP-1R (arrows) localised to an endosome–ER MCS in an Ex-4-stimulated INS-1 832/3 SNAP/FLAG-hGLP-1R cell; endosome highlighted in gold and ER in blue; size bar, 100 nm. **h**, Maximum intensity projection (MIP) of a confocal z-stack of EGFP-VAPB (green) and SNAP/FLAG-hGLP-1R (red) from an Ex-4-stimulated INS-1 832/3 SNAP/FLAG-hGLP-1R cell; size bar, 10 µm. **i**, Ex-4-induced insulin secretion (fold over 11 mM glucose) in non-targeting Control *versus* VAPB RNAi-treated INS-1 832/3 cells; *n*=4, *p<0.05 by paired t-test.

Fig. 2. Internalisation-dependent hGLP-1R-VAPB binding and VAPB-localised GLP-1R signalling. a, EGFP-VAPB co-IP with SNAP/FLAG-hGLP-1R in vehicle (Veh) *versus* exendin-4 (Ex-4)-stimulated INS-1 832/3 SNAP/FLAG-hGLP-1R cells co-expressing control pcDNA3.1+ *versus* dominant negative dynamin (Dyn) 1 + 2 K44A. **b**, Veh-subtracted Ex-4-*versus* exendin-F1 (Ex-F1)-induced BRET kinetic traces (left) and corresponding AUCs (right) of SNAP/FLAG-hGLP-1R-NLuc–Venus-VAPB interactions in INS-1 832/3 cells; *n*=3, *p<0.05 by paired t-test. **c** (top), Confocal microscopy analysis of SNAP/FLAG-hGLP-1R localisation in mouse primary islets transduced with SNAP/FLAG-hGLP-1R adenoviruses following 5-minute stimulation with the indicated agonists [Ex-4, Ex-F1, exendin-D3 (Ex-D3), tirzepatide (Tirz) and semaglutide (Sema) used at 100 nM; orforglipron (Orf) and danuglipron (Dan) used at 5 μM]; size bars, 20 μm; **c** (bottom), Quantification of residual surface SNAP/FLAG-hGLP-1R levels in islets from above; *n*=3. **d**, Quantification of EGFP-VAPB co-IP with SNAP/FLAG-hGLP-1R in INS-1 832/3 SNAP/FLAG-hGLP-1R cells stimulated for 5 minutes with the indicated agonists; *n*=3. **e**, VAPB-localised cAMP generation (measured by FluoSTEP) in response to stimulation with 100 nM Ex-4 *versus* Ex-F1 in INS-1 832/3 cells expressing pcDNA3-GFP11(x7)-VAPB + pcDNA3.1(+)-FluoSTEP-ICUE; maximal responses (to FSK+IBMX) shown; kinetic traces (left) and corresponding AUCs for the agonist-stimulated period (right) shown; *n*=5, *p<0.05 by paired t-test. **f** (top), Ex-4 *versus* Ex-F1-induced global PKA activity, measured with the global PKA biosensor pcDNA3.1(+)- ExRai-AKAR2 in INS-1 832/3 cells; kinetic traces (left) and corresponding AUCs (right) shown; *n*=3; ns, non-significant by paired t-test. **f** (bottom), Ex-4 *versus* Ex-F1-induced mitochondrial PKA activity, measured with the mitochondrial PKA biosensor pcDNA3-mitoExRai-AKAR2 in INS-1 832/3 cells; kinetic traces (left) and corresponding AUCs (right) shown; *n*=3, **p<0.01 by paired t-test. **g**, Mitochondrial over global PKA activity, calculated as AUC ratio from data in (**f**); *n*=3, *p<0.05 by paired t-test.

Fig. 3. hGLP-1R localisation to ERMCSs. a, SNAP/FLAP-hGLP-1R associated with purified mitochondria in mitochondrial fractions from vehicle (Veh) *versus* exendin-4 (Ex-4)-stimulated INS-1 832/3 SNAP/FLAG-hGLP-1R cells. Representative blots (left) and quantification of SNAP/FLAP-hGLP-1R over Tom20 signals (right) shown; *n*=3, *p<0.05 by paired t-test. **b**, Confocal microscopy analysis of SNAP/FLAG-hGLP-1R (red) co-localisation with ERMCSs (SPLICS Mt-ER Long P2A, green) in Ex-4-stimulated INS-1 832/3 SNAP/FLAG-hGLP-1R cells; box, magnification inset; size bar, 5 μm. **c**, Time-lapse confocal microscopy analysis of SNAP/FLAG-hGLP-1R–ERMCS association, imaged as in (**b**); arrows indicate co-localised spots; time post-Ex-4 addition indicated; size bar, 10 μm. **d**, Single confocal slice from an Ex-4-stimulated INS-1 832/3 SNAP/FLAG-hGLP-1R cell, with signals for EFGP-VAPB (green), SNAP/FLAG-hGLP-1R (yellow), mitochondria (magenta), and DAPI (blue) shown; arrow points to a SNAP/FLAG-hGLP-1R-positive endosome used for CLEM analysis; size bar, 10 μm. **e**, CLEM overlay of aligned confocal slice with corresponding single slice of an EM tomogram; size bar, 10 μm; magnification of EM tomogram slices with the SNAP/FLAG-hGLP-1R-positive endosome from (**d**) (arrow) shown; size bar, 1 μm. **f**, 3D rendering of the segmentation of data from (**e**), with ER (purple), mitochondria (orange) and SNAP/FLAG-hGLP-1R-positive endosome (yellow) shown. **g**, TEM micrograph of a 70-nm ultrathin section from resin embedded mouse islets transduced with a SNAP/FLAG-hGLP-1R adenovirus, with SNAP/FLAG-hGLP-1R labelled with SNAP-Surface biotin + Alexa Fluor 488 Streptavidin, 5-nm colloidal gold prior to Ex-4 stimulation and fixation; ER (blue), mitochondria (yellow) and SNAP/FLAG-hGLP-1R-positive endosome (pink); inset shows magnified endosome area containing 5-nm gold particles; size bars, 100 nm.

Fig. 4. hGLP-1R–SPHKAP association via shared VAPB binding and SPHKAP-dependent GLP-1R-induced VAPB-localised PKA activity. a, SPHKAP-EGFP co-IP with SNAP/FLAG-hGLP-1R in Control *versus* VAPB RNAi-treated INS-1 832/3 SNAP/FLAG-hGLP-1R cells under vehicle (Veh) *versus* exendin-4 (Ex-4)-stimulated conditions. **b**,

Quantification of SPHKAP-EGFP over SNAP/FLAG-hGLP-1R levels from (**a**); *n*=4, *p<0.05, ns, non-significant by one-way ANOVA with Šidák post-hoc test; Veh fold changes also shown, *p<0.05 by paired t-test. **c**, Confocal microscopy analysis of SPHKAP-EGFP *versus* mitochondria (imaged with MitoTracker Red) localisation in INS-1 832/3 cells treated with Control *versus* VAPB RNAi; size bars, 5 µm. **d**, Confocal microscopy analysis of SPHKAP-EGFP *versus* ER (imaged with ER-Tracker Red) localisation in INS-1 832/3 cells; size bar, 10 µm. **e**, Ex-4-stimulated cAMP responses in Control *versus* SPHKAP RNAi-treated INS-1 832/3 cells, measured with cADDis cAMP biosensor; top, cAMP traces; bottom, AUC quantification; *n*=3; ns, non-significant by paired t-test. **f**, Ex-4-stimulated global PKA responses in Control *versus* SPHKAP RNAi-treated INS-1 832/3 cells; left, PKA traces; right, AUC quantification; *n*=4; ns, non-significant by paired t-test. **g**, Ex-4-stimulated mitochondrial PKA responses in Control *versus* SPHKAP RNAi-treated INS-1 832/3 cells; left, PKA traces; right, AUC quantification; *n*=4, *p<0.05 by paired t-test. **h**, VAPB-localised PKA activity (measured by FluoSTEP) in response to 100 nM Ex-4 stimulation in Control *versus* SPHKAP RNAi-treated INS-1 832/3 cells expressing pcDNA3-GFP11(x7)-VAPB + pcDNA3.1(+)-FluoSTEP-AKAR; maximal responses (to FSK+IBMX) shown; kinetic traces (left) and corresponding AUCs for the agonist-stimulated period (right) shown; *n*=5, *p<0.05 by paired t-test.

Fig. 5. Regulation of GLP-1R function by SPHKAP. **a**, Exendin-4 (Ex-4)-stimulated changes in mitochondrial membrane potential in Control *versus* SPHKAP RNAi-treated INS-1 832/3 cells, measured with TMRE; left, membrane potential traces; G20, 20 mM glucose; right, quantification of AUCs during the Ex-4 and G20 periods; *n*=5, *p<0.05 by paired t-test. **b**, Ex-4-stimulated ATP responses in Control *versus* SPHKAP RNAi-treated INS-1 832/3 cells, measured with the cyto-Ruby3-iATPSnFR1.0 biosensor; left, ATP traces; right, AUC quantification; *n*=3, *p<0.05 by paired t-test. **c**, Ex-4-induced insulin secretion (fold over 11 mM glucose) in Control *versus* SPHKAP RNAi-treated INS-1 832/3 cells; *n*=3, *p<0.05 by paired t-test. **d**, Percentage of apoptosis +/- thapsigargin exposure in Control *versus* SPHKAP RNAi-treated INS-1 832/3 cells under vehicle (Veh) *versus* Ex-4-stimulated conditions; *n*=3; *p<0.05 by one-way ANOVA with Šidák post-hoc test. **e**, PKA-dependent phosphorylation of MIC19-3xHA in INS-1 832/3 cells under Veh *versus* Ex-4-stimulated conditions, determined by Western blotting of anti-HA immunoprecipitates with an anti-RRx-pS/T antibody; forskolin (FSK), positive control for PKA activation; left, representative blots; right, quantification of phospho-MIC19 levels; *n*=3, *p<0.05 by one-way ANOVA with Šidák post-hoc test. **f**, Ex-4-induced mitophagy, measured as changes in ratio fluorescence intensities (580/440 nm) over time with the dual-excitation ratiometric biosensor mKeima-Red-Mito-7 in Control *versus* SPHKAP RNAi-treated INS-1 832/3 cells; *n*=6. **g**, Time-lapse confocal microscopy imaging showing Drp1 localisation to mitochondria in Veh *versus* Ex-4-stimulated INS-1 832/3 cells; mitochondria (mito-BFP, blue) and Drp1 (mCherry-Drp1, red); arrows indicate Drp1-positive spots on mitochondria; time post-Veh or Ex-4 exposure indicated; size bars, 10 µm. **h**, Changes in Drp1 phosphorylation at Ser 616 in Control *versus* SPHKAP RNAi-treated Ex-4-stimulated INS-1 832/3 cells; left, representative blots; right, quantification; *n*=4; *p<0.05 by two-way ANOVA with Tukey post-hoc test.

Fig. 6. GLP-1R/SPHKAP-dependent mitochondrial remodelling. **a**, Confocal microscopy analysis of mitochondrial morphology in vehicle (Veh) *versus* exendin-4 (Ex-4)-stimulated WT INS-1 832/3 cells; top, representative images with mitochondria labelled with MitoTracker Red; size bar, 10 µm; bottom, percentage of cells classified as presenting hyperfused, tubular or fragmented mitochondria per condition; *n*=4, ***p<0.001 by two-way ANOVA with Tukey post-hoc test. **b**, as in (**a**) for INS-1 832/3 GLP-1R KO cells; *n*=4; ns, non-significant by two-way ANOVA with Tukey post-hoc test. **c**, as in (**a**) for Control *versus* SPHKAP RNAi-treated INS-1 832/3 cells under Veh *versus* Ex-4-stimulated conditions; *n*=5, **p<0.01, ***p<0.001, ns, non-significant by two-way ANOVA with Tukey post-hoc test. **d**, Maximum intensity projections (MIP) from confocal z-stacks of mitochondria in vehicle (Veh) *versus* Ex-4-stimulated Control and SPHKAP RNAi-treated INS-1 832/3 cells; size bars, 10

µm. **e**, Representative images of mitochondrial morphology in Control *versus* SPHKAP RNAi-treated INS-1 832/3 cells under Veh *versus* Ex-4-stimulated conditions, imaged by super-resolved STED microscopy; size bars, 2 µm.

Fig. 7. Exendin-4-induced changes in mitochondrial morphology and number of ERMCSs per mitochondria. a, Representative TEM micrographs of resin-embedded ultrathin sections depicting mitochondrial morphology in Control *versus* SPHKAP RNAi-treated INS-1 832/3 cells, and in INS-1 832/3 GLP-1R KO cells, under vehicle (Veh) *versus* exendin-4 (Ex-4)-stimulated conditions; size bars, 100 nm. **b**, Quantification of mitochondrial area and number of cristae per mitochondria from ~200 TEM images collected from n=3 independent experiments, ****p<0.0001; ns, non-significant by one-way ANOVA with Šidák post-hoc test. **c**, Quantification of ERMCS length in Control *versus* SPHKAP RNAi TEM images from (**a**,**b**); *p<0.05 by one-way ANOVA with Šidák post-hoc test. **d**, Representative confocal images of WT INS-1 832/3 cells co-expressing the mitochondrial marker 4xMTS-Halo (green) and splitFAST reporters ER-RspA-NFAST and OMM-short-RspA-CFAST, labelled with a Lime splitFAST ligand to detect ERMCSs (magenta) under Veh *versus* Ex-4-stimulated conditions; size bars, 5 µm. **e**, Quantification of the number of ERMCSs per mitochondrial area from data in (**d**); results per cell (left) and per independent experiment (right) shown; 50-57 cells imaged in n=3 independent experiments, *p<0.05, ****p<0.0001 by unpaired t-test.

Fig. 8. SPHKAP control of GLP-1R function in primary mouse islets. a, PLAs showing interactions between endogenous GLP-1R and VAPB (left) or SPHKAP (right) in exendin-4 (Ex-4)-stimulated primary mouse islets; size bars, 20 µm. **b**, Ex-4-induced changes in ATP level (normalised to total protein) in Control *versus* SPHKAP shRNA-transduced primary mouse islets; n=5, *p<0.05 by one-way ANOVA with Šidák post-hoc test. **c**, Ex-4-induced changes in thapsigargin-triggered ROS accumulation in Control *versus* SPHKAP shRNA-transduced primary mouse islets; n=6, *p<0.05 by one-way ANOVA with Šidák post-hoc test. **d**, Ex-4-induced potentiation of insulin secretion in Control *versus* SPHKAP shRNA-transduced primary mouse islets; n=9, *p<0.05 by one-way ANOVA with Šidák post-hoc test; fold over 11 mM glucose (G11) also shown, p=0.0869 by paired ratio t-test.

Fig. 9. SPHKAP control of GLP-1R-dependent mitochondrial remodelling in primary mouse islets. a, Confocal microscopy analysis of mitochondrial morphology in vehicle (Veh) *versus* exendin-4 (Ex-4)-stimulated WT primary mouse islets; top, representative images with MitoTracker Red-labelled mitochondria; size bar, 20 µm; bottom, percentage of islet cells classified as presenting hyperfused, tubular or fragmented mitochondria per condition; n=5 islet preps from separate mice, *p<0.05 by two-way ANOVA with Tukey post-hoc test. **b**, as in (**a**) for islets from GLP-1R KO mice; n=5 islet preps from separate mice; ns, non-significant by two-way ANOVA with Tukey post-hoc test. **c**, as in (**a**) for Control *versus* SPHKAP shRNA-transduced mouse islets under Veh *versus* Ex-4-stimulated conditions; n=6 islet preps from separate mice, *p<0.05, **p<0.01, ns, non-significant by two-way ANOVA with Tukey post-hoc test. **d**, as in (**a**) for Control *versus* SPHKAP RNAi-treated dispersed primary mouse islet cells under Veh *versus* Ex-4-stimulated conditions; size bars, 5 µm; n=4 islet preps from separate mice, ***p<0.001, ns, non-significant by two-way ANOVA with Tukey post-hoc test.

Fig. 10. GLP-1R–VAPB/SPHKAP interactions and GLP-1R-dependent mitochondrial remodelling in primary human islets. a, PLA showing interactions between endogenous GLP-1R and VAPB (left) or SPHKAP (right) in exendin-4 (Ex-4)-stimulated primary human islets; size bars, 20 µm. **b**, Negative control (no primary antibody) for PLA data shown in (**a**); nuclei (DAPI), blue; size bar, 20 µm. **c**, Confocal microscopy analysis of mitochondrial morphology in vehicle (Veh) *versus* Ex-4-stimulated primary human islets; representative images with mitochondria labelled with MitoTracker Red; size bars, 20 µm; inset, magnification areas. **d**, Percentage of human islet cells classified as presenting hyperfused,

tubular or fragmented mitochondria per condition; *n*=5 islet preps from separate human donors, *p<0.05, ns, non-significant by two-way ANOVA with Tukey post-hoc test.

Supplementary Figure Legends

Supplementary Fig. 1. hGLP-1R β-cell interactome and validation of VAPB-hGLP-1R interaction – Extra data. a, Principal component analysis (PCA) of biological repeats from interactome data from Fig. 1a,b. **b**, Pathway enrichment analysis using gProfiler; results show 10 most significant gene ontology terms represented in the interactome data from Fig.1a,b. **c**, SNAP/FLAG-hGLP-1R levels in input *versus* output supernatants from co-IP experiments from Fig. 1e. **d**, Time-series confocal microscopy analysis of SNAP/FLAG-hGLP-1R (red) and EGFP-VAPB (green) localisation in response to exendin-4 (Ex-4) in INS-1 832/3 SNAP/FLAG-GLP-1R cells; time post-Ex-4 addition indicated; size bar, 5 µm. **e**, EGFP-VAPB WT *versus* P56S mutant co-IP with SNAP/FLAG-hGLP-1R in vehicle (Veh) *versus* Ex-4-stimulated INS-1 832/3 SNAP/FLAG-hGLP-1R cells. **f,** Confocal microscopy analysis of SNAP/FLAG-hGLP-1R (red) co-localisation with EGFP-VAPB WT or P56S (green) in Ex-4-stimulated INS-1 832/3 SNAP/FLAG-hGLP-1R cells; size bars, 5 µm. **g**, Western blot analysis of endogenous VAPB levels in Control *versus* VAPB RNAi-treated INS-1 832/3 cells; representative blots and quantification of VAPB knockdown shown; *n*=3, **p<0.01 by paired t-test. **h**, Ex-4-induced potentiation of insulin secretion in Control *versus* VAPB RNAi-treated INS-1 832/3 cells; *n*=4, **p<0.01, ns, non-significant by one-way ANOVA with Šidák post-hoc test. **i**, Ex-4-induced insulin secretion in pcDNA3.1+, EGFP-VAPB WT and P56S-transfected INS-1 832/3 cells; fold over pcDNA3.1+ also shown, *n*=5; **p<0.01 by one-way ANOVA with Šidák post-hoc test; *p<0.05 by paired t-test.

Supplementary Fig. 2. Internalisation-dependent hGLP-1R-VAPB binding and VAPB-localised GLP-1R signalling – Extra data. a, Confocal microscopy analysis of SNAP/FLAG-hGLP-1R localisation in exendin-4 (Ex-4)-stimulated INS-1 832/3 SNAP/FLAG-hGLP-1R cells co-expressing dominant negative dynamin (Dyn) 1 + 2 K44A; white arrow indicates plasma membrane SNAP/FLAG-hGLP-1R localisation with Dyn1+2 K44A co-expression; yellow arrow indicates endosomal SNAP/FLAG-hGLP-1R localisation in a non-Dyn1+2 K44A expressing cell; size bar, 5 µm. **b**, Schematic of the hGLP-1R-Nanoluciferase (NLuc)–Venus-VAPB interaction NanoBRET assay. **c**, Representative blots from EGFP-VAPB co-IP with SNAP/FLAG-hGLP-1R in INS-1 832/3 SNAP/FLAG-hGLP-1R cells stimulated for 5 minutes with: Ex-4, exendin-F1 (Ex-F1), exendin-D3 (Ex-D3), tirzepatide (Tirz), semaglutide (Sema) all used at 100 nM; orforglipron (Orf) and danuglipron (Dan) used at 5 µM. **d**, Schematic of the FluoSTEP method used to quantify GLP-1R-induced VAPB-localised cAMP generation; Epac1 (149-881), exchange protein activated by cAMP, amino acids 149-881; RFP, red fluorescent protein; $sfGFP_{1-10}$, superfolder green fluorescent protein helices 1-10; GFP_{11}, 11th helix of sfGFP; VAPB, vesicle-associated membrane protein-associated protein B. **e**, Localisation of the excitation-ratiometric global PKA biosensor pcDNA3.1(+)-ExRai-AKAR2 and mitochondrial PKA biosensor pcDNA3-mitoExRai-AKAR2 in INS-1 832/3 cells; size bars,10 µm. **f**, Ex-4-stimulated global and mitochondrial PKA responses in INS-1 832/3 cells, measured with the biosensors from (**e**); Forskolin (FSK) + IBMX added to record maximal responses.

Supplementary Fig. 3. hGLP-1R β-cell interactome analysis with further agonists. Heatmap of GLP-1R interactor enrichment analysis from anti-FLAG co-immunoprecipitates from INS-1 832/3 SNAP/FLAG-hGLP-1R cells stimulated for 5 minutes with the indicated agonists; blue, decreased; red, increased enrichment; LC-MS/MS data analysed in LFQ-Analyst and normalised to hGLP-1R levels for each experimental sample; colour scale centred around overall median value; *n*=4 for exendin-4 (Ex-4), exendin-F1 (Ex-F1) and exendin-D3 (Ex-D3); *n*=3 for GLP-1.

Supplementary Fig. 4. hGLP-1R localisation to ERMCSs – Extra data. a, Single cryo-confocal slice from an exendin-4 (Ex-4)-stimulated INS-1 832/3 SNAP/FLAG-hGLP-1R cell, with signals for EGFP-VAPB (cyan), SNAP/FLAG-hGLP-1R (magenta), and mitochondria (yellow); inset, magnified area; arrow points to SNAP/FLAG-hGLP-1R-positive endosome used for cryo-CLEM analysis; size bar, 5 µm. **b**, Overlay of a cryo-confocal slice aligned with the corresponding single slice of a resliced 3D cryoFIB/SEM volume. **c**, 3D rendering of the segmentation of the FIB-SEM volume data from (**b**), with ER (cyan), mitochondria (yellow) and SNAP/FLAG-hGLP-1R-positive endosome (magenta) shown.

Supplementary Fig. 5. Gene expression data and genetic association of *SPHKAP* variants with T2D and BMI. a, Schematic of the AKAP SPHKAP protein primary structure. AKB, A-kinase binding domain; pFFAT, phospho-FFAT motif. Alignment of SPHKAP FFAT motif to the canonical FFAT sequence depicted; Alcoholic residues are highlighted in blue, acidic residues in green, and aromatic residues in red; all other residues are in black. **b**, Analysis of *SPHKAP* mRNA levels from primary islets isolated from WT *versus* heterozygous and homozygous *db*/*db* mice; data obtained from RNA Seq dataset GSE107489[111]; n=3, **p<0.01 by one-way ANOVA with Dunnett post-hoc test. **c**, *SPHKAP* gene region variant associations from T2D European ancestry[37] and multi-ancestry[38] GWAS; y-axes represent significance ($-\log_{10}$ p-value) of phenotype–variant associations and x-axes genomic location of the variants (NCBI human genome build37). Secondary y-axes represent recombination fraction from 1000 Genomes Project and horizontal dashed lines highlight association threshold for significance ($p=5\times10^{-8}$). Lead variant with the highest significance is shown as a purple diamond and correlation (LD, r^2) of other SNPs in the lead variant region represented with colours as per box legend. Variants previously reported for associations with phenotypes in GWAS catalog (www.ebi.gwas.org) are indicated and respective phenotypes listed. **d**, As for (**c**) for BMI GWAS meta-analyses[39, 40]. **e**, Comparison of the effects of *SPHKAP* gene region variants showing at least nominal association (p<0.05) with both T2D risk and high adiposity (BMI) from GWAS meta-analyses from (**c**,**d**). X-axis [odds ratio (OR) with 95% confidence interval] corresponds to associations with T2D, while y-axis (beta with standard error) corresponds to associations with BMI. Variant points are scaled in size to their significance with T2D (z-score from association test). Seven *SPHKAP* single nucleotide polymorphisms (SNPs), 2 for T2D and 5 for high BMI, identified for T2D / BMI from GWAS Catalog (www.ebi.gwas.org) as being in high linkage disequilibrium (LD) with each other, are indicated. **f**, *SPHKAP* coding variant effects on random glucose (RG) from UKBB whole-exome sequencing (WES) data for ~450,000 individuals; y-axis represents significance ($-\log_{10}$ p-value) of variant association and x-axis represents the genomic location of variants (NCBI human genome build37). Secondary y-axis represents recombination fraction from 1000 Genomes Project and horizontal dashed line highlights the association threshold for significance ($p=5\times10^{-8}$). RG levels in mmol/L are natural logarithm transformed and adjusted for time since last meal (t) as $t+t^2+t^3$, age, sex, and six principal components (derived from UKBB GWAS data).

Supplementary Fig. 6. hGLP-1R–SPHKAP association via shared VAPB binding – Extra data. a, SNAP/FLAG-hGLP-1R levels in input *versus* output supernatants from co-IP experiments from Fig. 4a,b. **b**, Endogenous SPHKAP co-IP with SNAP/FLAG-hGLP-1R in vehicle (Veh) *versus* exendin-4 (Ex-4)-stimulated INS-1 832/3 SNAP/FLAG-hGLP-1R cells. **c**, z-stack series of confocal microscopy images of SPHKAP-EGFP and mitochondria (imaged with MitoTracker Red) in INS-1 832/3 cells; size bar, 10 µm. **d**, SPHKAP-EGFP pFFAT motif mutant (DFLTESE) co-IP with SNAP/FLAG-hGLP-1R in Veh *versus* Ex-4-stimulated INS-1 832/3 SNAP/FLAG-hGLP-1R cells. **e**, Confocal microscopy analysis of SPHKAP-EGFP WT *versus* pFFAT motif mutant with mitochondria (labelled with MitoTracker Red) in INS-1 832/3 cells; size bars, 5 µm. **f**, Western blot analysis of endogenous SPHKAP levels in Control *versus* SPHKAP RNAi-treated INS-1 832/3 cells. **g**, Quantification of SPHKAP knockdown from (**f**); n=3, *p<0.05 by paired t-test. **h**, Western blot analysis of SPHKAP-EGFP levels in Control *versus* SPHKAP RNAi-treated INS-1 832/3 cells.

Supplementary Fig. 7. Regulation of GLP-1R function by SPHKAP – Extra data. a, EGFP-VAPB co-IP with SNAP/FLAG-hGLP-1R in Control *versus* SPHKAP RNAi-treated INS-1 832/3 SNAP/FLAG-hGLP-1R cells under vehicle (Veh) *versus* exendin-4 (Ex-4)-stimulated conditions. **b**, Confocal microscopy analysis of EGFP-VAPB co-localisation with SNAP/FLAG-hGLP-1R in Ex-4-stimulated Control *versus* SPHKAP RNAi-treated INS-1 832/3 SNAP/FLAG-hGLP-1R cells; size bars, 5 µm. **c**, Schematic of the FluoSTEP method used to quantify GLP-1R-induced VAPB-localised PKA activity; FHA1, forkhead-associated 1 phospho-peptide binding protein; PKA, protein kinase A; RFP, red fluorescent protein; $sfGFP_{1-10}$, superfolder green fluorescent protein helices 1-10; GFP_{11}, 11th helix of sfGFP; VAPB, vesicle-associated membrane protein-associated protein B. **d**, Ex-4-induced changes in ATP level in Control *versus* SPHKAP RNAi-treated INS-1 832/3 cells; n=3, *p<0.05 by one-way ANOVA with Šidák post-hoc test. **e**, Ex-4-induced potentiation of insulin secretion in Control *versus* SPHKAP RNAi-treated INS-1 832/3 cells; n=3, *p<0.05 by one-way ANOVA with Šidák post-hoc test. **f**, Ex-4-induced potentiation of insulin secretion in INS-1 832/3 cells transfected with EGFP *versus* SPHKAP-EGFP; n=3; ns, non-significant by one-way ANOVA with Šidák post-hoc test; fold over 11 mM glucose (G11) also shown; ns, non-significant by paired t-test. **g**, Ex-4 induced changes in ER Ca^{2+}, measured with pCAG G-CEPIA1er, in Control *versus* SPHKAP RNAi-treated INS-1 832/3 cells; n=4. **h**, As in (**g**) for mitochondrial Ca^{2+}, measured with pCAG mito-RCaMP1h; peak response times indicated per condition; n=4. **i**, PKA-dependent phosphorylation of MIC19-3xHA in Control *versus* SPHKAP or VAPB RNAi-treated INS-1 832/3 cells under Veh *versus* Ex-4-stimulated conditions, determined by Western blotting of anti-HA immunoprecipitates with an anti-RRx-pS/T antibody. **j**, Mitochondrial DNA (mtDNA) copy number, measured as a ratio of mitochondrial $tRNA^{Pro}$ over hexokinase (HK) in Veh *versus* Ex-4-stimulated Control and SPHKAP RNAi-treated INS-1 832/3 cells, as well as INS-1 832/3 GLP-1R KO cells; n=7; ns, non-significant by two-way ANOVA with Tukey post-hoc test.

Supplementary Fig. 8. GLP-1R and SPHKAP-dependent mitochondrial remodelling – Extra data. a, Overlay of a single confocal slice, with signals for VAPB (green), GLP-1R (yellow), mitochondria (magenta), and DAPI (blue) shown, and corresponding single slice of an EM tomogram following CLEM analysis of exendin-4 (Ex-4)-stimulated INS-1 832/3 SNAP/FLAG-hGLP-1R cells; size bar, 1 µm; magnified confocal slice region with arrow pointing to SNAP/FLAG-hGLP-1R positive signal also shown; size bar, 1 µm. **b**, Magnification of tomogram slices corresponding to magnified confocal slice from (**a**); arrow points to the same SNAP/FLAG-hGLP-1R-positive lysosome as in (**a**) embedded in a mitochondrion, indicating mitophagy; size bar, 1 µm. **c**, Single channel images corresponding to mito-BFP (blue) and mCherry-Drp1 (red) signals from Fig. 5g. **d**, Quantification of mitochondrial mean form factor and mean area in Veh *versus* Ex-4-stimulated WT and GLP-1R KO INS-1 832/3 cells; n=5, *p<0.05, **p<0.01, ns, non-significant, by one-way ANOVA with Šidák post-hoc test. **e**, As in (**d**) in Veh *versus* Ex-4-stimulated Control *versus* SPHKAP RNAi-treated INS-1 832/3 cells; n=5, *p<0.05, **p<0.01, ***p<0.001, ns, non-significant, by one-way ANOVA with Šidák post-hoc test.

Supplementary Fig. 9. GLP-1R–VAPB/SPHKAP interactions and GLP-1R-dependent mitochondrial remodelling in primary islets – Extra data. a, Negative control (no primary antibody) for PLA data shown in Fig. 8a; nuclei (DAPI), blue; size bar, 20 µm. **b**, PLA showing interactions between endogenous GLP-1R and SPHKAP (green) in vehicle (Veh) and exendin-4 (Ex-4)-stimulated primary mouse islets with insulin co-staining (red); nuclei (DAPI), blue; size bars, 20 µm. **c**, Quantification of SPHKAP mRNA levels by qPCR in Control *versus* SPHKAP shRNA-transduced intact primary mouse islets; n=3. **d**, Example of cell segmentation into hyperfused (blue), tubular (purple) or fragmented (pink) mitochondrial phenotypes in a primary mouse islet. **e**, Quantification of mitochondrial mean form factor and mean area in Control *versus* SPHKAP RNAi-treated dispersed mouse islet cells under Veh

versus Ex-4-stimulated conditions; *n*=4, *p<0.05, ***p<0.001, ns, non-significant, by one-way ANOVA with Šidák post-hoc test.

Supplementary Movie 1. Time-lapse confocal microscopy imaging of SNAP/FLAG-hGLP-1R (red) and EGFP-VAPB (green) localisation in response to exendin-4 stimulation in INS-1 832/3 SNAP/FLAG-hGLP-1R cells; images taken every 6 seconds, shown at 5 frames per second.

Supplementary Movie 2. Time-lapse confocal microscopy imaging of SNAP/FLAG-hGLP-1R (red) and ERMCS (SPLICS Mt-ER Long P2A, green) localisation in response to exendin-4 stimulation in INS-1 832/3 SNAP/FLAG-hGLP-1R cells; images taken every 6 seconds, shown at 5 frames per second; acquisition starts at 60 seconds post-exendin-4 exposure.

Supplementary Movie 3. Time-lapse confocal microscopy imaging of Drp1 (mCherry-Drp1, red) and mitochondria (mito-BFP, blue) localisation in vehicle-exposed INS-1 832/3 cells; images taken every 6 seconds, shown at 5 frames per second; acquisition starts at 60 seconds post-vehicle exposure.

Supplementary Movie 4. Time-lapse confocal microscopy imaging of Drp1 (mCherry-Drp1, red) and mitochondria (mito-BFP, blue) localisation in exendin-4-stimulated INS-1 832/3 cells; images taken every 6 seconds, shown at 5 frames per second; acquisition starts at 60 seconds post-vehicle exposure.

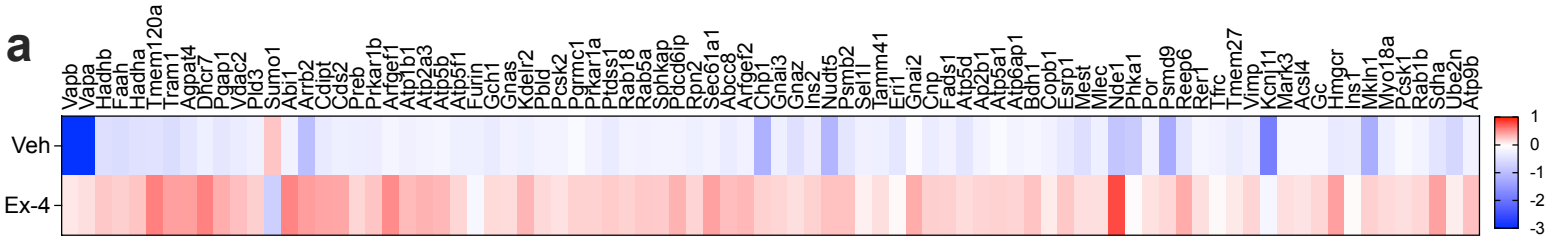

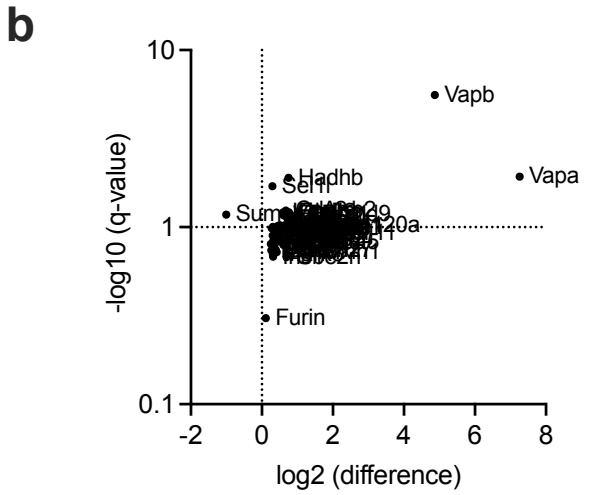

c

Name	Localisation	Function
VAPB	ER-Mitochondria contacts	lipid and ion transport
VAPA	ER-Mitochondria contacts	lipid and ion transport
HADHB	Mitochondria	β-oxidation of long chain fatty acids
FAAH	ER-Mitochondria contacts	fatty acid amide hydrolysis
HADHA	Mitochondria	β-oxidation of long chain fatty acids
APGAT4	ER / Mitochondria	phosphatidic acid biosynthesis
DHCR7	ER	cholesterol biosynthesis
VDAC2	ER-Mitochondria contacts	metabolite transport, mPTP component
CDS2	ER	phosphatidylinositol biosynthesis
ATP2A3	ER-Mitochondria contacts	SERCA pump, calcium transport
ATP5B	Mitochondria	ATP synthase subunit
ATP5F1	Mitochondria	ATP synthase subunit
PGRMC1	ER / Mitochondria	cholesterol metabolism
PTDSS1	ER	phosphatidylserine biosynthesis
Rab18	ER	lipid droplet biogenesis, lipolysis
SPHKAP	Mitochondria	PKA anchoring protein
TAMM41	Mitochondria	phosphatidylinositol biosynthesis
CNP	Mitochondria	calcium-induced opening of mPTP
FADS1	Mitochondria	fatty acid unsaturation
ATP5D	Mitochondria	ATP synthase subunit
ATP5A1	Mitochondria	ATP synthase subunit
BDH1	Mitochondria	fatty acid catabolism
POR	ER	cholesterol biosynthesis
REEP6	ER-Mitochondria contacts	GPCR regulation of mitochondrial function
HMGCR	ER	cholesterol biosynthesis
SDHA	Mitochondria	mitochondrial respiratory chain complex

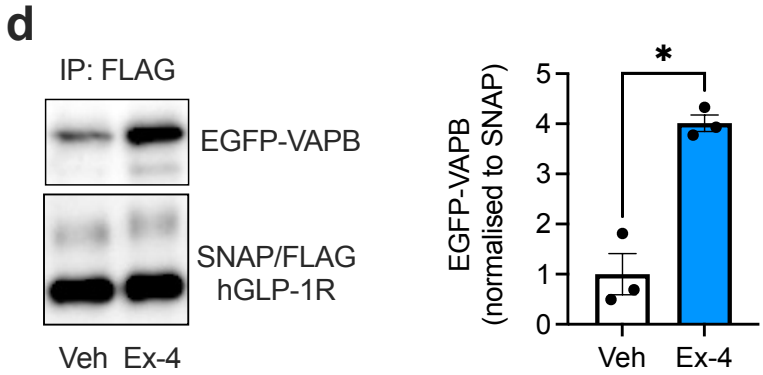

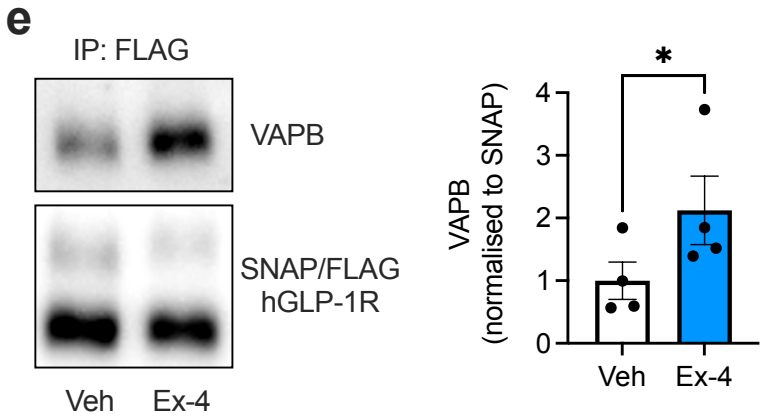

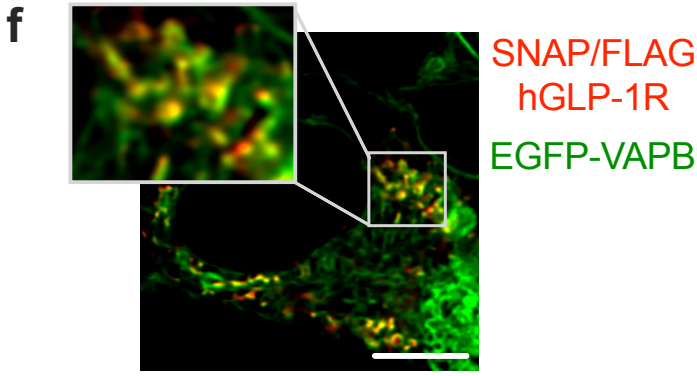

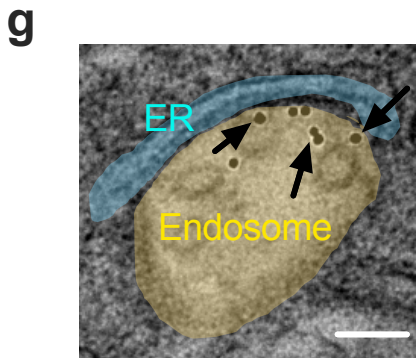

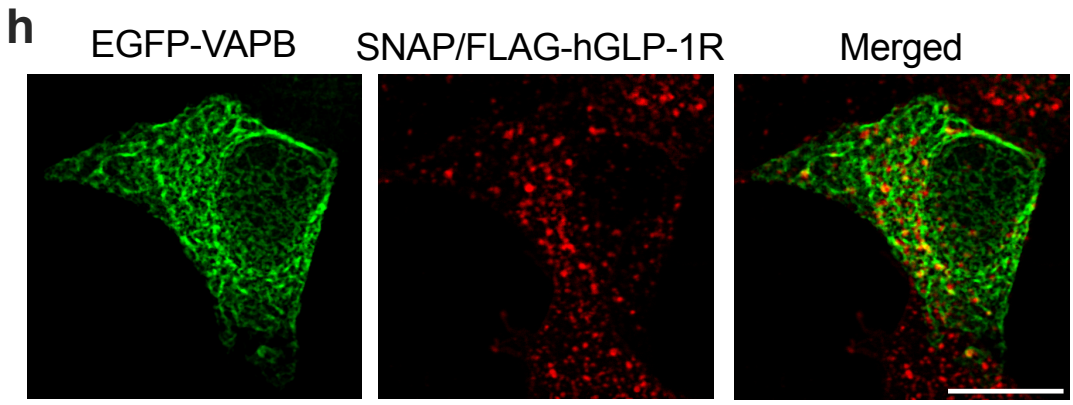

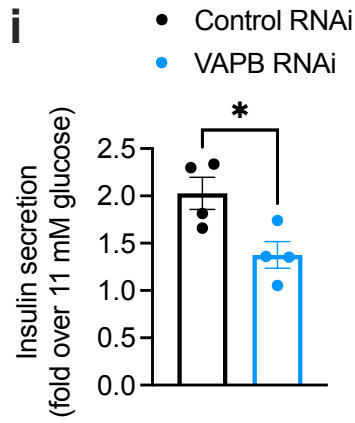

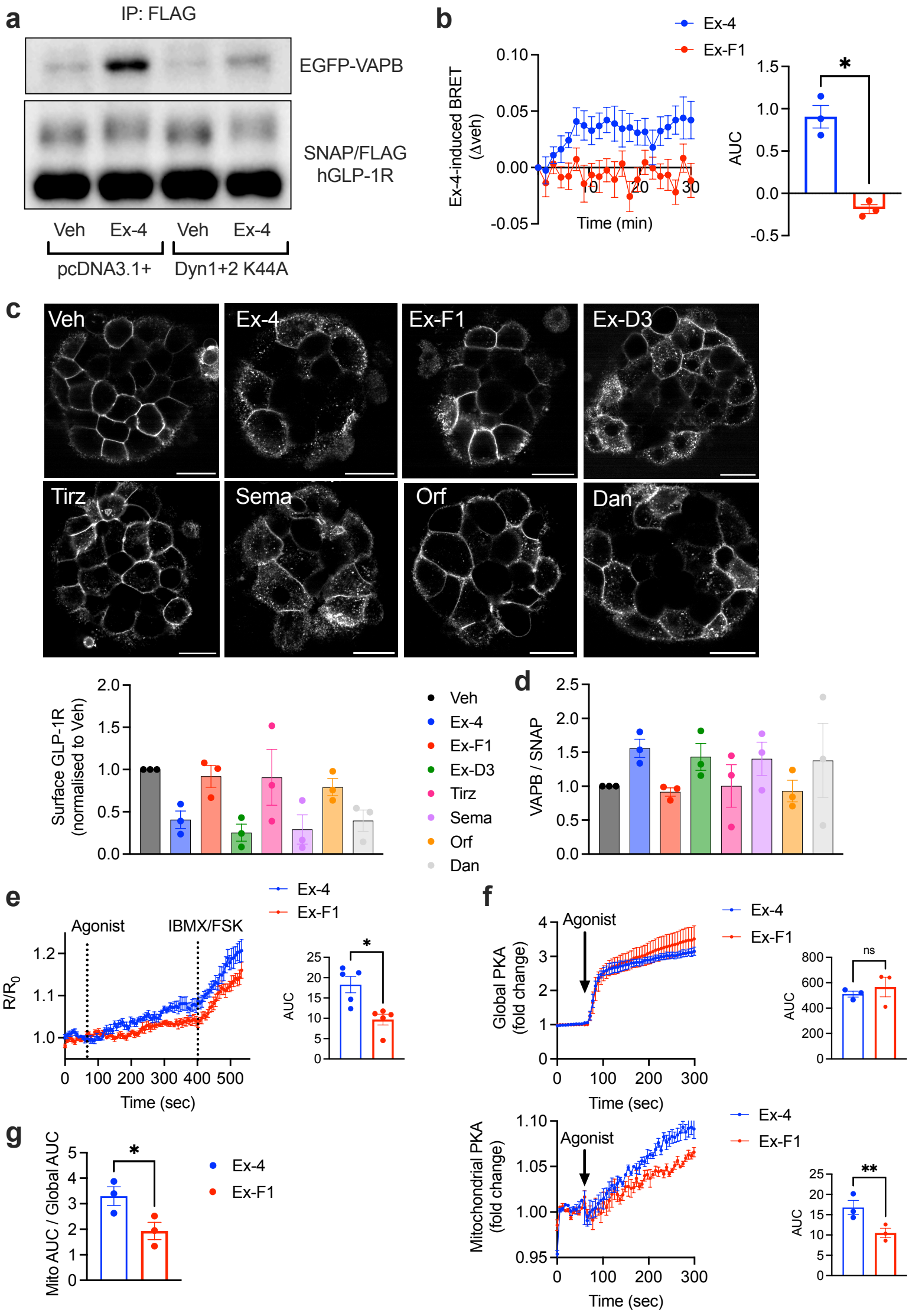
a
IP: FLAG
EGFP-VAPB
SNAP/FLAG hGLP-1R
Veh
Ex-4
Veh
Ex-4
pcDNA3.1+
Dyn1+2 K44A
b
Ex-4
Ex-F1
Ex-4-induced BRET (Δveh)
Time (min)
AUC
c
Veh
Ex-4
Ex-F1
Ex-D3
Tirz
Sema
Orf
Dan
Surface GLP-1R (normalised to Veh)
Veh
Ex-4
Ex-F1
Ex-D3
Tirz
Sema
Orf
Dan
d
VAPB / SNAP
e
Agonist
IBMX/FSK
R/R0
Time (sec)
AUC
f
Agonist
Global PKA (fold change)
Time (sec)
AUC
ns
Mitochondrial PKA (fold change)
Time (sec)
AUC
g
Mito AUC / Global AUC

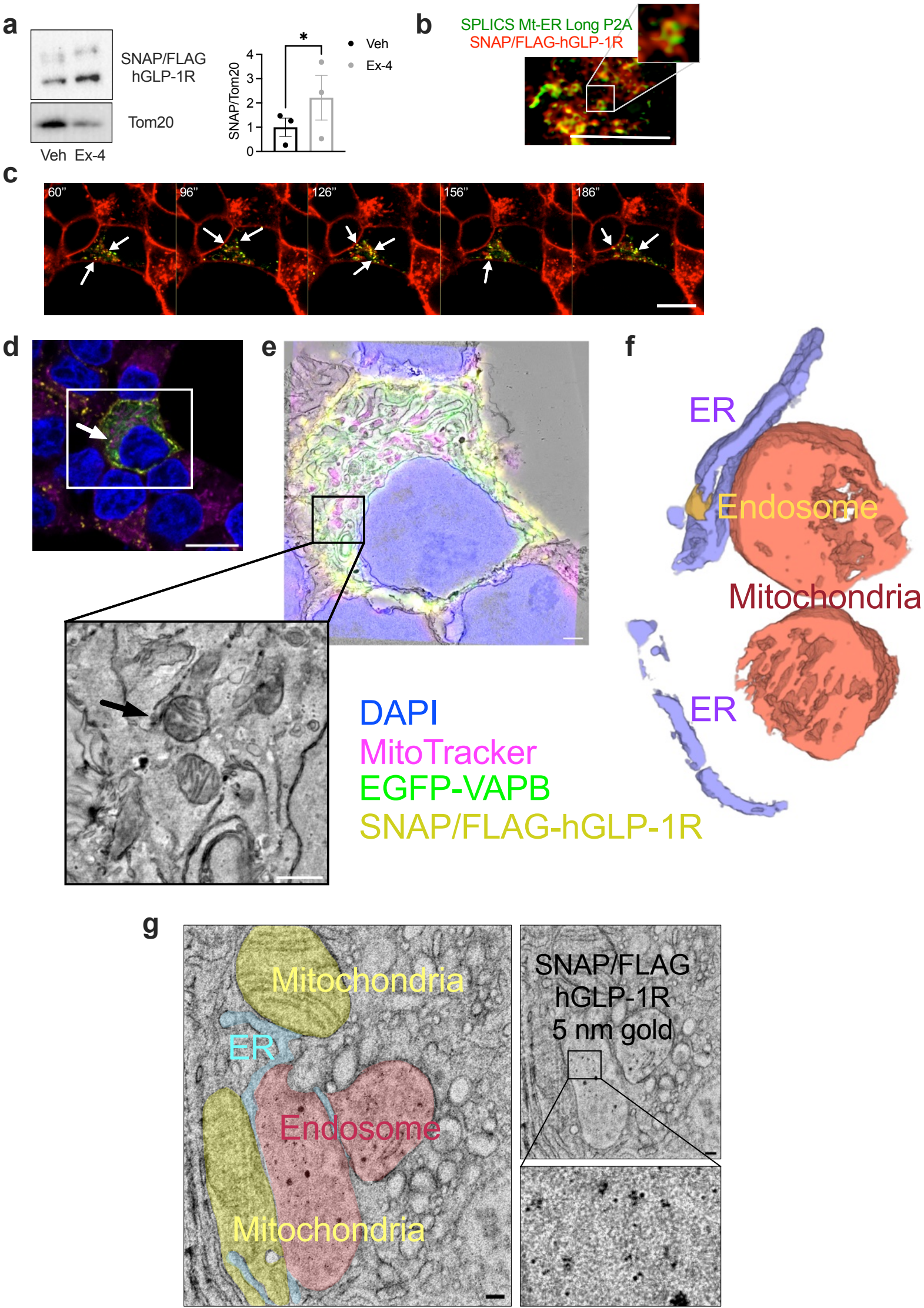
a
SNAP/FLAG
hGLP-1R
Tom20
Veh Ex-4
SNAP/Tom20
Veh
Ex-4
b
SPLICS Mt-ER Long P2A
SNAP/FLAG-hGLP-1R
c
60"
96"
126"
156"
186"
d
e
f
ER
Endosome
Mitochondria
ER
DAPI
MitoTracker
EGFP-VAPB
SNAP/FLAG-hGLP-1R
g
Mitochondria
ER
Endosome
Mitochondria
SNAP/FLAG
hGLP-1R
5 nm gold

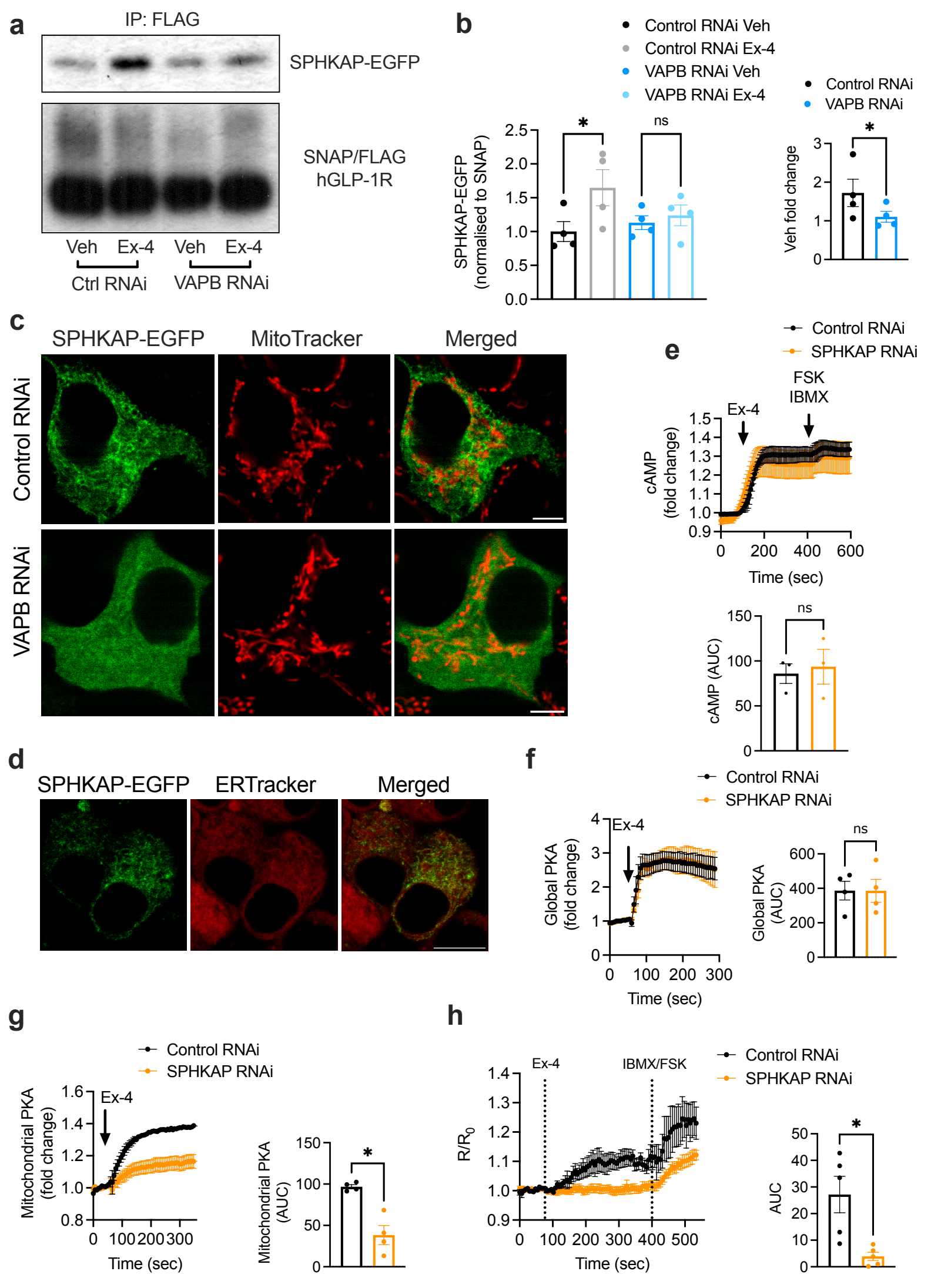
a
IP: FLAG
SPHKAP-EGFP
SNAP/FLAG
hGLP-1R
Veh
Ex-4
Veh
Ex-4
Ctrl RNAi
VAPB RNAi
b
Control RNAi Veh
Control RNAi Ex-4
VAPB RNAi Veh
VAPB RNAi Ex-4
SPHKAP-EGFP
(normalised to SNAP)
*
ns
Control RNAi
VAPB RNAi
Veh fold change
*
c
SPHKAP-EGFP
MitoTracker
Merged
Control RNAi
VAPB RNAi
e
Control RNAi
SPHKAP RNAi
FSK
IBMX
Ex-4
cAMP
(fold change)
Time (sec)
ns
cAMP (AUC)
d
SPHKAP-EGFP
ERTracker
Merged
f
Control RNAi
SPHKAP RNAi
Ex-4
Global PKA
(fold change)
Time (sec)
ns
Global PKA
(AUC)
g
Control RNAi
SPHKAP RNAi
Ex-4
Mitochondrial PKA
(fold change)
Time (sec)
Mitochondrial PKA
(AUC)
*
h
Ex-4
IBMX/FSK
Control RNAi
SPHKAP RNAi
R/R0
Time (sec)
AUC
*

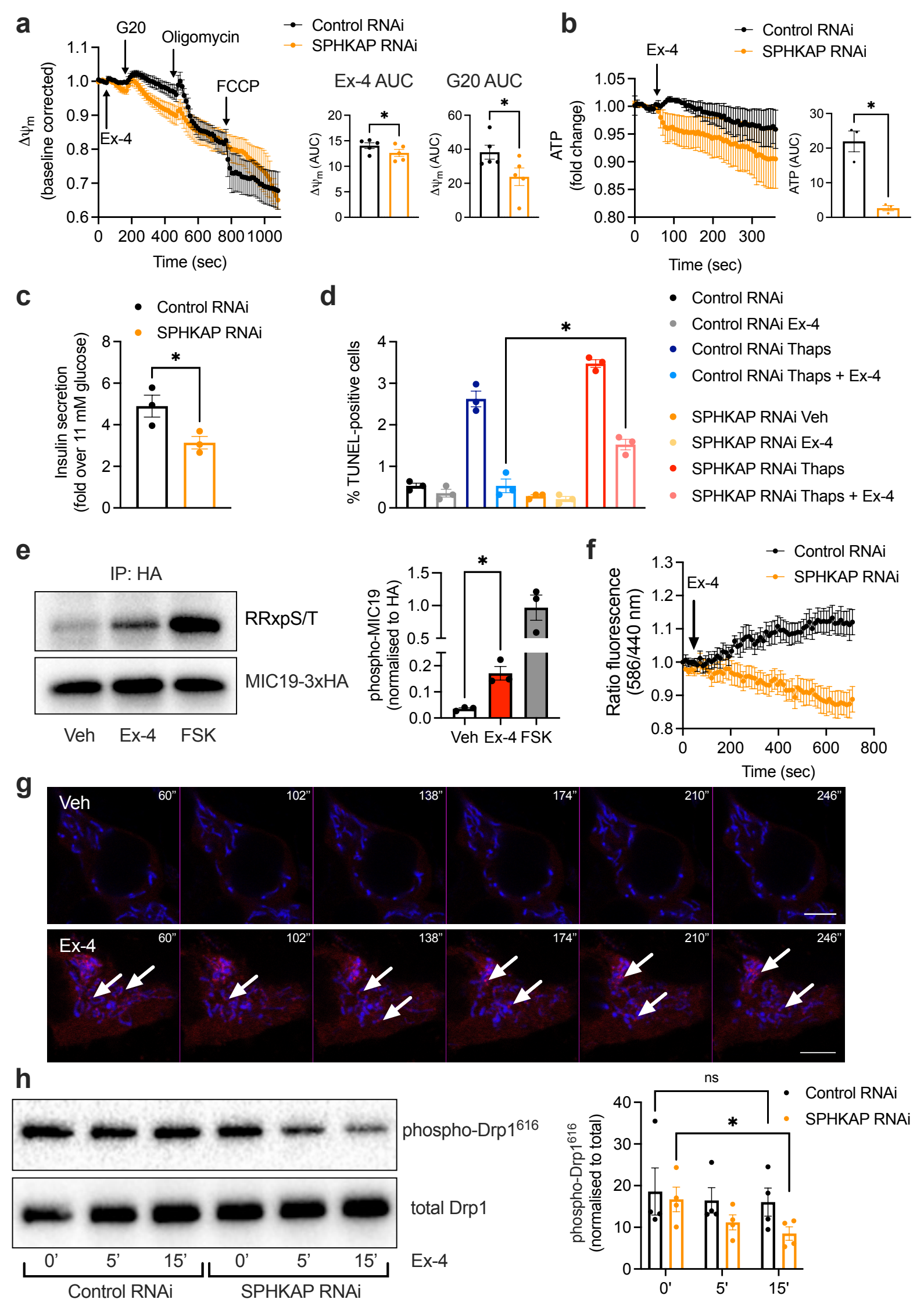
a
G20
Oligomycin
FCCP
Ex-4
Control RNAi
SPHKAP RNAi
Δψm (baseline corrected)
Time (sec)
Ex-4 AUC
G20 AUC
Δψm (AUC)
b
Ex-4
ATP (fold change)
ATP (AUC)
Time (sec)
c
Insulin secretion (fold over 11 mM glucose)
d
% TUNEL-positive cells
Control RNAi
Control RNAi Ex-4
Control RNAi Thaps
Control RNAi Thaps + Ex-4
SPHKAP RNAi Veh
SPHKAP RNAi Ex-4
SPHKAP RNAi Thaps
SPHKAP RNAi Thaps + Ex-4
e
IP: HA
RRxpS/T
MIC19-3xHA
Veh
Ex-4
FSK
phospho-MIC19 (normalised to HA)
f
Ratio fluorescence (586/440 nm)
Time (sec)
g
Veh
Ex-4
60"
102"
138"
174"
210"
246"
h
phospho-Drp1616
total Drp1
0'
5'
15'
Ex-4
Control RNAi
SPHKAP RNAi
ns
phospho-Drp1616 (normalised to total)

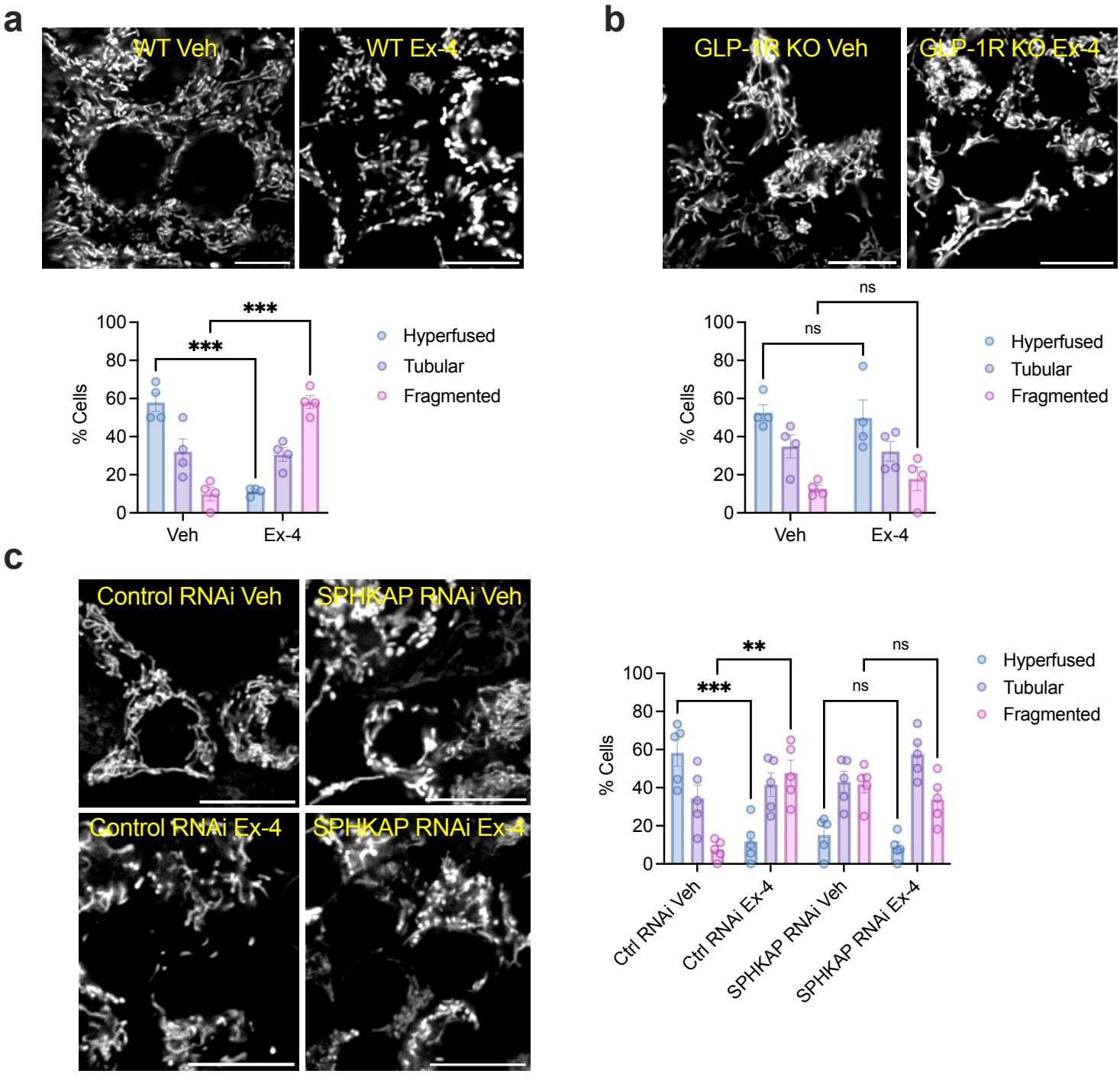
a
WT Veh
WT Ex-4
% Cells
100
80
60
40
20
0
Veh
Ex-4
***
***
Hyperfused
Tubular
Fragmented
b
GLP-1R KO Veh
GLP-1R KO Ex-4
ns
ns
c
Control RNAi Veh
SPHKAP RNAi Veh
Control RNAi Ex-4
SPHKAP RNAi Ex-4
**
***
ns
ns
Ctrl RNAi Veh
Ctrl RNAi Ex-4
SPHKAP RNAi Veh
SPHKAP RNAi Ex-4

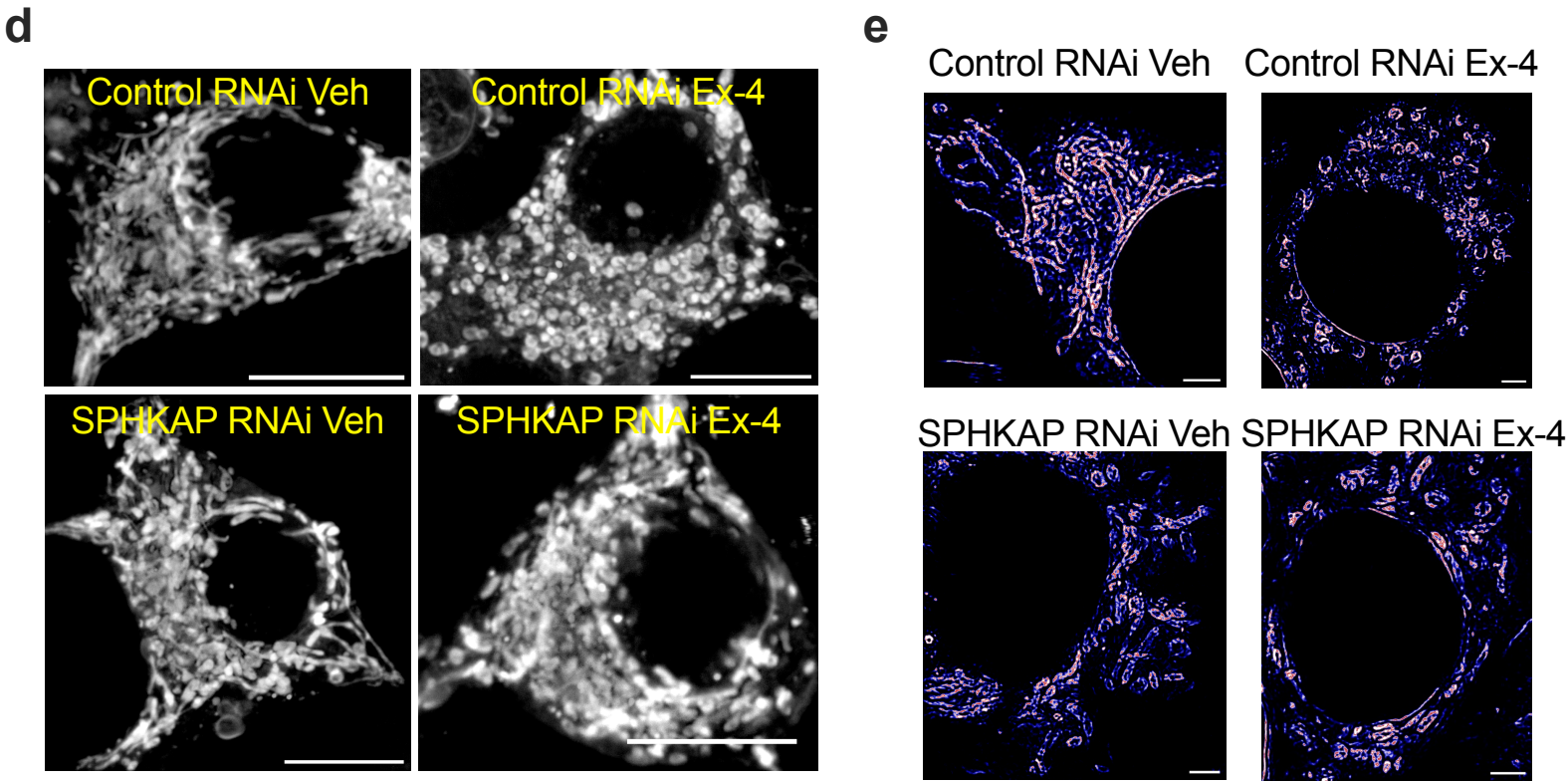
d
Control RNAi Veh
Control RNAi Ex-4
SPHKAP RNAi Veh
SPHKAP RNAi Ex-4
e
Control RNAi Veh
Control RNAi Ex-4
SPHKAP RNAi Veh
SPHKAP RNAi Ex-4

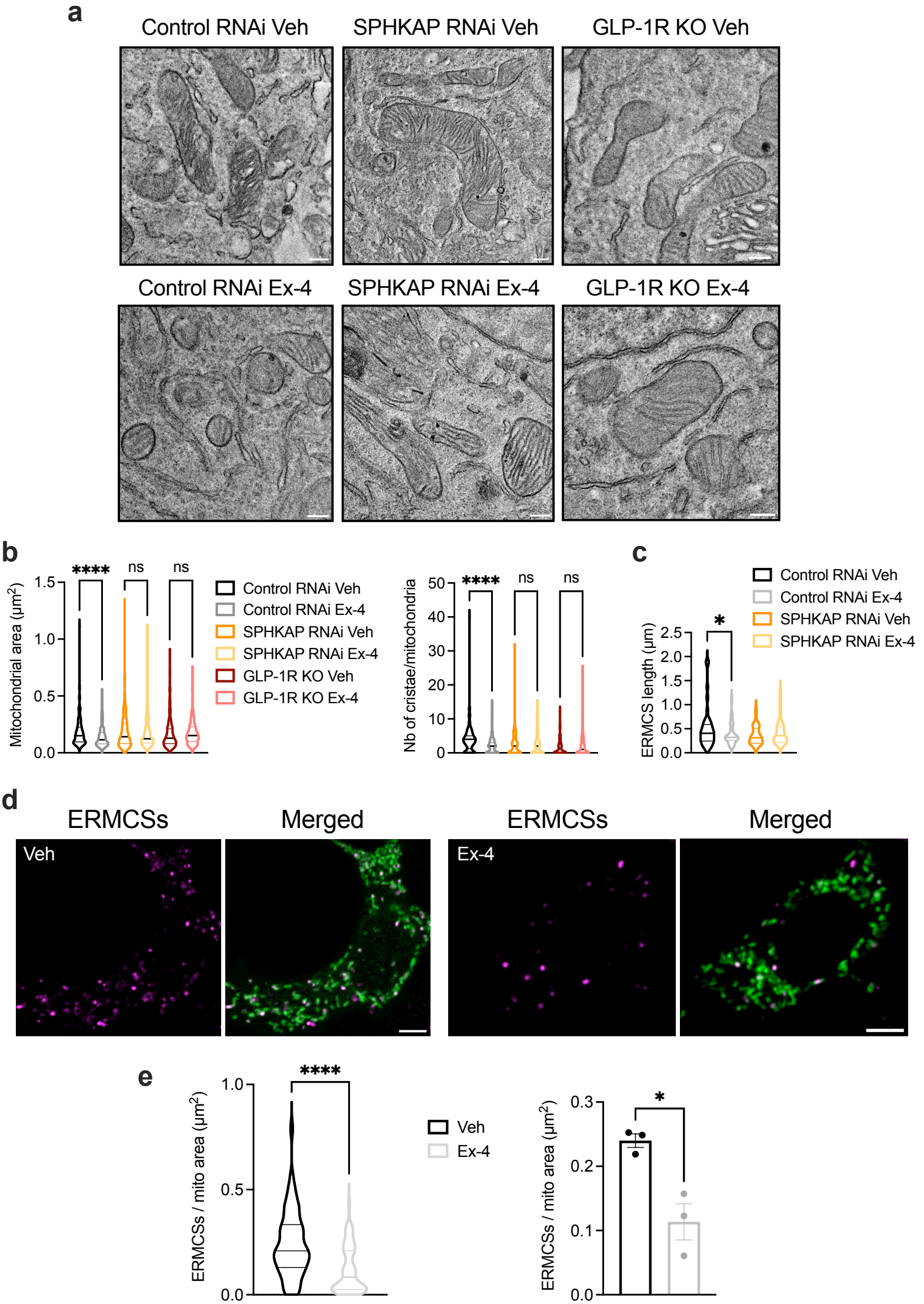
a
Control RNAi Veh
SPHKAP RNAi Veh
GLP-1R KO Veh
Control RNAi Ex-4
SPHKAP RNAi Ex-4
GLP-1R KO Ex-4
b
Mitochondrial area (µm²)
****
ns
ns
Control RNAi Veh
Control RNAi Ex-4
SPHKAP RNAi Veh
SPHKAP RNAi Ex-4
GLP-1R KO Veh
GLP-1R KO Ex-4
Nb of cristae/mitochondria
c
ERMCS length (µm)
*
d
ERMCSs
Merged
Veh
Ex-4
e
ERMCSs / mito area (µm²)
Veh
Ex-4

a

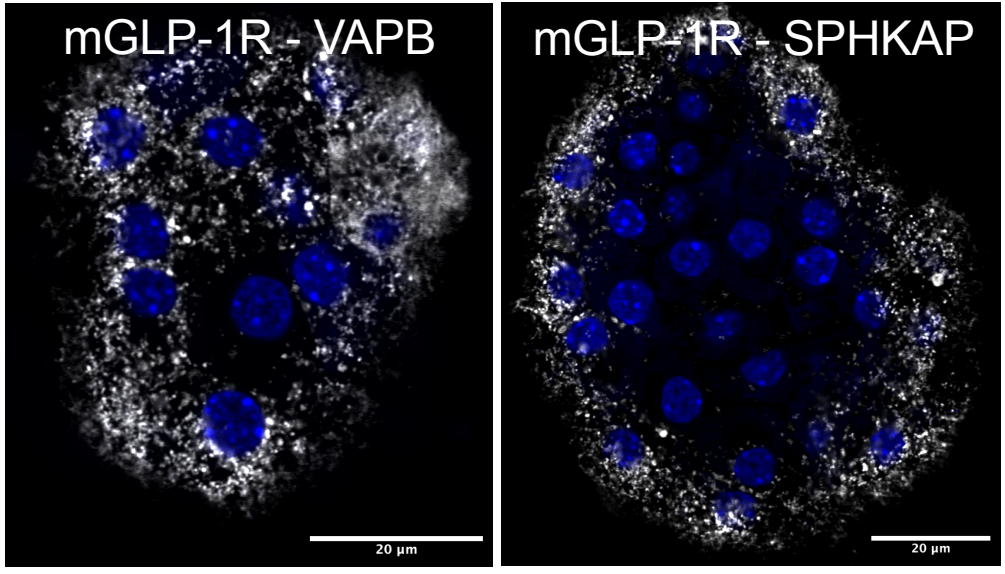
mGLP-1R - VAPB
mGLP-1R - SPHKAP
20 µm
20 µm

b

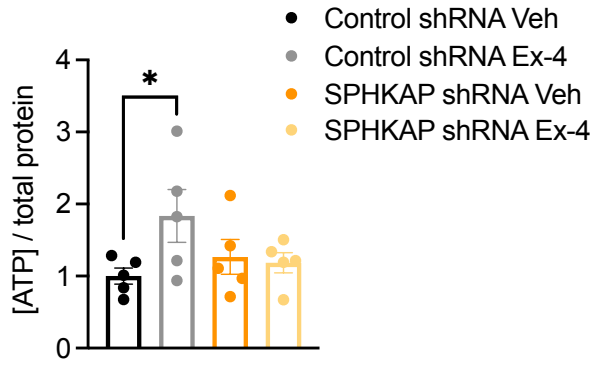
Control shRNA Veh
Control shRNA Ex-4
SPHKAP shRNA Veh
SPHKAP shRNA Ex-4
[ATP] / total protein
0
1
2
3
4
*

c

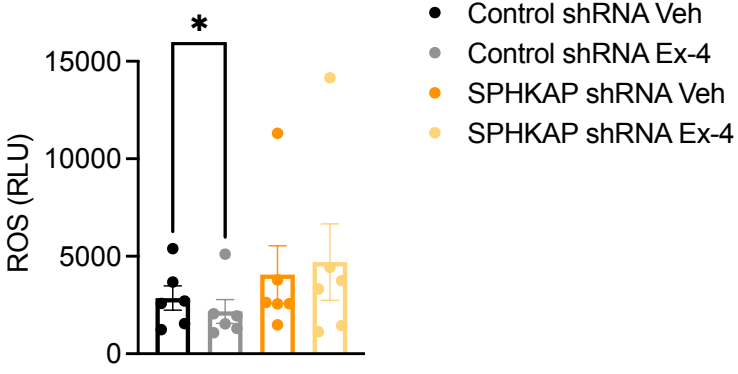
Control shRNA Veh
Control shRNA Ex-4
SPHKAP shRNA Veh
SPHKAP shRNA Ex-4
ROS (RLU)
0
5000
10000
15000
*

d

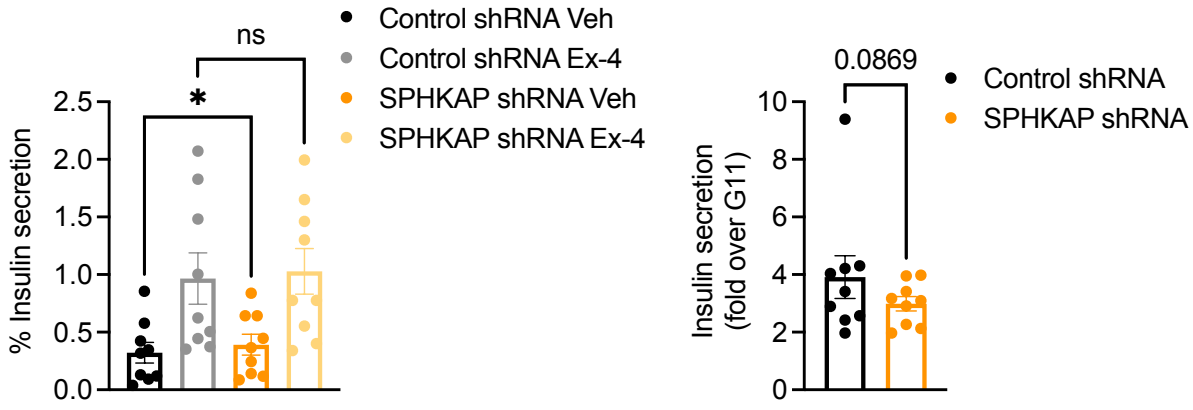
Control shRNA Veh
Control shRNA Ex-4
SPHKAP shRNA Veh
SPHKAP shRNA Ex-4
% Insulin secretion
0.0
0.5
1.0
1.5
2.0
2.5
ns
*
Control shRNA
SPHKAP shRNA
Insulin secretion
(fold over G11)
0
2
4
6
8
10
0.0869

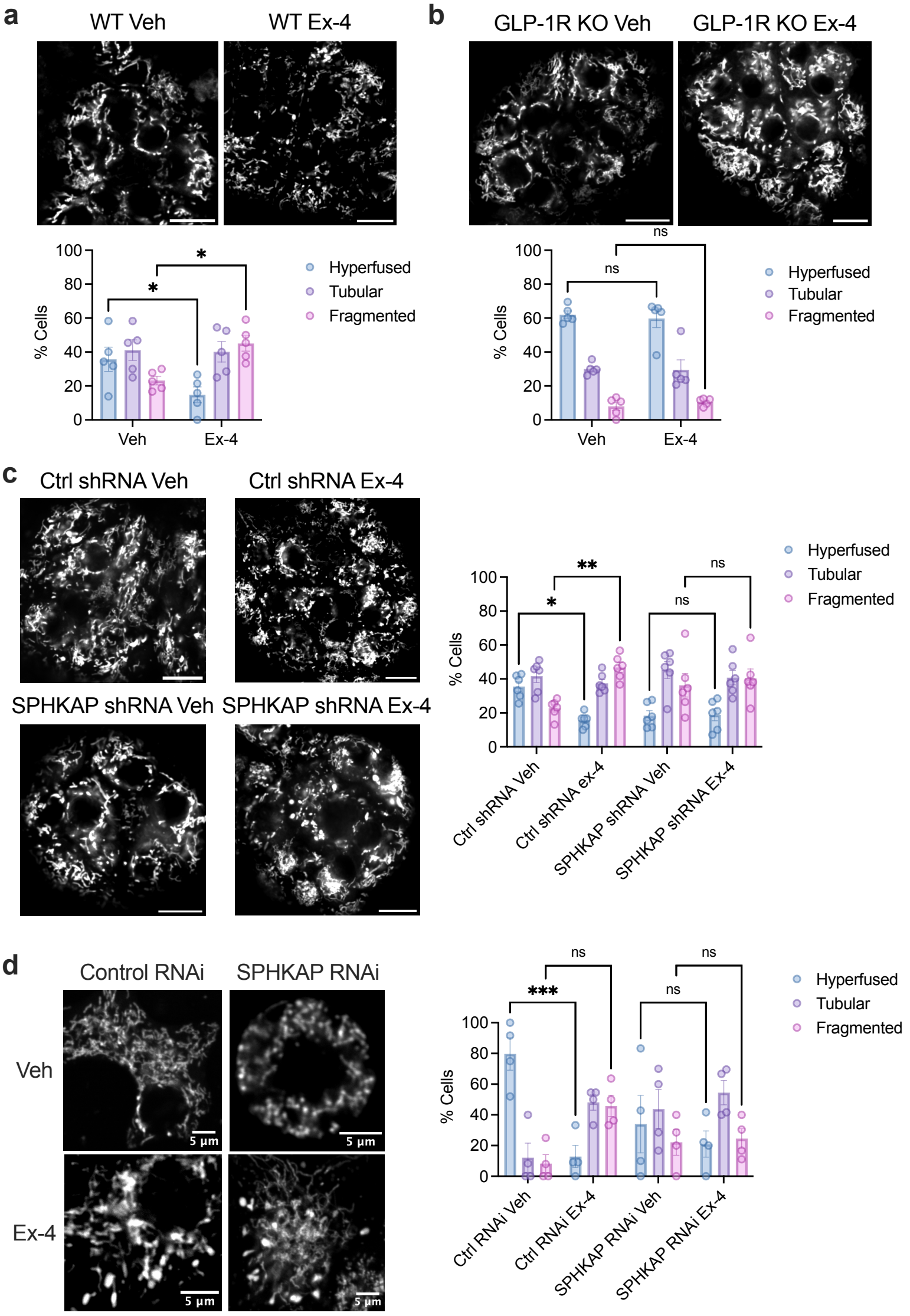
a
WT Veh
WT Ex-4
% Cells
100
80
60
40
20
0
Veh
Ex-4
*
*
Hyperfused
Tubular
Fragmented
b
GLP-1R KO Veh
GLP-1R KO Ex-4
ns
ns
% Cells
Veh
Ex-4
Hyperfused
Tubular
Fragmented
c
Ctrl shRNA Veh
Ctrl shRNA Ex-4
SPHKAP shRNA Veh
SPHKAP shRNA Ex-4
**
*
ns
ns
% Cells
Ctrl shRNA Veh
Ctrl shRNA ex-4
SPHKAP shRNA Veh
SPHKAP shRNA Ex-4
Hyperfused
Tubular
Fragmented
d
Control RNAi
SPHKAP RNAi
Veh
Ex-4
5 µm
5 µm
5 µm
5 µm
ns
ns
***
ns
% Cells
Ctrl RNAi Veh
Ctrl RNAi Ex-4
SPHKAP RNAi Veh
SPHKAP RNAi Ex-4
Hyperfused
Tubular
Fragmented

a

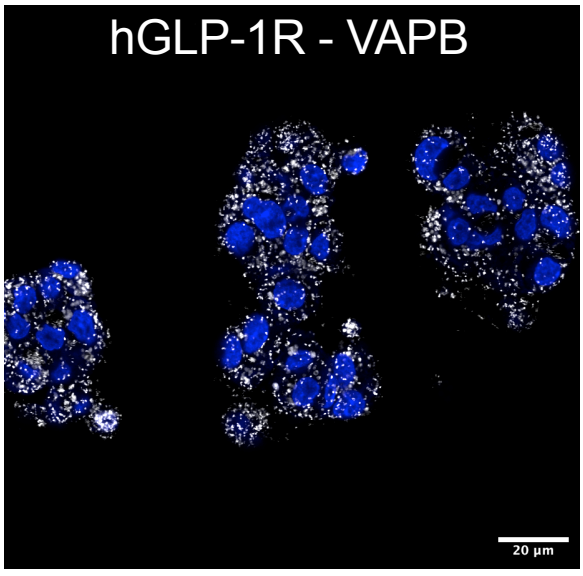
hGLP-1R - VAPB
20 µm

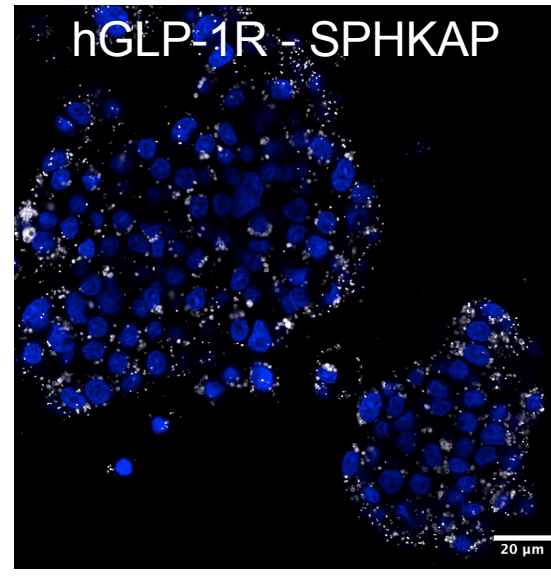
hGLP-1R - SPHKAP
20 µm

b

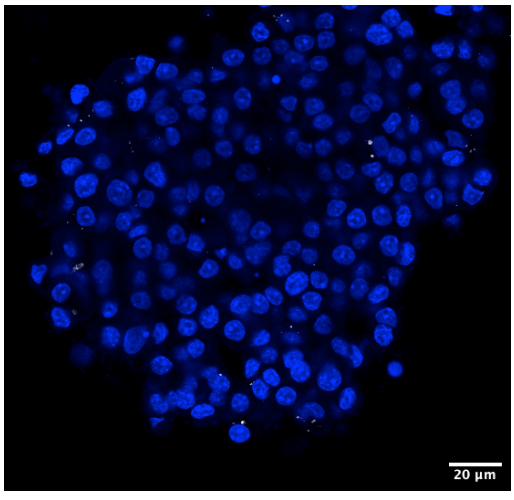
20 µm

c

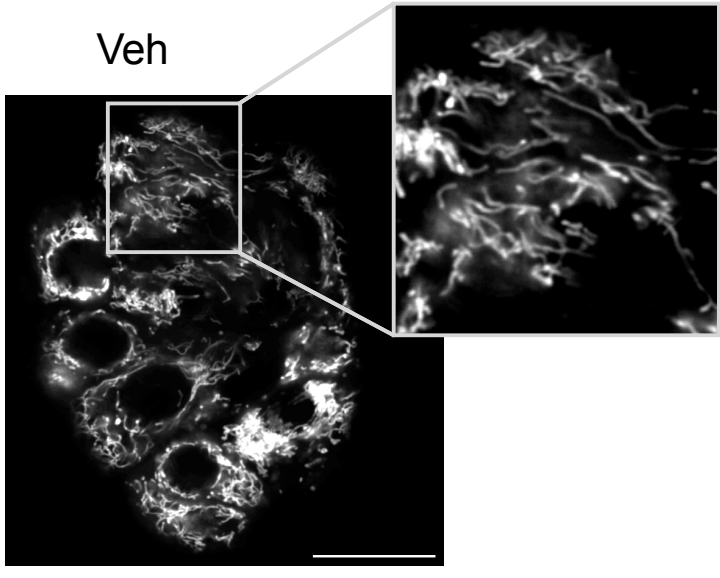
Veh

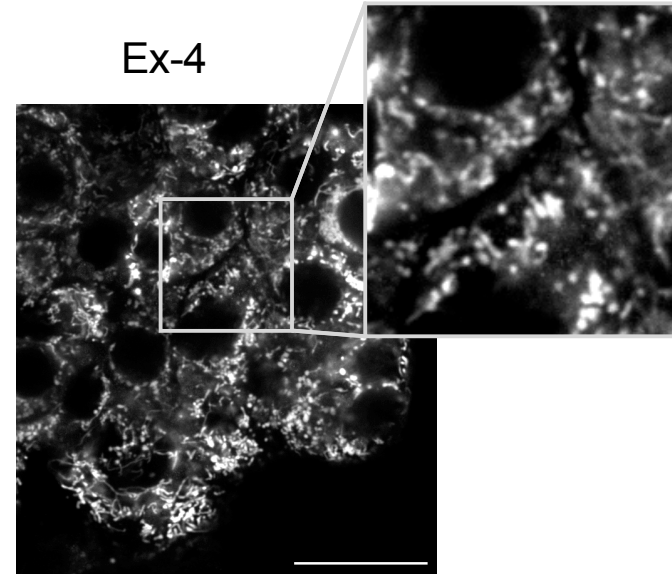
Ex-4

d

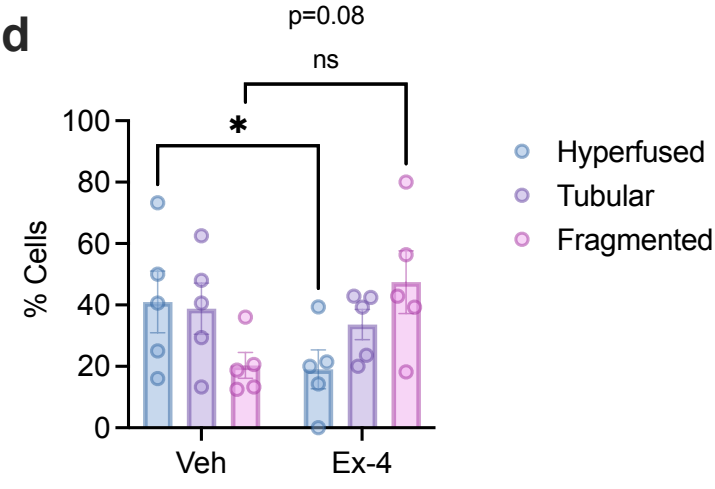
p=0.08
ns
*
100
80
60
40
20
0
% Cells
Veh
Ex-4
Hyperfused
Tubular
Fragmented